Earthquake Loss Estimation Based on Building Inventory Data and Strong Motion Prediction in Ulaanbaatar city, Mongolia

（モンゴル・ウランバートル市における強震動予測と

建物台帳データに基づく地震被害予測）

2022 年 3 月

Zorigt Tumurbaatar

Content of thesis

Acknowledgments

I would like to express my deepest gratitude to my supervisor, associate prof Hiroyuki Miura for the endless support, valuable advice, patience, and constant encouragement during my Ph.D.

I would like to thank the Environmental and Earthquake Engineering project unit of the Mongol-Japan Higher Engineering Education Development (M-JEED) project, Dr. Ts.Tsoggerel and other staff for supporting me during the study.

I would like to extend my appreciation to senior Prof. Haruyuki Yamamoto, P.Otgonbayar, D.Dashjamts, Prof. G.Ganzorig, Prof. Ya.Duinkherjav, Prof. M.Oyunchimeg, lecturer B.Erdenebold, and MUST workmates, I will always be in the depth of your support.

I am grateful for supporting data of research, Ph.D. Ts.Batsaikhan, Dr. Ch.Odonbaatar of Institute of Astronomy and Geophysics, Consultant Engineer G.Tulga “Tulga Project” Co., Ltd, A.Batsaikhan “Soil Trade” Co., Ltd, Consultant Engineer M.Myagmarjav “ENGIGEOTECH” Co., Ltd and my friend engineer S.Baasansuren Ulaanbaatar city Capital Investment Agency.

I want to thank my family and parents, who always love and support me in my academic career.

Zorigt Tumurbaatar

Hiroshima University, Higashihiroshima City, Japan

February 2022

Abstract

Mongolia has been one of the most seismically active intracontinental regions in the world, with four large earthquakes with magnitudes of around 8 along with their active faults in the western part of the country during the last century. Compared with western Mongolia, central Mongolia, including Ulaanbaatar's region (UB), is considered as the relatively low seismically active zone. Even though, according to the previous investigation, there are several active faults such as Hustai, Gunj, and Emeelt faults. In particular, the Emeelt fault earthquake with the estimated maximum magnitude of 7 has been expected to impact the UB region significantly because the fault is located at around 20km from UB to the west-south-west direction. In this research, building loss estimation due to a scenario earthquake is performed based on strong motion prediction and updated building inventory data in Ulaanbaatar city (UB), Mongolia.

In Chapter 1, the seismic and social conditions in UB are described for applying strong motion simulation and building damage assessment. I revealed that the detailed shear-wave velocity models and up-to-date building inventory are required in UB because such data is not prepared in the target area. The literature reviews for the microtremor-based approach for developing underground structure models and urban-scale building damage assessments are also conducted. The objective and methods of this research are explained.

In Chapter 2, microtremor measurements are conducted at 50 sites in UB, and microtremor horizontal-to-vertical spectral ratio (MHVR) is obtained to evaluate the site effects. The joint inversion technique based on the diffuse field theory is applied to the observed MHVRs and surface-wave dispersion data estimated by microtremor array observation in previous research at three sites in UB for estimating shear-wave velocity structure models. Based on the joint inversion analysis results, single inversion is applied to the MHVRs at the rest of the observation sites for estimating shear-wave velocity models. The surface shear-wave velocity models estimated by the inversion analysis show good agreement with soil models of existing borehole data. Finally, the theoretical site amplifications

of S-waves are evaluated by the estimated shear-wave velocity models, and the seismic zoning is performed based on the amplification factors.

In Chapter 3, a strong ground motion simulation is performed for the scenario earthquake induced by the Emeelt fault. Seismic ground motions at the seismic bedrock are computed by the stochastic Green's function (SGF) method and the characterized fault model. Seismic ground motions at the ground surface are calculated by the estimated shear-wave velocity models in Chapter II and the equivalent linear seismic response analysis method of DYNEQ. The dynamic soil properties for sand and gravel developed in Japan are applied to evaluate the nonlinear response of strong shaking. The distributions of spectral accelerations for typical periods are estimated from the strong ground motion simulation and spatial interpolation technique. The simulation results show that the peak ground acceleration is expected at approximately 500 cm/s/s in the western part of UB located near the fault.

In Chapter 4, the building inventory data is updated from the existing data by estimating heating type, structural class, and construction year for the unregistered buildings to estimate the buildings' construction cost. Since Mongolia is located in the cold region, the heating type is a critical item that controls the construction cost. The building information is estimated from the location, building use, building height, and building shapes, such as the registered buildings' area, length, and width. The construction cost for each building is evaluated based on the Mongolian construction code. I confirmed that the estimated construction costs aggregated for the districts show good agreement with the official statistics for the building properties.

In Chapter 5, the financial building loss due to the scenario earthquake is based on the strong motion simulation, the updated building inventory data, and global vulnerability functions developed in GAR-13. The building vulnerability classes are assigned by the structural type, building height, and location. The result of the loss estimation shows the total amount of the loss is approximately 3.4 billion USD, whereas the recent growth domestic product (GDP) in Mongolia is 28.7 billion USD, indicating the loss reaches approximately 26 % of the Mongolian GDP. The estimated loss almost

corresponds to the direct shaking-related economic losses in the recent worldwide M7 class earthquakes.

Chapter 6 summarizes the research in this thesis, and also the strengths and limitations of this study are described for future research.

List of figures

List of tables

CHAPTER 1. INTRODUCTION

1. 1. Background

The capital Ulaanbaatar (UB) is the largest city of Mongolia, at an elevation of about 1350 m, along the valley of Tuul River and at the foot of the Bogd Mountain (about 1900 m). UB is also the economic and industrial center of the country. The population of UB is increased during the last 20 years, from 700.000 to about 1.452 million inhabitants, today about 44% of the whole population of Mongolia is concentrated in UB. Due to the population growth and urban sprawl in UB, hazard and risk analysis for future earthquakes have become an essential issue for disaster mitigation planning.

Earthquakes have significantly impacted economic and social losses in urban areas because they have brought extensive damage to buildings and infrastructures. Building damage is the most critical factor of seismic losses because buildings are the predominant facility in the built environment, and buildings are vulnerable to earthquake damage (Kircher et al., 1997). Building damage estimations for earthquake scenarios have been recognized as essential information for planning disaster reduction measures. However, UB has not fully developed the geophysical and building inventory database required for strong motion prediction and building damage estimation in earthquake scenarios.

1. 1. Literature review

1. 1. 1. Seismicity in Mongolia.

Mongolia has been one of the most seismically active intracontinental regions in the world, with four large earthquakes with magnitudes of around 8 along with their active faults in the western part of the country during the last century (Munkhsaikhan, 2016). Compared with western Mongolia, central Mongolia, including Ulaanbaatar's region (UB), is considered as a relatively low seismically active zone in Figure 1-1.

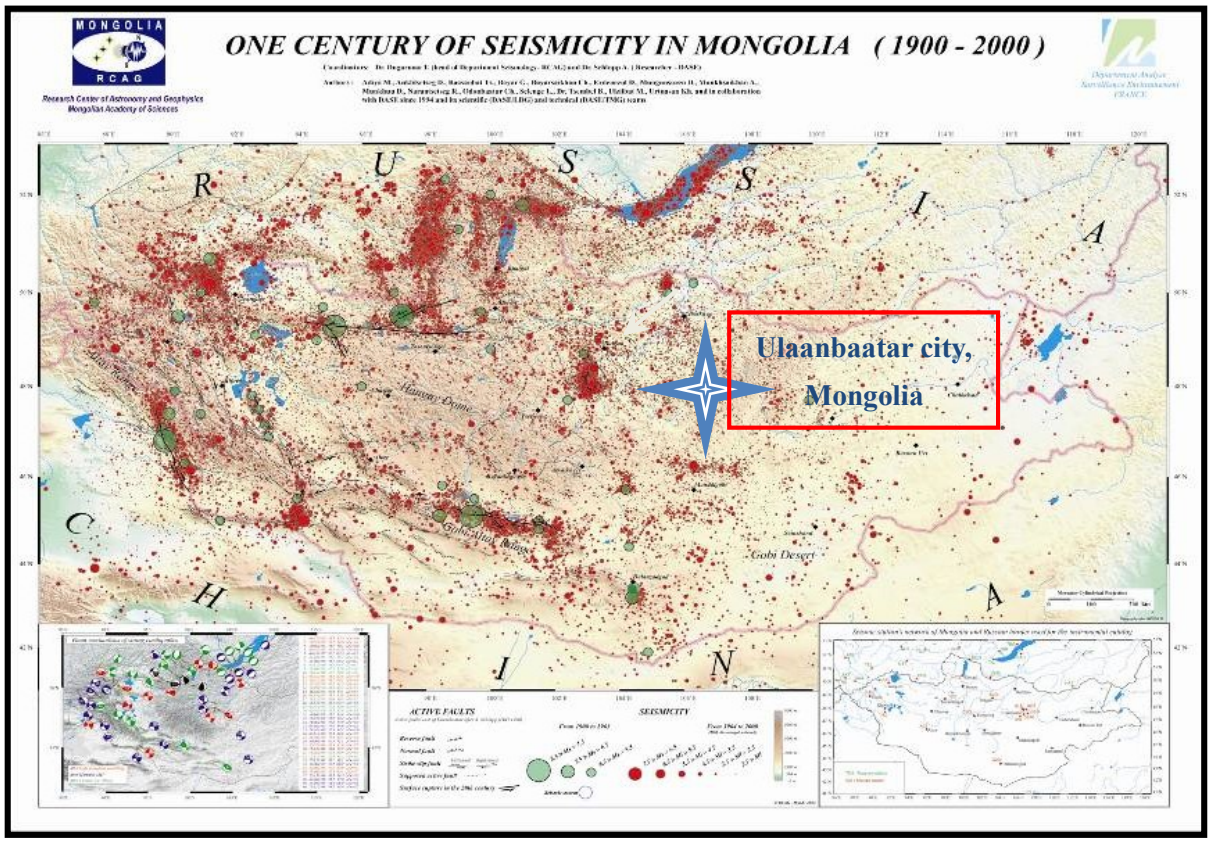

Figure 1-1. Seismicity in Mongolia (One Century of Seismicity in Mongolia RCAG). Star indicates the location of Ulaanbaatar city

According to some seismologists, the Ulaanbaatar region is considered a low seismic hazard region because of the absence of strong earthquakes compared to the strong historical earthquakes that

occur in western Mongolia. Another view of this assumption is the extremely thin population distribution in this area which has not suffered much due to the past earthquakes. Recording of earthquake magnitude around Ulaanbaatar can be divided into three periods: up to 1964, (1964-1994), and (1995-2014, or until 2017.) These can be called historical, early instrumental, and recent instrumental of seismic station, respectively. The period covers the time when seismology science began to develop in Mongolia between 1925 and 1964, and an earthquake measurement scale was magnitude M=4 to 5.4. These were reported in the International Seismological Centre (ISC), and were only recorded by the three components of seismic station Ulaanbaatar, Russian seismic stations more than 600 km away, and some notable scientists such as Natsag-yum and, Khilko. Sadly, some of the events lacked detailed information about macroseismic data, where it was difficult to estimate their magnitude.

Seismicity of the instrumental and recent instrumental period (1964-1994 and 1994-present time) A low number of earthquakes was recorded in the instrumental period because very few seismic stations with low sensitivity had been installed then the recent instrumental period, whereas the number of stations was significantly higher than the previous period. There only 672 earthquakes were localized in this area between 1964 and 1994. The last period corresponds to the end of 1994, until today. During that period, earthquake detection capacity increased due to installing several high-sensitivity digital stations around Ulaanbaatar. Plus, over 10,000 earthquakes were detected with a magnitude up to 5.6, but 90% of them were tiny. The largest earthquake occurred on 1998-09-24, in the south, 190km away from Ulaanbaatar, with a magnitude of 5.6.

The Mw=7.2 Mogod earthquake of 1967/01/05 is the most significant event in this region and was located 260 km from Ulaanbaatar city (Adiya 2016). And next one is Deren earthquake ML=5.3 the 2010 Deren earthquake ML=5.1.

Nevertheless, several earthquakes were largely felt in Ulaanbaatar during the last century (Intensity MSK up to VI) without significant damage.

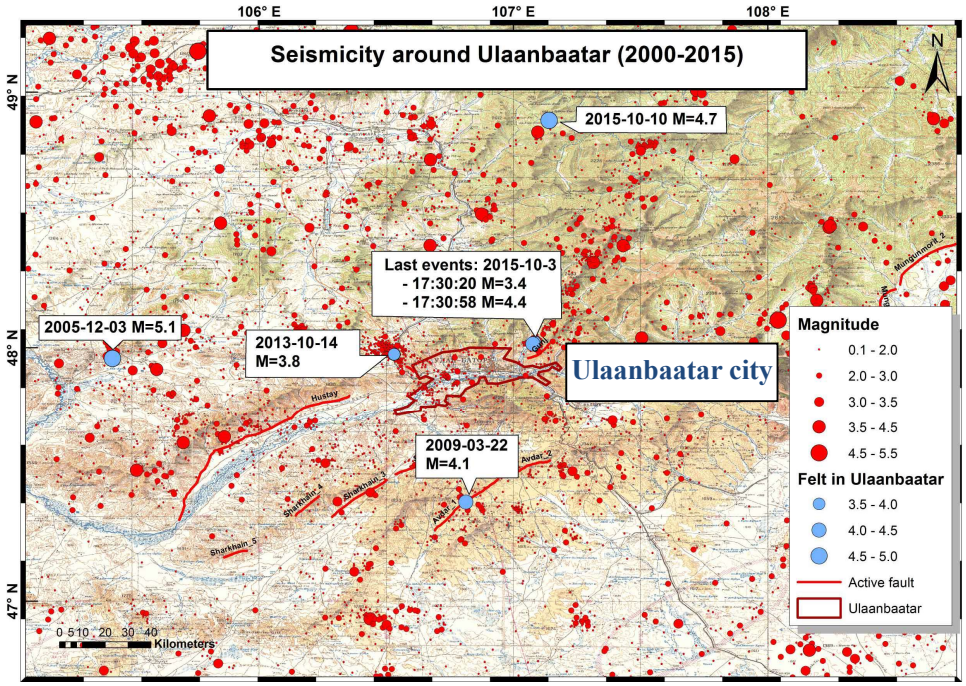

Figure 1-2. Seismicity map of Ulaanbaatar region (2000-2015). (Tsamba et al., 2017)

Since 2005, a stronger seismic activity (M ≤ 4.5) has been observed ~ 10 km west of the capital, around the newly discovered Emeelt fault (Schlupp et al., 2010a), which prompted studies in tectonic geomorphology and paleoseismology to characterize some of the few known active faults (Hustai, Gunj, Emeelt) and extend the catalogue of potential seismic sources in Figure 1-2. Collaborated researcher's team which included Institute of Astronomy and Geophysics (IAG) and France researchers worked on Emeelt fault area since 2005 it becomes the trending topic of Mongolian geophysical researchers with the development of highly sensitive seismic stations around UB. According to the area of Emeelt fault explorations (Munkhsaikhan, 2016), (Oyun-Erdene et al., 2014) estimated maximum moment magnitude Mw=7 indicates significant risk for UB's population. They used deterministic methods over the probabilistic approach to estimate strong motion. In the probabilistic approach, the return period is 11000 years and probability are very low in case of fault in

Table 1-1 (独立行政法人 & Japan International Cooperation Agency (JICA), 2016).

Table 1-1. Active fault information around Ulaanbaatar city.

	Active fault	Fault type	Fault length	Vertical displacement	Horziontal displacement	Magnitude	Most recent activity	Return period

1	Khustai	Left strike-slip / normal fault	212 km	10m	39 - 50 m	Mw＝7.8	1000 BP	10000 year
2	Avdar	Left strike-slip	50 km	-	50 m	Mw＝7.1 - 7.2	5812 - 5643 BP	10000 year
3	Gunjiin	Left strike-slip	15-20km	-	～25 m	Mw＝6.8	6500 - 9800 BP	10000 year
4	Sharkhai	Left strike-slip	50 km	-	-	Mw＝7.1 - 7.2	1180 ± 50 BP	10000 year
5	Emeelt	Right strike-slip / reverse fault	35 km	-	2 m	Mw＝6.5 - 7	～10000	10000 year
6	Mungunmorit	Low-angle reverse fault	90 km	1.5m	-	Mw＝7.8	9214 - 3165 BP	10000 year

1. 1. 2. Ground motion prediction

Empirical Green's Function Method (EGFM) has been employed to simulate strong ground motions for scenario earthquakes when appropriate ground motion data for small earthquakes is available (Irikura, 1986). To extend the EGFM to the cases in that any observed record of small earthquakes is not available, a way to calculate them based on the stochastic theory has been developed. This calculated small earthquake's record is called Stochastic Green's Function (SGF) (Boore, 1983). The way to synthesize strong-motion using the SGF is called the Stochastic Green's Function Method (SGFM). Figure 1-3 shows general steps to estimate strong ground motion considered site characteristics applied in this research.

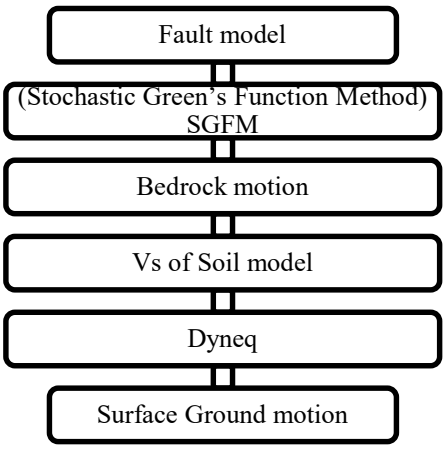

Figure 1-3. Flow chart of estimation of strong ground motion considered site characteristics.

Ground response analysis is vital to the estimate seismic behavior of the surface soil layer to calculate input earthquake motion to the building because the surface layer amplifies earthquake motion. Equivalent linear site response analysis DYNEQ (Yoshida, 2015) is applied to obtain the surface ground motion time histories. Shear modulus (G) and damping (h) are necessary as the mechanical properties in the equivalent linear method dynamic properties of soil are used to calculate in DYNEQ. Strain stiffness of ground (G/G0) and strain-damping (h-γ) for soil type sand, gravel, and bedrock were applied in this method.

1. 1. 3. Microtremor measurement

Microtremors (ambient ground noise) is a low-cost and convenient method to estimate site characterizations. For example, while horizontal motions are larger than vertical motion on the soft ground, both horizontal and vertical motions are similar on the stiff ground. In particular, Horizontal-to-Vertical (H/V) spectral ratio technique firstly proposed by Nakamura has been utilized to evaluate the fundamental resonant frequency of grounds (Lachetl & Bard, 1994; Lermo & Chavez-Garcia, n.d.). Microtremor H/V spectral ratio (MHVR) has also been used to estimate Vs profiles by assuming that the microtremors are mainly composed of surface waves (Arai, 2005; Arai & Tokimatsu, 2004).

Odonbaatar (Chimed, 2011) performed microtremor array observations at three UB sites to identify the deep underground structures and estimate the three-dimensional (3D) UB basin model. He

also simulated ground motions using the basin model to discuss the 3D effect on the surface ground motions. However, the detailed Vs structures in UB have not been validated since he developed two layers model with surface and bedrock layers. Due to the recent project of the Japan International Cooperation Agency (JICA) in UB city (City & Japan International Cooperation Agency, 2013), the results of PS-logging investigations and Spectral Analysis of Surface Wave (SASW) surveys at around 40 sites were reported. Since the explorations were up to 30m depth at the maximum, the intermediate and deeper Vs structures have not been elucidated.

Recently diffuse field assumption (DFA) has been proposed to understand MHVR by assuming a diffuse wavefield containing all types of elastic waves. In theory, MHVR can be numerically computed for the imaginary part of Green's functions, and the theoretical H/V ratio depends on underground layer thickness and elastic properties of soil. Hence the theory allowed to invert Vs profiles from MHVR. One of the authors also examined the applicability of the DFA for the MHVR-based Vs profiling and presented the validity of the technique for the site characterizations.

1. 1. 4. Building inventory

A building inventory might contain point- or polygon-like data with certain attribute fields such as address field, geographical coordinates, construction year. It is possible to group/classify the individual buildings based on common attributes. The definition of a classification system for the characterization of the exposed building stock and the description of its damage is an essential step in risk analysis in order to ensure a uniform interpretation of data and results (Erdik et al., 2011). For a general building stock, the following parameters affect the damage and loss characteristics: structural system; material and lateral-load-resisting system; height: number of floors; and construction year: to identify seismic design level.

Figure 1-4. Typical building photos in UB

Figure 1-4 shows the existing building types in UB collected during the visit for this study.

This study aims to develop a building inventory database in UB, including construction cost for each building in considering structural types, building heights, heating types, and other building characteristics in order to assess the buildings' vulnerabilities for a scenario earthquake economically. Although existing building inventory data is available in UB, structural types and construction years necessary for construction cost estimation and assignment of vulnerability functions are not fully registered in some buildings. I estimate the structural types, construction years, and heating types by criteria developed from the building characteristics in the inventory data.

1. 1. 5. Earthquake damage estimation

Building damage estimation methodologies can be divided into estimations based on fragility and vulnerability functions (Porter, 2015). The former method estimates probabilities of damage level for a building using the fragility function that represents the relationship between seismic excitation and damage probability. The Project for Strengthening the Capacity of Seismic Disaster Risk Management in UB City has conducted the building damage estimation in Ulaanbaatar city at 2013 (City & Japan International Cooperation Agency, 2013). Seismic excitation includes ground motion intensity or building response spectrum with damage probability for each damage state such as collapse, severe damage, moderate damage, and slight damage developed for various building structural types. In typical approaches of the method such as HAZUS, building damage probabilities were estimated from building responses derived by the spectral capacity method using demand curves of ground motions and capacity curves of buildings. In alternative approaches, building damage was estimated by empirical fragility curves developed from ground motion intensities and building damage statistics obtained in past damaging earthquakes (Matsuoka et al., 2014; Murao & Yamazaki, 2002). The fragility function-based approach can estimate the number of damaged buildings expected from predicted ground motion intensities.

The latter method estimates building loss based on vulnerability functions developed for each structural type (Dolce et al., 2006; Ferreira et al., 2013). Vulnerability functions represent the relationships between ground motion intensity and repair cost normalized by the replacement or construction cost. The normalized repair cost in percentile is expressed as the mean damage ratio (MDR) with variance in the vulnerability functions. Thus, the vulnerability functions can directly quantify the economic losses of buildings in earthquake scenarios. Recently vulnerability functions for various building structural types have been developed to globally assess the seismic risk of buildings (Yamin et al., 2014, 2017). If a database of construction costs for buildings in a target area is obtained, direct building monetary losses can be evaluated for an earthquake scenario using the

vulnerability functions (Yepes-Estrada et al., 2017).

Earthquakes are amongst the natural hazards responsible for the highest number of human casualties and economic losses throughout mankind's history. Recently the world's population reached the seven billion mark with the prospect of surpassing nine billion by the year 2050 (Silva 2013). The exponential growth in the world's population has led to an increase in the number of megacities (i.e., cities with a population larger than two million), many of them in earthquake-prone regions and potentially at risk (Crowley et al. 2006). In the past century alone, it has been estimated that, on average, nearly seventeen thousand people have lost their lives annually as a direct result of strong ground motion (Sen 2009). Seismic events have also had a significant impact on the economy at the country level and globally in recent years. For example, following M7 class Haiti's Earthquake in 2010, the total economic losses were estimated to be around 120% of the country's gross domestic product (GDP). In 2011 after the Great East Japan Earthquake, a worldwide rise in the prices of electronics was observed due to disruptions in the supply chain to several factories (Silva 2013).

1. 2. Objectives

This study aims to assess the earthquake loss estimation of Ulaanbaatar, Mongolia. It includes a wide area of research, that's why objectives have many types. The main objectives of this research are:

1. To demonstrate soil structural model of Ulaanbaatar city based on microtremor measurements
2. Strong motion prediction for the Emeelt fault
3. To develop building inventory data, including construction cost
4. Building damage and economic loss estimation of the city.

1. 3. Methods

Chapter 2 presents site effect estimation based on microtremor H/V spectral ratio of UB city. It includes single and joint inversion analysis compared with previous studies and geological borehole information. The shear wave velocity model of UB city and site amplification zoning is estimated in this chapter.

Chapter 3 describes earthquake response spectra on seismic bedrock of the Emeelt fault using the stochastic Greens function method. And it uses the shear wave velocity model of UB estimated in chapter 2 to consider site effect for surface ground motion spectra.

Building inventory development and cost estimation are included in chapter 4. The last part of the research has done in chapter 5. It has estimated building damage and economic loss estimation of UB. Furthermore, the total economic loss of the Emeelt faults earthquake results is estimated and discussed with the GDP of Mongolia.

Figure 1-5 shows the outline of the research. This research includes a wide range of research areas.

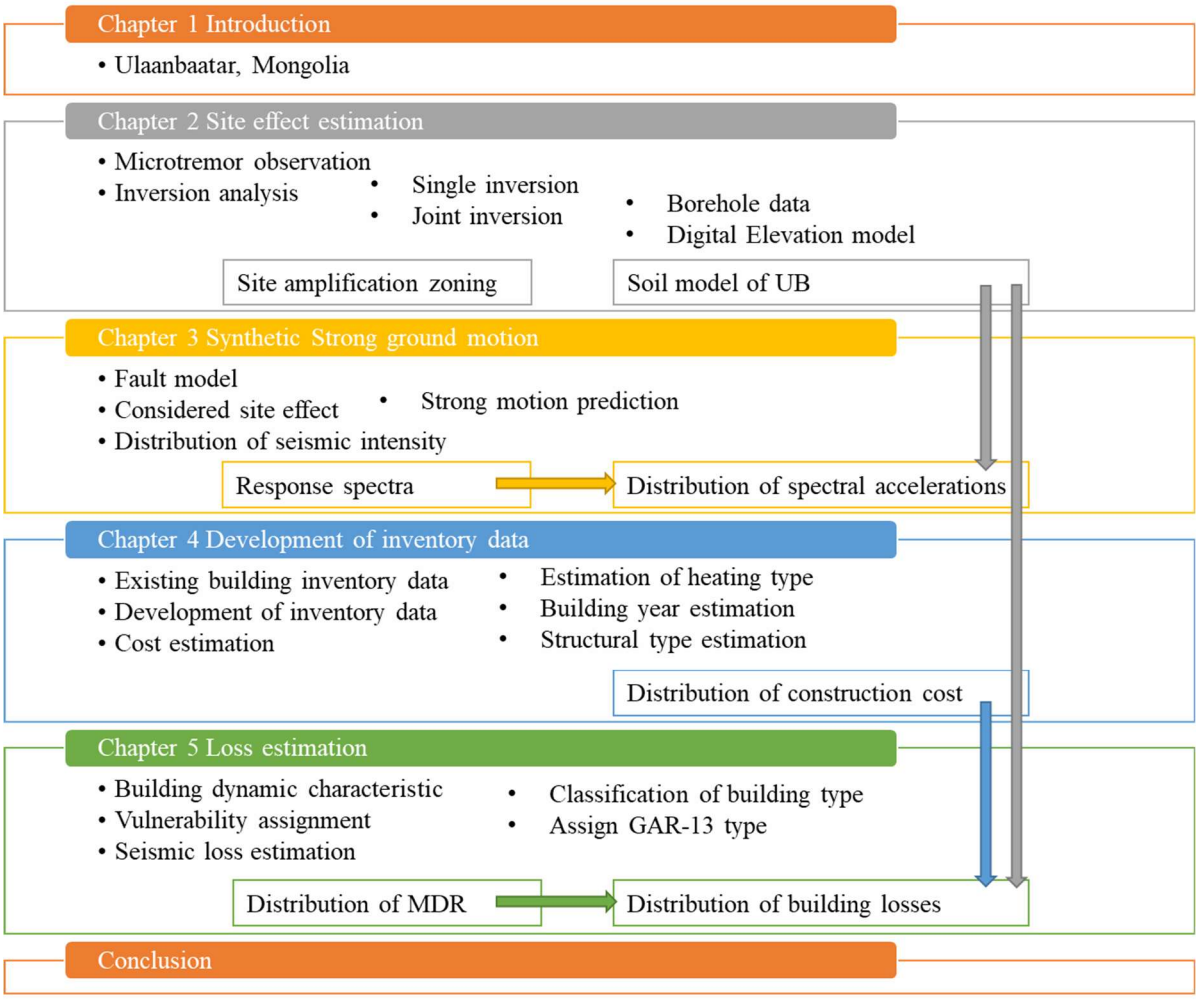

Figure 1-5. Outline of dissertation

CHAPTER 2. SITE EFFECT ESTIMATION OF MICROTREMOR H/V SPECTRAL RATIOS

2. 1. Introduction

Mongolia has been one of the most seismically active intracontinental regions in the world, with four large earthquakes with magnitudes of around 8 along with their active faults in the western part of the country during the last century (Munkhsaikhan, 2016). Compared with western Mongolia, central Mongolia, including Ulaanbaatar's region (UB), is considered a relatively low seismically active zone. Even though, according to the previous investigation (Munkhsaikhan, 2016), there are several active faults such as Hustai, Gunj, and Emeelt faults. In particular, the Emeelt fault earthquake with the estimated maximum magnitude of 7 (Oyun-Erdene et al., 2014) has been expected to significantly impact the UB region because the fault is located around 20km from UB.

In order to consider the disaster mitigation planning for such large earthquakes, the assessments of ground shaking intensities and building damage for scenario earthquakes are indispensable. Generally, the ground shaking intensity is determined by evaluating the source, path, and site effects. Especially the evaluation of site effects is essential because surface soil can generate significant ground motion amplification during earthquakes. The increase of the amplitude of seismic shaking can produce severe damage to buildings and infrastructures, accompanying a loss of lives. The basin UB located at the valley of Tuul river has 30km length and 4 to 10km width and is filled with alluvial deposits. According to borehole data and geological map, deposit thickness is around 10 to 80m in most areas, and the maximum depth is 120m expected around the Tuul Riverside (Chimed, 2011; V. I. et al., 2009). Since the population of UB city has grown around three times in the last two decades, the number of building constructions and densities are highly increased, and new construction districts have been expanded to everywhere of the city area. Especially in the last six years, moderate and high-rise buildings have been constructed near the Tuul Riverside, such as Zaisan, Yarmagiin Guur, and Shine Yarmag area (see Figure 2-1).

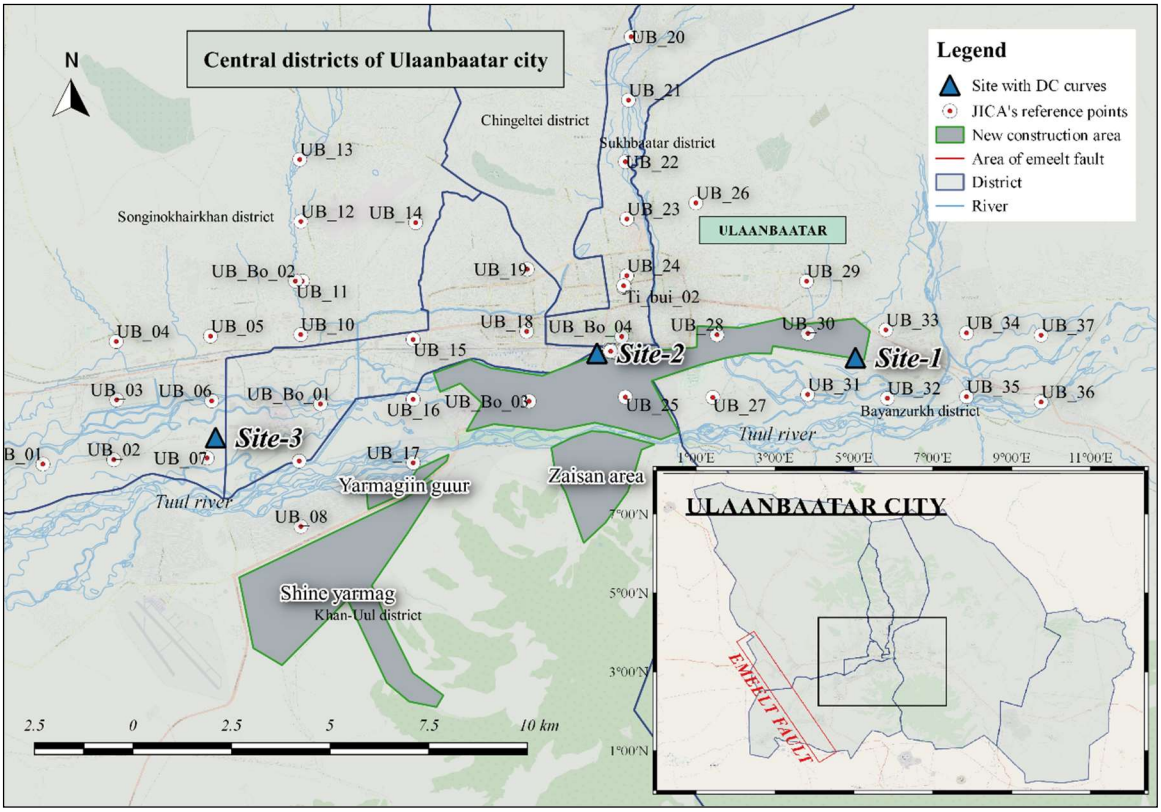

Figure 2-1. Location map of the study area with JICA's report reference points and the location of the Emeelt fault.

Odonbaatar (Chimed, 2011) performed microtremor array observations at three UB sites to identify the deep underground structures and estimate the three-dimensional (3D) UB basin model. He also simulated ground motions using the basin model to discuss the 3D effect on the surface ground motions. However, the detailed Vs structures in UB have not been validated since he developed two layers model with surface and bedrock layers. Due to the recent project of the Japan International Cooperation Agency (JICA) in UB city (City & Japan International Cooperation Agency, 2013), the results of PS-logging investigations and Spectral Analysis of Surface Wave (SASW) surveys at around 40 sites were reported. Since the explorations were up to 30m at the maximum, the intermediate and deeper Vs structures have not been elucidated.

Microtremors (ambient ground noise) is a low-cost and convenient method to estimate site

characterizations. For example, while horizontal motions are larger than vertical motion on the soft ground, both horizontal and vertical motions are similar to each other on the stiff ground. In particular, Horizontal-to-Vertical (H/V) spectral ratio technique, firstly proposed by Nakamura (Nakamura, 1989), has been utilized to evaluate the fundamental resonant frequency of grounds (Lachetl & Bard, 1994; Lermo & Chavez-Garcia, n.d.). Microtremor H/V spectral ratio (MHVR) has also been used to estimate Vs profiles by assuming that the microtremors are mainly composed of surface waves (Arai, 2005; Arai & Tokimatsu, 2004). Recently diffuse field assumption (DFA) has been proposed to understand MHVR by assuming a diffuse wavefield containing all types of elastic waves (Sanchez-Sesma et al., 2011). In theory, MHVR can be numerically computed for the imaginary part of Green's functions, and the theoretical H/V ratio depends on underground layer thickness and elastic properties of soil. Hence the theory allowed to invert Vs profiles from MHVR(García-Jerez et al., 2016; Kawase et al., 2018; Piña-Flores et al., 2017; Sánchez-Sesma, 2017). One of the authors also examined the applicability of the DFA for the MHVR-based Vs profiling and presented the validity of the technique for the site characterizations (Fujishima et al., 2018).

In this paper, we observe the microtremors at multiple sites in UB areas and apply the inversion technique to the MHVR to reveal the patterns of the Vs profiles considering the observations in the previous studies such as Odonbaatar and JICA's report (Chimed, 2011; City & Japan International Cooperation Agency, 2013; V. I. et al., 2009). Finally, the site amplification characteristics obtained from the estimated Vs profiles are discussed.

2. 2. Microtremor observation

In UB, around 5000 boreholes were explored by Russian and Mongolian research expeditions for geotechnical purposes before 1990. Although these data include some geotechnical information with laboratory tests, those data were surveyed at less than 10 m depth in most sites (Orkhon hydrogeology Co. Ltd., 2014). They did not include shear wave velocity information.

In the previous study by Odonbaatar, the microtremor array observations were performed at three sites in UB (Site 1, 2, and 3 in Figure 2-1) to estimate the deep underground structures. Since the estimated profiles were developed to create the UB basin model, the shallow Vs structures in the basin were not discussed in detail. Bedrock depth with the Vs of 1600 to 1800 m/s was determined at 40m to more than 100m depending on the location.

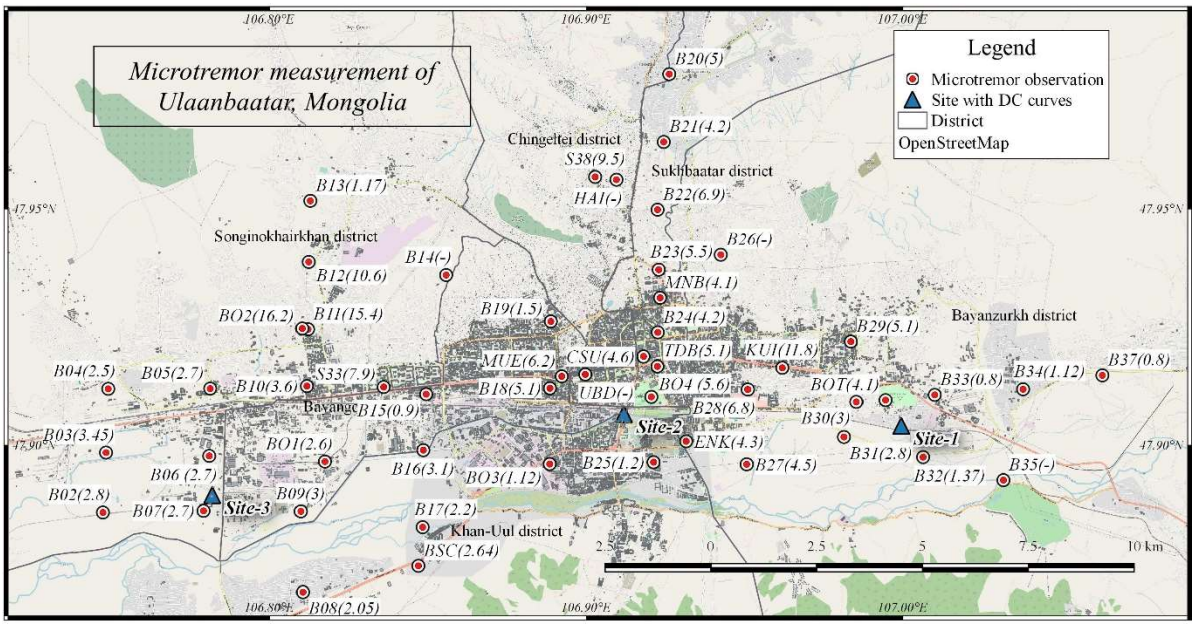

Figure 2-2. Microtremor observation points in Ulaanbaatar city. Values in brackets indicate peak frequencies identified from MHVRs.

In the JICA report, on the other hand, the Vs profiles were determined by PS-loggings at four sites (UB_Bo_01 to 04 in Figure 2-2) and the SASW method at 37 sites (UB_01 to 36 in Figure 2-2) in the

central UB area (City & Japan International Cooperation Agency, 2013). Since the depths of the Vs profiles are less than 30m and around 10m at most sites, deeper Vs structures have not been explored. It was never validated by other data sources such as MHVR. Furthermore, significant discrepancies between the Vs profiles derived by these two techniques were found even at the same site, indicating the uncertainty of the techniques. For those reasons, we conduct the microtremor observations at UB and apply the inversion technique to the observed MHVRs to derive the Vs profiles and evaluate the site amplification characteristics.

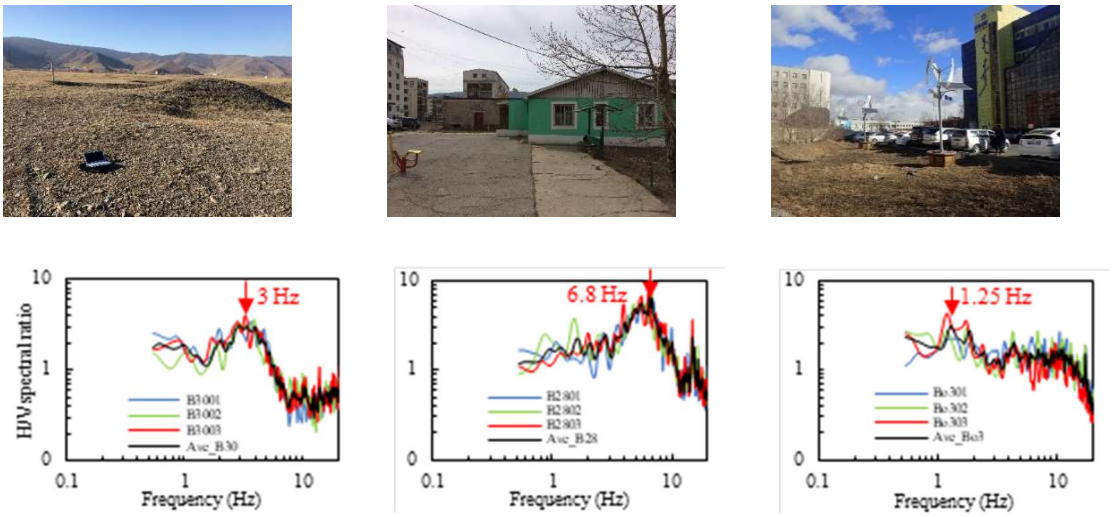

Figure 2-3. Typical site observation photos and observed H/V spectral ratios at B30, B28, and BO3.

The microtremors at more than 50 sites are measured by single-site observations in the city from March 25 to April 15, 2018. The locations of the observation sites are shown in Figure 2-2. The coordinates of the array observation sites in Odonbaatar's study and the JICA report sites are used for the observation, and we measure at the exact locations in most sites. Only a few sites are located in a special prohibited zone, such as UB city's pure water collecting zone. It was forbidden to enter that zone, so the microtremors were measured close to the target sites.

In the observations, we use the portable handheld microtremor sensor of GEODAQS-2S3D developed by ANET Inc., Japan. The sensor can measure the ambient ground motions in velocity with

the lower limit of the frequency of 0.5 Hz (period of 2.0 s). The sampling of 100 Hz is applied during the observation, indicating the frequency coverage from 50 Hz to 0.5 Hz. I have measured the microtremor at the ground's surface and recorded it for three to ten minutes. Due to the heavy traffic, the measurements are conducted in the early morning.

The Eq (2-1) calculates the MHVRs (HV_{obs}) shown below.

$$HV_{obs}(f) = \frac{\sqrt{NS(f)^2 + EW(f)^2}}{UD(f)} \tag{2-1}$$

Where the scripts NS and EW represent the Fourier spectrum for the north-south (NS) and east-west (EW) component respectively, while the UD corresponds to the up-down (UD) component in frequency f in Hz. The Parzen window with a bandwidth of 0.3 Hz is applied for the Fourier spectrum. Three 20.48 s duration parts with less traffic and artificial noises are extracted from the records, mean values of the three MHVRs are calculated.

The observation conditions and the observed MHVRs at the typical three sites are shown in Figure 2-3. The red number with an arrow indicates the peak frequencies of the MVHRs. The peak frequencies vary from 1.1 to 6.4 Hz, showing different site conditions in the city. The identified peak frequencies of the MHVRs are shown in the values in brackets in Figure 2-2. The peak frequencies are different at site by site. The northern locations such as B10, S38, B13, KUI, and B26 near the mountain have a higher frequency (10 to 15 Hz) or no peak. These results indicate shallow sedimentary depth or rock sites.

On the other hand, the lowest peak frequencies (2.4 to 5 Hz) are observed in most sites around the Tuul river basin, such as B03, B09, B25, and B32, probably due to the thick sediment. Besides, the peak amplitudes of MHVRs near the mountain sites are much lower than those at the Tuul riverside area. This result suggests that large site amplifications are expected in the Tuul riverside area.

2. 3. Inversion analysis of microtremor data

2. 3. 1. Joint inversion of H/V spectral ratio and surface wave dispersion curve

According to the previous inversion studies of MHVR (Arai, 2005; Sánchez-Sesma, 2017), joint inversion of MHVR and surface wave dispersion curve is more effective than a single inversion of MHVR to avoid the non-uniqueness of Vs and thickness during the Vs profile estimation. Therefore, the joint inversion of the MHVRs with dispersion curve obtained in Odonbaatar's microtremor array observations (Chimed, 2011) are applied at Site-1, 2, and 3.

First, I evaluate the estimated Vs profiles in Odonbaatar's study (OD models) by comparing theoretical H/V spectral ratio (HVR) with the observed MHVRs. The circles in Figure 2-4 (a) indicate the observed MHVRs. The data is resampled at equal intervals in a standard logarithm scale for the inversion analysis. The dotted lines in Figure 2-4 (a) show the theoretical HVRs computed from the OD models by the diffuse field theory at Site-1, 2, and 3. The observed phase velocities and Vs profiles of the OD models (Chimed, 2011) are shown by circles in Figure 2-4 (b) and dotted lines in Figure 2-4 (c), respectively. The dotted lines in Figure 2-4 (b) show the standard deviations of the phase velocities obtained from the array observations. As shown in Figure 2-4 (a), the theoretical values by the OD models do not match the observed MHVRs, especially at Site-2 and 3, suggesting that the OD models need to be modified using not only the dispersion curves but also the MHVRs.

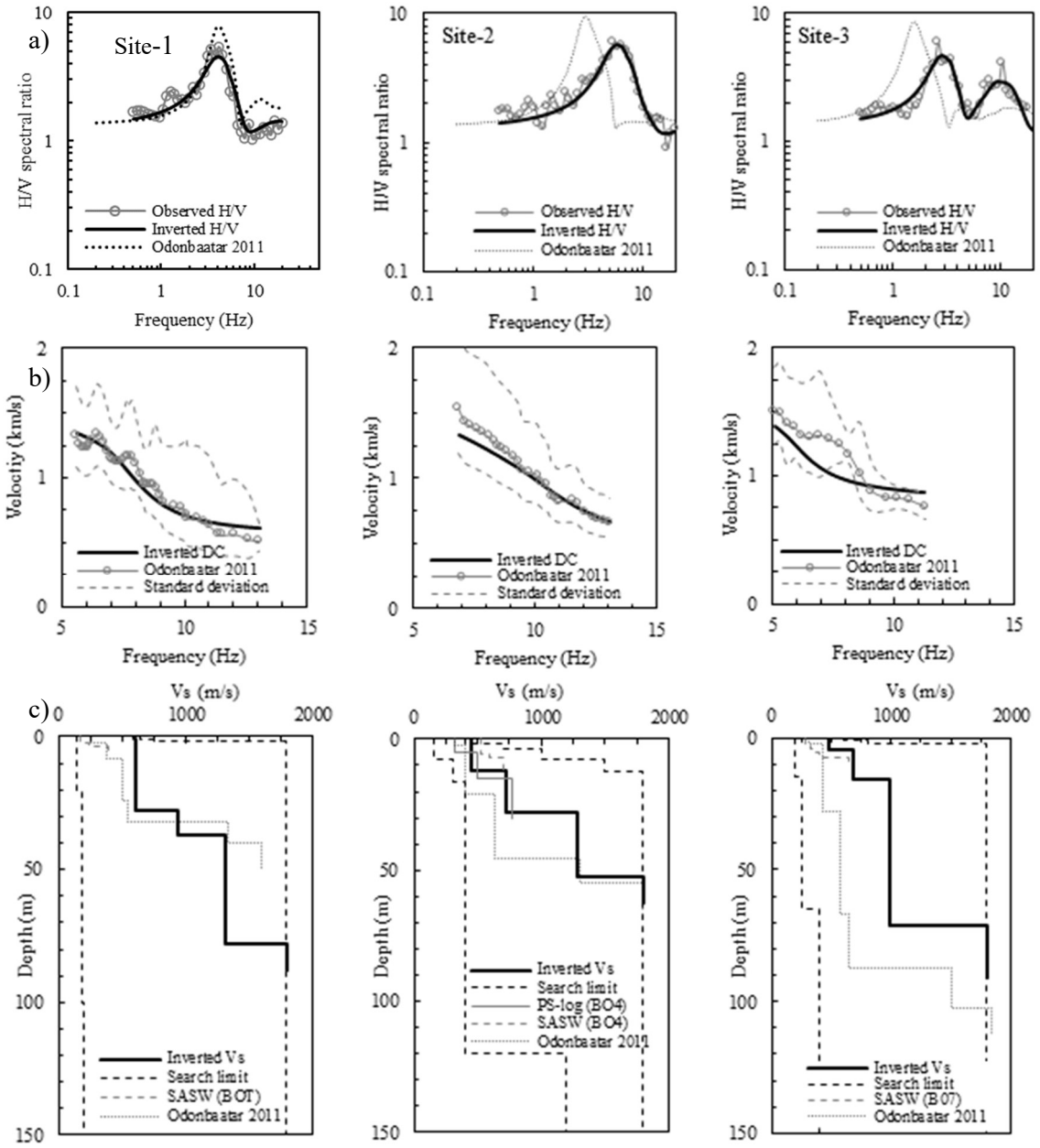

Figure 2-4. (a) Theoretical and observed H/V spectral ratio, (b) DC curve of joint inversion, and (c) Shear-wave velocity profiles of joint inversion at Site-1, 2, and 3.

Inversion technique requires search limits for the thickness and Vs for each soil layer generally based on geology, borehole, and geophysical test results. This study assumes search limits for each site considering the OD model for deeper structures and the JICA's report at the closest sites for shallower structures. The search limits for Site-1, 2, and 3 are shown in Table 2-1 to 3. The search limits are set to cover the existing models. The Vs of the lowest layers is fixed at 1800 m/s because the Vs of the bedrock was defined at around 1800 m/s in the OD models (Chimed, 2011), and the phase velocities were obtained up to about 1500 m/s in the dispersion curves as shown in Figure 2-4 (b).

Also, V_P and soil density for each layer require calculating theoretical HVR. Based on the previous PS-loggings in the JICA's report (City & Japan International Cooperation Agency, 2013), the relationship between Vs and V_P is modeled by linear regression analysis as shown in Equation (2-2).

$$Vp = 0.00162Vs^2 + 1.403Vs + 14.9 \tag{2-2}$$

The Equation (2-2) is used to set the search limit for V_P in the inversion analysis for the layer of Vs of less than 800 m/s because the shallow Vs structures up to the Vs of around 800 m/s were obtained in the JICA's report. If the Vs is higher than 800 m/s, the relationship developed by Kitsunezaki et al. (KITSUNEZAKI, 1990) shown in Equation 2-3 is applied.

$$Vp = 1.11Vs + 1290 \tag{2-3}$$

Soil density for each layer is assumed at general values as shown in Table 2-1 to 3.

In this study, the Simulated Annealing method (Kirkpatrick et al., 1983) is applied during the inversion analysis because it was already successfully applied in invert dispersion curves and MHVR (Sánchez-Sesma, 2017). I performed 10 inversions per site with different initial sets of randomly-

generated models and selected the best structure with the smallest misfit (best fit model).

Misfit between the theoretical and observed values in MHVR and dispersion curve is minimized in the joint inversion process. Misfit Γ is defined Equation 2-4 as shown below.

Table 2-1. Initial inversion parameter ranges for Site-1

Layer	Thickness (m)	Vs (m/s)	V_P (m/s)	Density (kg/m^3)
1	0-20	200-600	350-1400	1600-1800
2	0-80	250-800	450-2400	1700-1900
3	0-100	400-1200	830-2600	1800-2000
4	0-100	1200-1500	2600-2950	1900-2100
5	-	1800	3280	2000-2200

Table 2-2. Initial inversion parameter ranges for Site-2

Layer	Thickness (m)	Vs (m/s)	V_P (m/s)	Density (kg/m^3)
1	2-8	200-500	360-1120	1600-1800
2	2-8	300-700	580-1790	1700-1900
3	4-104	400-1000	830-2400	1800-2000
4	4-100	1200-1500	2620-2950	1900-2100
5	-	1800	3280	2000-2200

Table 2-3. Initial inversion parameter ranges for Site-3

Layer	Thickness (m)	Vs (m/s)	V_P (m/s)	Density (kg/m^3)
1	2-8	160-600	280-1400	1600-1800
2	2-8	300-700	580-1790	1700-1900
3	4-104	400-1000	830-2400	1800-2000
4	4-100	1200-1500	2600-2950	1900-2100
5	-	1800	3280	2000-2200

$$\Gamma = \frac{2(1-\xi)}{n}\sum_{i=1}^{n}\frac{(HV_{obs}(f_i)-HV_{th}(f_i))^2}{HV_{obs}{}^2(f_i)} + \frac{2\xi}{m}\sum_{i=1}^{m}\frac{(DC_{obs}(f_i)-DC_{th}(f_i))^2}{DC_{obs}{}^2(f_i)} \quad \text{(II-4)}$$

Where ξ=n/(n+m) is the cost function, n number of data with H/V spectral ratio is 41 at each site, and m number of data with dispersion curve is different for each site. Because the number of data in the obtained dispersion curves varied, m=42 at Site-1, m=27 at Site-2, and m=16 at Site-3 are used. Even if the number of data both observables is not the same, the cost function does not change (García-Jerez et al., 2016). H/V_{obs} and H/Vth represent the target measurements and calculated MHVRs for the current model in a frequency fi. DC_{obs} and DC_{th} are the experimental measurements

and the estimated dispersion curve for the current model.

In the preliminary analysis with the cost function of 0.5, the observed and inverted MHVRs showed a significant difference. Therefore, the cost is changed to 0.8 to increase the weight for the MHVR than for the dispersion curve. The results of the inversions are shown in solid thick lines in Figure 2-4. The solid lines in Figure 2-4 (a) and (b) indicate the theoretical values obtained from the inverted Vs profiles shown in Figure 2-4 (c). The theoretical values show good agreement with the observed values, especially showing better agreement for the MHVRs than the OD models.

On the other hand, the theoretical dispersion curves show lower agreement with the observed values than those by the OD models, especially at Site-3. This difference indicates that it is difficult to find a model that accurately reproduces both observation data. Considering the variability of the dispersion curve at Site-3, we accepted the inversion result since the theoretical values are within the standard error (mean plus-minus one standard deviation).

The estimated bedrock depths vary 50 to 80m, showing more considerable depths at Site-1 and 3 than at Site-2. Since Site-1 and Site-3 are located near the Tuul river as shown in Figure 2-1, larger sediments are expected in the Riverside area than in the central UB such as Site-2.

2. 3. 2. Single inversion of H/V spectral ratio

In this part, a single inversion analysis is applied to the observed MHVRs to estimate Vs profiles at the observation sites except for Site-1, 2, and 3. Blind single inversion can be quite costly because it may imply a vast search within the parameter space, and the convergence can require a long time or even not be reached. In order to sharpen the search of solutions, we define search limits of target values using existing shallow Vs profiles (City & Japan International Cooperation Agency, 2013) with the previous joint inverted results for deep underground structures. For example, a typical site search limit compared with JICA's report is shown in Table 2-4.

In the single inversion, the misfit Γ_{HV} was defined in Equation 2-5 as below:

$$\Gamma_{HV} = \sum_{i=1}^{n} \frac{(HV_{obs}(f_i) - HV_{th}(f_i))^2}{HV_{obs}{}^2(f_i)} \tag{2-5}$$

Where HV_{obs} and HV_{th} represent target measurements and calculated MHVR for a current model at frequencies f_i (Sánchez-Sesma, 2017).

Table 2-4. Initial inversion parameter of the typical site (UB25).

	JICA's report		This study	
Layer	**Thickness (m)**	**Vs (m/s)**	**Thickness (m)**	**Vs (m/s)**
1	0-4	207-323	0-20	150-500
2	0-6	436-703	0-50	180-1000
3	-	-	0-100	600-1500
4	-	-	-	1800

The H/V spectral amplitudes have no peak or are smaller than a factor of 2 at a few sites located in the mountain areas. These sites are eliminated in the inversion process because it would be difficult to accurately estimate Vs profiles due to the uncertainties during the inversion analysis. Figure 2-5 shows the observed and inverted MHVRs of 40 sites.

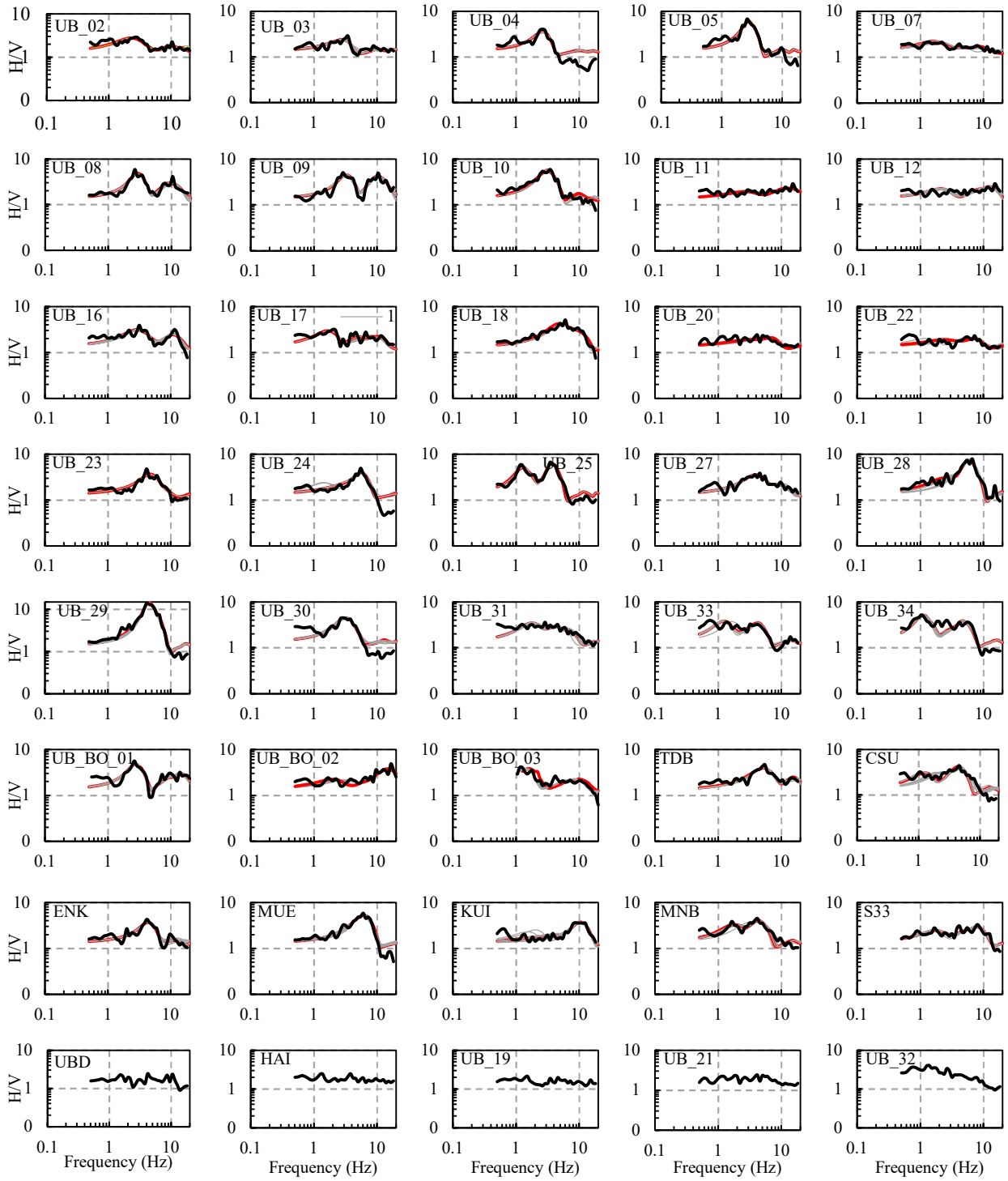

Figure 2-5. Observed and theoretical MHVRs obtained by single inversion; Black line indicates observed MHVR; Red line indicates inverted best MHVR; Gray lines indicate inverted models. The bottom row figures show no peak and have not inverted.

The black line indicates the observed MHVRs, the red line indicates inverted best results of MHVRs, and the gray line shows the results of other inverted models. At most of the sites, the misfits of the inversion process are negligible. It is considered that the difference between the observed and inverted MHVRs is similar in shape and amplitude. Figure 2-6 shows the inverted Vs profiles of the sites in UB. The Vs profiles are up to 160m depth in most sites.

In some sites such as UB_08, UB_33, UB_34, and UB_Bo_03, the bedrock depths are estimated at around 200m depth is slightly deeper than those expected in the previous research (Chimed, 2011; V. I. et al., 2009) because the predominant frequencies are found at approximately 1 Hz or less. Since the information for the deeper underground structures in UB is very limited, further detailed observations such as much larger-scale microtremor array observations would be required to justify the deeper parts of the estimated Vs profiles.

The main objective of this study is to evaluate the site effects in the UB area. To discuss the effect of the bedrock depth on site amplifications, sensitivity analysis is performed by using the estimated Vs profile in UB33, where the estimated bedrock depth is 203m. Table 2-4 shows the Vs profile estimated in UB33. I prepare the other three models (Model-1, 2, and 3) by changing the thickness of the third layer from 98m to 80m, 60m, and 40m. The bedrock depths of the three models correspond to 185m, 165 m, and 145 m, respectively. The site amplifications are calculated from the four models by the one-dimensional elastic wave propagation theory of SH-wave (Haskell, 1960). The damping factor of 0.03 is given to all the layers. Figure 2-7 shows the calculated site amplification for the models. The amplification factors around 1.0 Hz are slightly shifted to a higher frequency by reducing the thickness of the third layer. However, the site amplification factors among the models are pretty small and negligible. It indicates that the thickness of the deep layers does not influence site amplifications.

2. 4. Shear wave velocity structure

2. 4. 1. Shear wave velocity structure

Shear wave velocity structure is shown in this part. There are 40 sites estimated shear wave velocity structure in UB. Based on these results, I can create the soil model of UB city, which is essential part of site effect assessment.

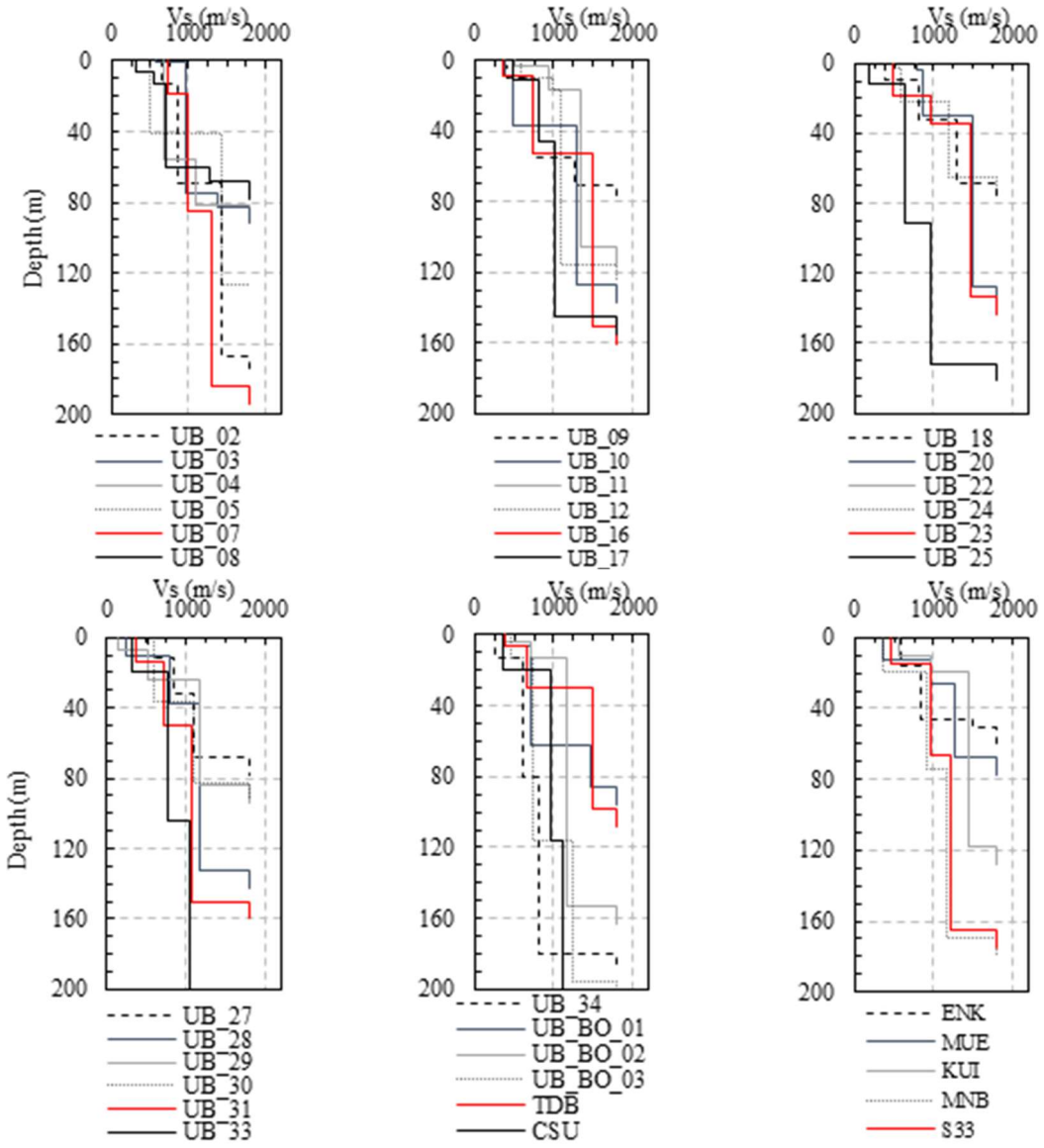

Figure 2-6. Estimated shear-wave velocity profiles of all sites obtained from microtremor single inversion

2. 4. 2. Comparison with borehole data

According to the borehole data, the soil consists of gravel with clay or sand in upper layers and weathered shale or rocks in lower layers. The thickness of the inverted layers almost corresponds to the boundaries of the soil types in the borehole. The Vs corresponding to the gravel with clay and sand layers are 400 to 1000 m/s, while the Vs corresponding to the weathered shale and rock are 1000 to 1500 m/s. The results show some justification for the inverted shallow Vs structures.

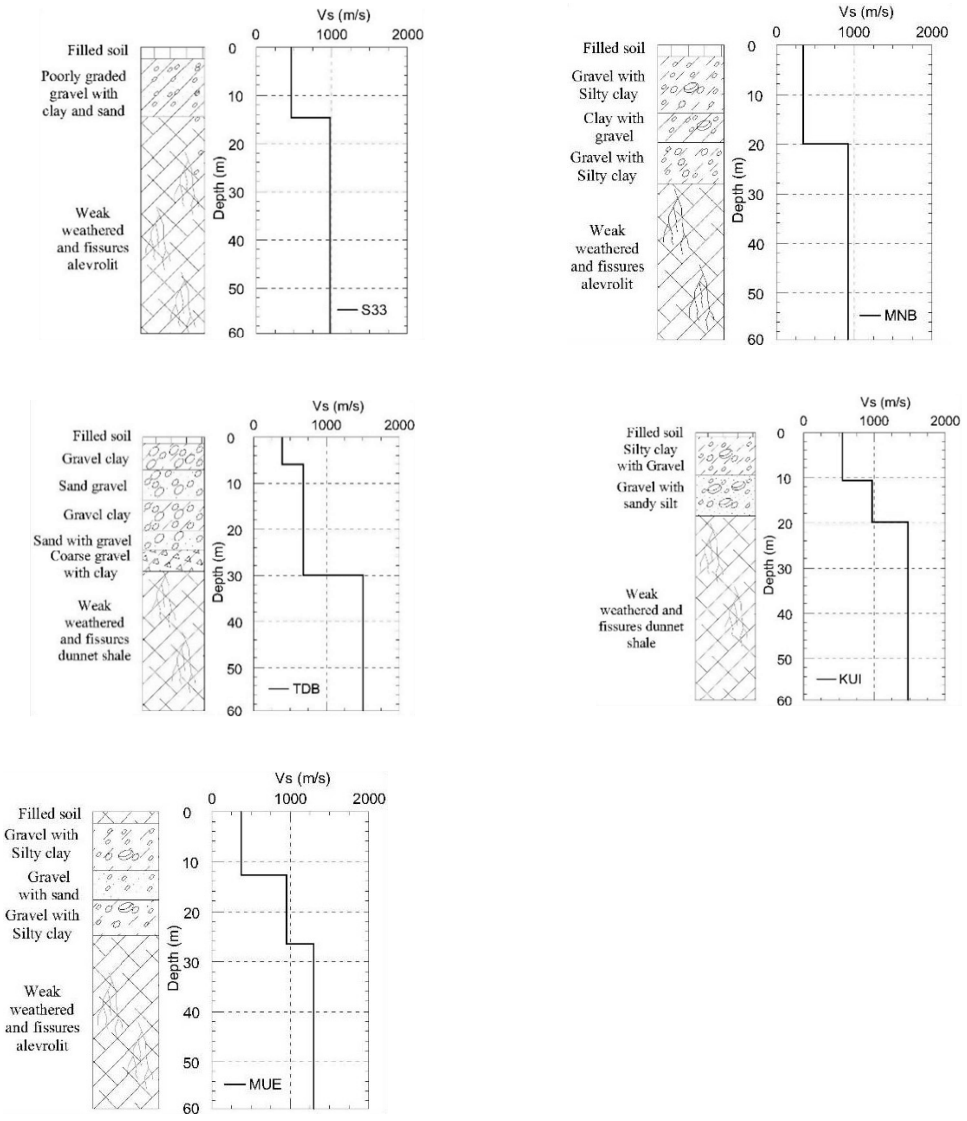

Figure 2-7. Comparison of estimated shear-wave velocity profiles and existing borehole data

2. 5. Vs30 distribution in UB

2. 5. 1. Vs_{30} distribution in UB

Time-averaged shear-wave velocity in upper 30 m depth (Vs30) has been used to index site characteristics in many applications such as ground motion prediction equations, building codes, and earthquake hazard maps. To evaluate the pattern of Vs30s in UB, the Vs30s are calculated from the Vs profiles inverted in the previous section.

Figure 2-8 (a) shows Vs30 distribution with a Geotechnical map of UB (Orkhon hydrogeology Co. Ltd., 2014). According to this map, the UB basin has consisted mainly of Alluvium, Alluvium-Diluvium, Fluvial deposits, and the northern part has consisted of Neogene. The geological period of deposits is mostly Quaternary; an epoch is Holocene to Pleistocene. Bedrocks have mainly consisted of carboniferous shallow marine sedimentary rocks and Devonian to Carboniferous accretionary complex. Along the Tuul river, it is covered by sediments of sand, gravel, and mud transported by the rivers. Also, Selbe, Uliastai, Bilgekh, and Tahilt rivers are located around Ulaanbaatar city. All these rivers are affected boundary of deposits and geotechnical conditions UB basin.

Figure 2-8 (b) shows the map of Vs30 distribution in UB paired with 7.5-arcsecond resolution digital elevation model (DEM) of the Global multi-resolution terrain elevation data 2010 (Danielson & Gesch, n.d.). The elevation in Ulaanbaatar's central area is 1280 to 1350 m above sea level, and those in the northern and southern mountains are higher than 2100 m.

More significant Vs30 sites (larger than 750 m/s) are located near the mountain, including UB20, UB22, KUI, and UB11. Smaller Vs30 sites (less than 450 m/s) are distributed in the lower elevation area. Especially the Vs30s smaller than 450 m/s are expected near the Uliastai river, such as UB34, UB33, and UB29 located in the eastern part of UB. In the central part of UB, the Vs30 with 450 to 600 m/s are distributed, such as CSU and TDB. Most of the sites in UB are classified to class C or B in the NEHRP Vs30 categories (Building Seismic Safety Council (BSSC), 2009), indicating that the site conditions are stiff and almost no very soft soils are expected in UB.

2. 5. 2. Site effect assessment

Concerning seismic hazard, fundamental questions are whether a high seismicity rate represents what we may expect in the future and the hazard assessment with smaller but more frequent events. Site effects characterized by site amplification would be necessary for seismic hazard mapping, and microzoning would also be convenient for understanding site amplification patterns. In this study, the microzonation in UB is evaluated based on the site amplifications calculated from the inverted Vs profiles.

Considering the locations of the sites and major rivers in UB, the elevation map, the geological conditions (Orkhon hydrogeology Co. Ltd., 2014), and the similarities of the calculated site amplification, we divided the UB area into five zones, as shown in Figure 2-10. The distribution of the average site amplifications for 1-1.25 Hz, 3.33-5 Hz, and 6.67-10 Hz in the sites are displayed in Figure 2-9. The theoretically calculated site amplification in the zones is shown in Figure 2-10. Zone-I is located in the western part of the UB basin and north of Tuul river, showing more significant amplification in 3 Hz. Zone-II is in the south-western part of UB and south of the Tuul river. Recently newly developed built-up areas have been expanded to this zone. Moderate to small amplifications are expected in the zone.

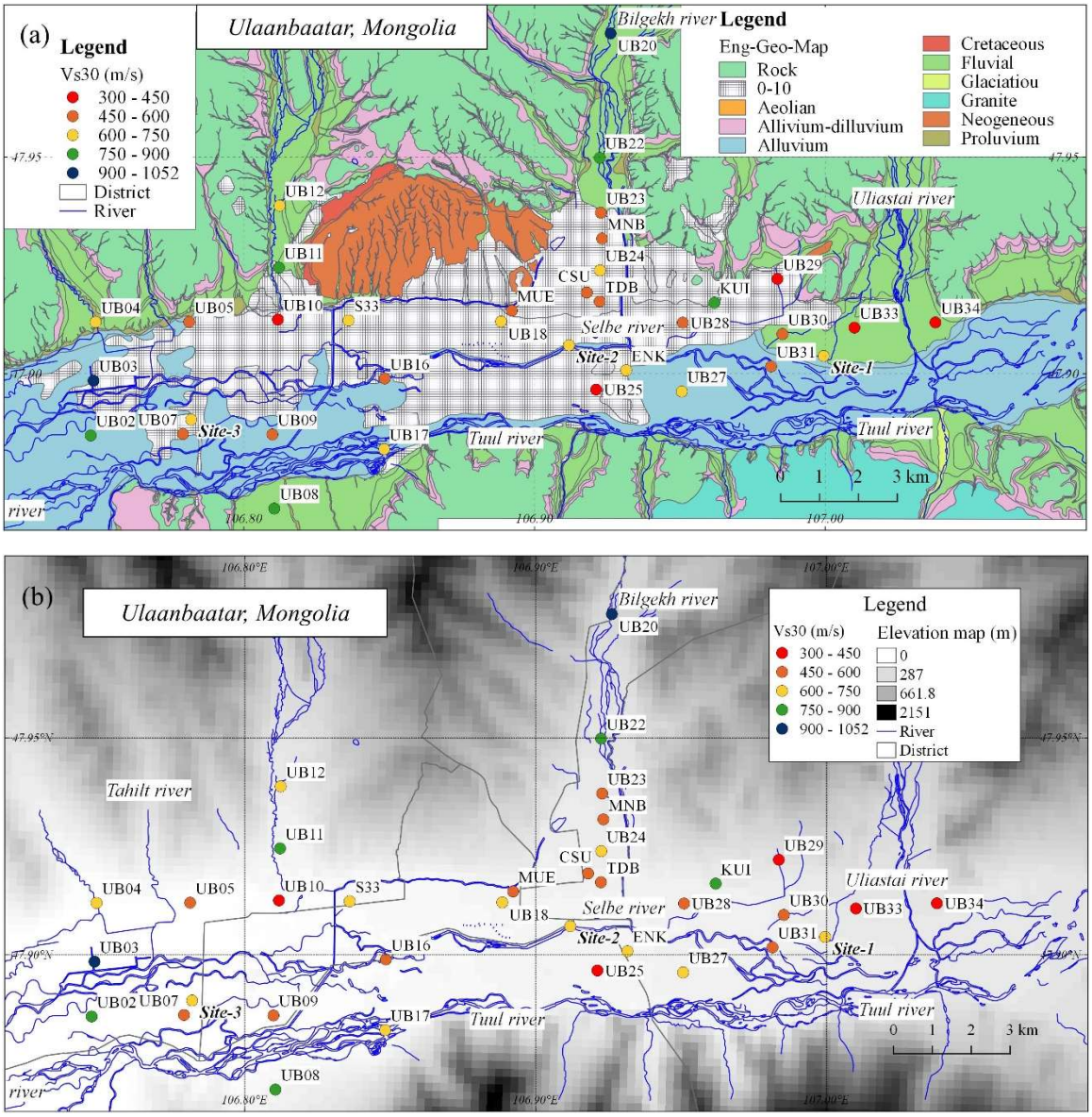

Figure 2-8. (a) Vs30 distribution map with Geotechnical map (Orkhon hydrogeology Co. Ltd., 2014)
(b) Vs30 distribution map with digital elevation model (DEM)

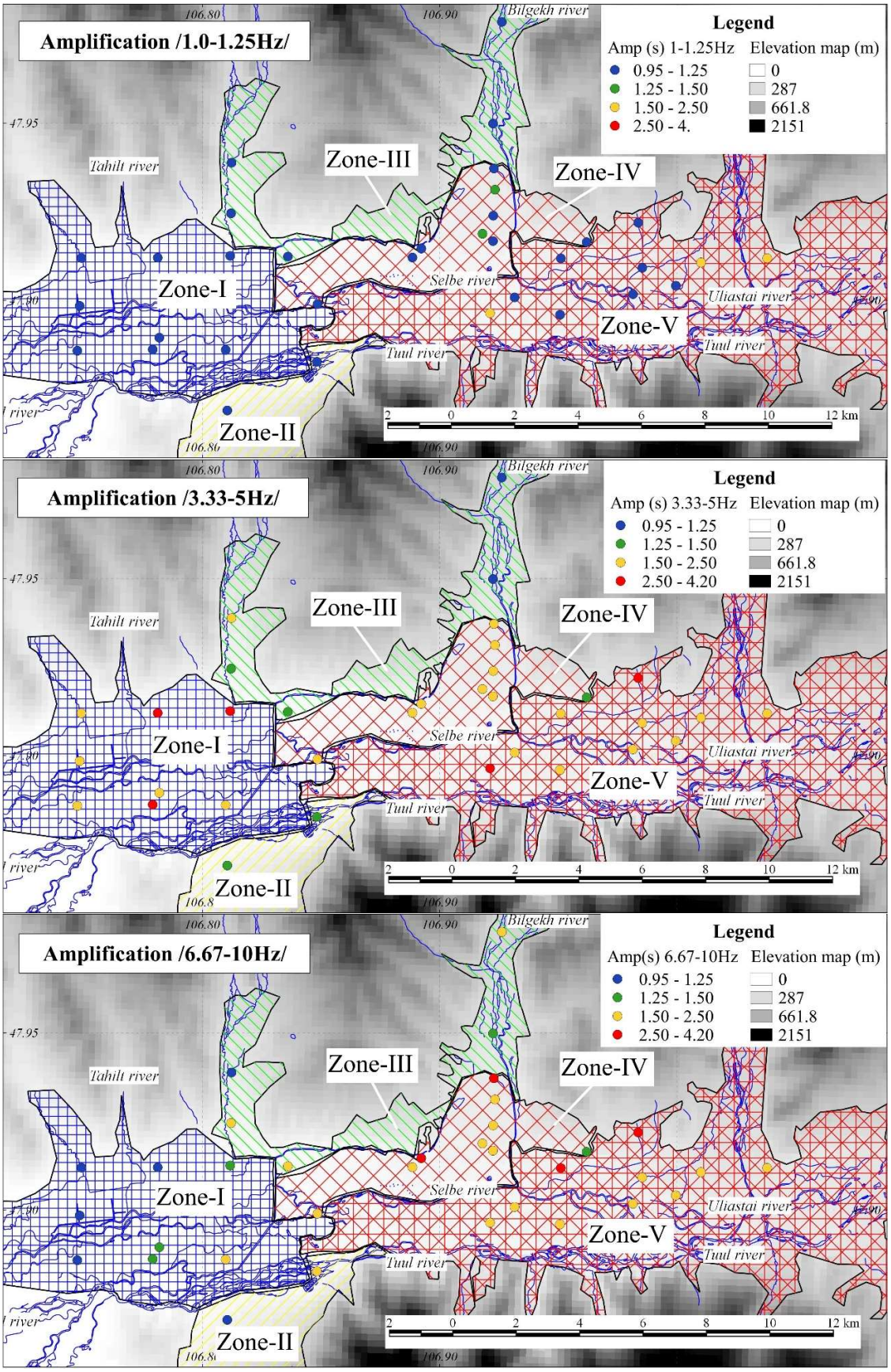

Figure 2-9. Site amplifications for common frequencies with Zoning map.

Zone-III is located in the northern part of UB along the Bilgekh and Selbe rivers. As described above, these sites are located in higher elevation zone, and the Vs30s are also larger than other areas. Small amplifications are expected for all frequency ranges in the zone. Zone-IV includes the central part of UB located in the north of the Selbe river. Intermediate to large amplifications is calculated for 4 to 10 Hz. Zone-V covers the eastern and southern parts of UB. This zone contains major rivers such as Uliastai and Tuul rivers. Since the smaller Vs30s are estimated in the zone, the highest amplification is obtained in UB, especially for the frequencies higher than 3 Hz. Since thick sediments are determined in the zone as discussed above, more vigorous ground shaking would be excited in future earthquakes. In particular, newly urbanized areas have been expanded to the area of Zone-V, indicating that it might be a higher risk in such new construction districts.

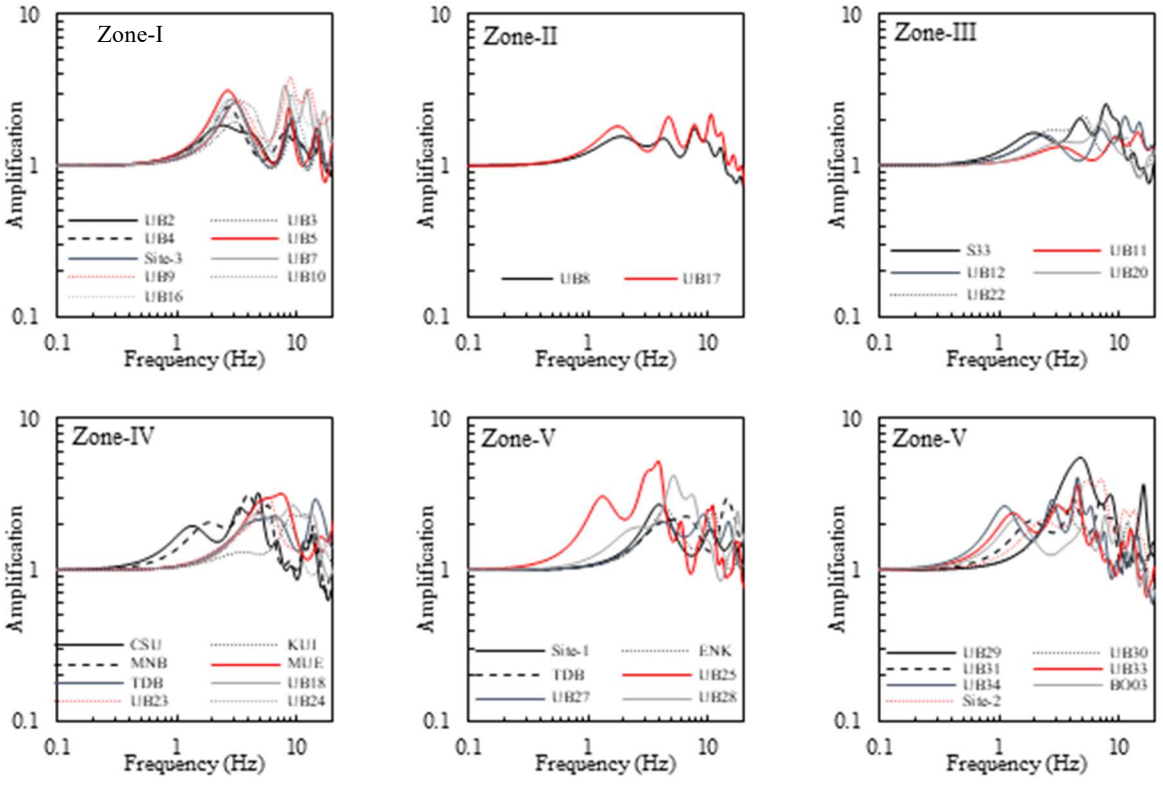

Figure 2-10. Theoretical site amplification for each zone in UB

2. 6. Conclusion

In this chapter, the shear-wave velocity (Vs) profiles in Ulaanbaatar (UB) city are estimated from the inversion analysis of the observed microtremor H/V spectral ratios (MHVRs) based on the diffuse field assumption. The joint inversions of the MHVRs and the surface wave dispersion curves obtained in the previous study are applied to the three sites in UB. The single inversion of the MHVRs estimates the Vs profiles for the rest of the sites. A comparison between the inverted shallow Vs profiles and the geological borehole information has shown that reliable results within the methods' capabilities and resolution could be achieved.

Finally, the seismic microzoning is performed based on the site amplifications obtained from the inverted Vs profiles. The UB areas are divided into five zones considering the site characterizations. The most significant site amplifications are expected around the Tuul river area, which consists deepest sedimentary deposit. Especially the Zone-V is the highest site amplified area, which means the significant risk for a newly constructed building district. Strong ground motion predictions and building damage estimation for scenario earthquakes based on the site characterization of this study would be performed in future works.

CHAPTER 3. SYNTHETIC STRONG GROUND MOTION DUE TO SCENARIO EARTHQUAKE

3. 1. Introduction

Mongolia has been one of the most seismically active intracontinental regions in the world, with four large earthquakes (magnitude around 8) along its active faults in the western part of the country during the last century (Munkhsaikhan, 2016). Compared with western Mongolia, central Mongolia, including Ulaanbaatar's region (UB), is considered a relatively low seismically active zone. Even though, according to the many articles, there are several active faults, such as Hustai, Gunj, and Emeelt faults under 100km from UB. Collaborated researcher's team, which included the Institute of Astronomy and Geophysics (IAG) and France researchers worked on the Emeelt fault area since 2005. It became the trending topic of Mongolian geophysical researchers to develop highly sensitive seismic stations around UB. According to the area of Emeelt fault explorations (Munkhsaikhan, 2016; Oyun-Erdene et al., 2014), the estimated maximum moment magnitude Mw=7 indicates significant risk for UB's population. Therefore, estimation of strong ground motion for UB is an essential part of the earthquake disaster.

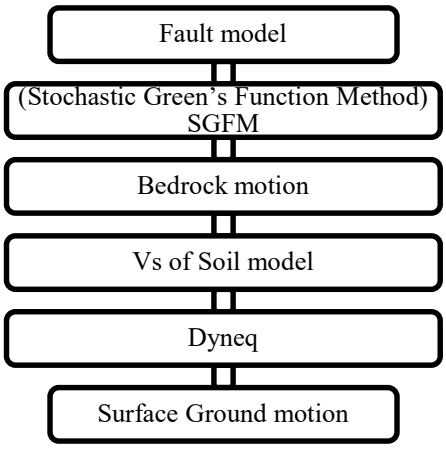

Figure 3-1. Flowchart of estimation of synthetic ground motion

Empirical Green's Function Method (EGFM) has been employed to simulate strong ground

motions for scenario earthquakes when appropriate ground motion data for small earthquakes is available (Irikura, 1986). To extend the EGFM to the cases in that any observed record of small earthquakes is not available, a way to calculate them based on the stochastic theory has been developed. This calculated small earthquake's record is called Stochastic Green's Function (SGF) (Boore, 1983). The way to synthesize strong-motion using the SGF is called the Stochastic Green's Function Method (SGFM). Figure 3-1 shows general steps to estimate strong ground motion considered site characteristics applied in this paper.

3. 2. Methodology

3. 2. 1. Stochastic Green's Function Method

This method is to generate time series which is considered frequency filter; physical approximates with spectrum window, prescribed stress parameters, seismic moment and so on. Synthetic ground motion model by Boore (Boore, 1983) was used for determining rock level synthetic acceleration-time history. The Fourier amplitude spectrum of ground motion at a site is expressed in terms of source and wave propagation functions and is given in Eq. (3-1).

$$A(\omega) = CM_0 S(\omega, \omega_c) P(\omega, \omega_m) \frac{e^{-\omega R/2Q\beta}}{R} \tag{3-1}$$

C and M_0 are the scaling factors and seismic moment (dyne-cm).

$$C = \frac{R_{\theta\phi} \cdot FS \cdot PRITITN}{4\pi\rho\beta^3} \tag{3-2}$$

Where, $R_{\theta\phi}$ represents the radiation pattern for a range of azimuths θ and takeoff angles ϕ. FS accounts for the free surface effect. $PRTITN$ is the reduction factor that accounts for the partitioning of energy into two horizontal components and R is the hypocentral distance. ρ and β are crustal density and shear wave velocity.

The source spectrum, the ω-square model used in this study, is given by

$$\text{Source } S(\omega, \omega_c) = \frac{\omega^2}{1 + (\omega/\omega_c)^2} \tag{3-3}$$

Here, ω_c is corner frequency, and the value of ω_c is obtained from $f_c = \omega_c / 2\pi$. The $P(\omega, \omega_m)$ in equation (3-1) is a high-cut filter that accounts for the observation that acceleration spectra often show a sharp decrease with increasing frequency, above some cut-off frequency ω_m (*84.82rad/s*) is used.

$$P(\omega,\omega_m)=\left[1+\left(\omega/\omega_m\right)^{2s}\right]^{-1/2} \tag{3-4}$$

In equation (3-4), s controls the decay rate high frequencies and assigned 4 (Boore, 1983). Also, M_0 and ω_c these two source parameters, can be related through an equation involving another parameter with dimensions of stress.

$$f_c = 4.9 \times 10^6 \beta\left(\Delta\sigma / M_0\right)^{1/3} \tag{3-5}$$

Where f_c is in Hertz, β is in km/s, $\Delta\sigma$, the stress drop in bars, and M_o is dyne-cm.

Synthesis of strong ground motions during a large earthquake is computed by the Empirical Green's function (Irikura, 1986), shown in equation (3-6). *U(t)* target event is expressed in terms of the seismogram $u_{ij}(t)$ of the subevent as follows:

$$U(t)=\sum_{i=1}^{N}\sum_{j=1}^{N}\frac{r}{r_{ij}}F\left(t-t_{ij}\right)\cdot u_{ij}\left(t\right) \tag{3-6}$$

Where r is the hypocentral distance from the observation point to subevent, r_{ij} distance to i, j-th subfault, *F(t)* is filtering function to adjust the difference in slip time function between the target event and subevent.

$$t_{ij}=\frac{\left(r_{ij}-r_0\right)}{V_s}+\frac{\xi_{ij}}{V_R} \tag{3-7}$$

Where ξ_{ij} is the distance from rupture nucleation point to the i, j-th subfault, V_R rupture speed, *Vs* is the seismic wave velocity.

$$F(t)=\delta(t)+\frac{1}{n'}\sum_{k=1}^{(N-1)n}\delta\left[t-(k-1)\frac{\tau}{(N-1)n'}\right] \tag{3-8}$$

Where τ is the rise time of the target event, n' is an appropriate integer to eliminate spurious periodicity.

3. 3. Fault model

Strong ground motions in the target area for a scenario earthquake are estimated by the simulation techniques based on the stochastic Green's function method (SGFM) and the equivalent linear seismic response analysis. The SGFM consists of a simulation of the ground motions generated from sub-faults (small events) (Boore, 1983) in an anticipated large earthquake fault and a summation of the generated ground motions in the smaller events (Irikura & Miyake, 2011; Kamae et al., n.d.). The method can create the synthesized strong ground motions at arbitrary sites on seismic bedrock (approximately shear-wave velocity of 3 km/s) and has been widely used in current strong ground motion predictions. To estimate the ground motions at the ground surface, site amplification of the surface soils needs to be considered. The authors already estimate the underground shear-wave velocity structure models at approximately 50 sites in the UB area by the inversion analysis of the observed microtremor data (Tumurbaatar et al., 2019).

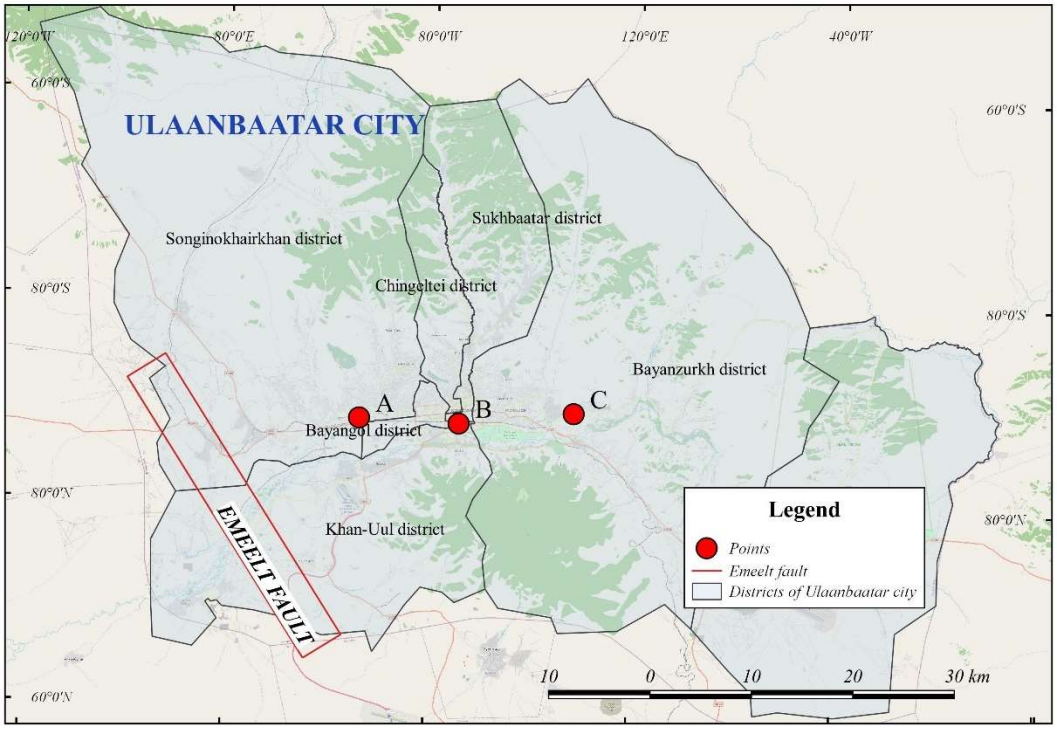

Figure 3-2. Locations of Emeelt fault model and site A-C.

I apply the equivalent linear seismic ground response analysis of DYNEQ (Yoshida et al., 2002) to the estimated ground motions at bedrock and the shear-wave velocity models to consider the nonlinear response of strong shakings. Finally, we estimate the distribution of spectral accelerations for the scenario by interpolating the estimated ground motion intensities.

Table 3-1. Input fault parameters and properties for SGFM.

Fault parameters:		**Asperity parameters:**	
Moment magnitude	M_w=7.4	Moment of asperity	M_{wa}=6.6
Seismic moment	M_0=2.43E+19 N*m	Seismic moment of asperity	M_0=1.07E+19 N*m
Length of fault	L=35 km	Length of asperity	l=16.4 km
Width of fault	W=16.3 km	Width of asperity	w=7.62 km
Strike	N150E deg.	Average stress drops of asperity	D_{sa}=1.99E+07 Pa
Dip	72 deg.		
Upper limit	3 km		
Average stress drop	D_s=4.37E+06		
Constant stress parameter	$\Delta\sigma$ = 199 bars		
SGFM parameters:			
Frequency-dependent path	Q = 204 f $^{0.65}$	Shear wave velocity	Vs = 3.4 km/s
Crustal density	ρ = 2700 kg/m^3	Reduction factor	$PRTITN$= 0.71
Radiation pattern	$R_{\theta\phi}$ = 0.63	Free surface factor	FS = 2.0

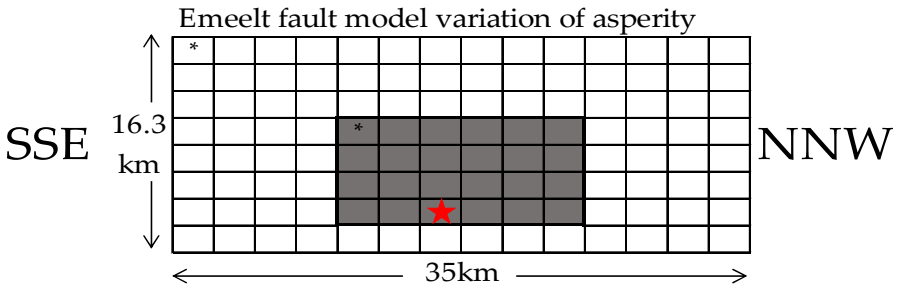

Figure 3-3. Characterized variations of the Emeelt fault model. Grids represent the sub-faults of the earthquake. The dark area indicates the asperity area in the fault. Asterisks and star represent the origins of the background and the asperity, and the rupture starting point, respectively.

I selected the Emeelt fault as the scenario earthquake because the fault is located at only 20 km from the central UB area. Figure 3-2 shows the location of the Emeelt fault, and Table 3-1 shows the parameters of the characterized fault model of the scenario earthquake. The fault location, orientation, and the detailed fault parameters proposed in the previous study (Oyun-Erdene et al., 2014) are used in the simulation. Figure 3-2 shows the Emeelt fault characterized variation model, estimated as the severest scenario. The expected moment magnitude (Mw) is 7.4, and one asperity, also known as strong motion generation area (Irikura & Miyake, 2011), is assumed in the earthquake. The path and site properties used in the SGFM are also listed in Table 3-1.

3. 4. Strong ground motion prediction on seismic bedrock

The strong ground motions are simulated at 50 sites where the shear-wave velocity models were obtained in our previous study (Tumurbaatar et al., 2019). The upper figures of Figure 3-3 show the time histories of acceleration waveforms on the seismic bedrock estimated by the SGFM at the site A-C in Figure 3-2. Since we assume a constant radiation pattern, only one horizontal component of the seismic wave is estimated at each target site.

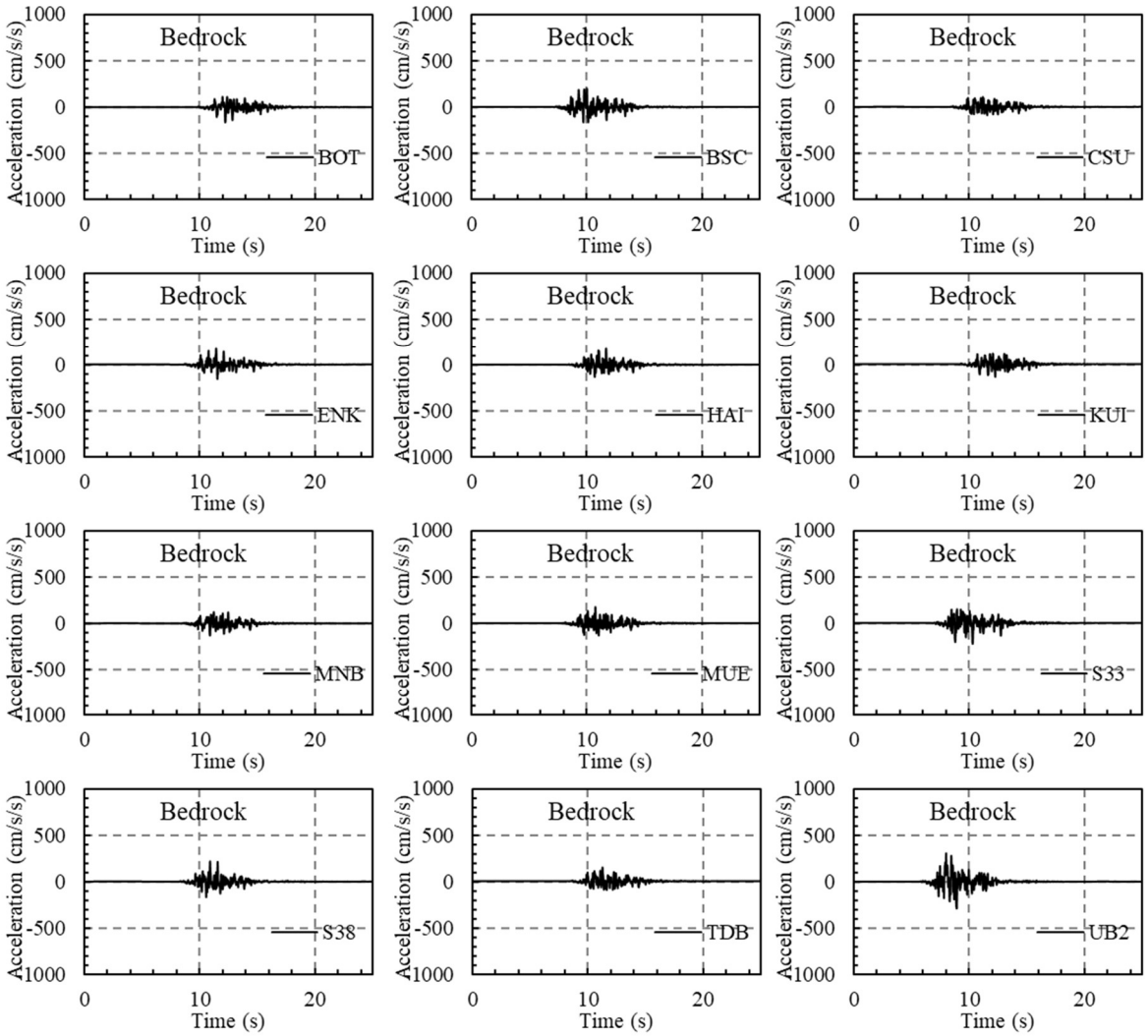

Figure 3-4. Acceleration time histories at seismic bedrock by SGFM at all sites.

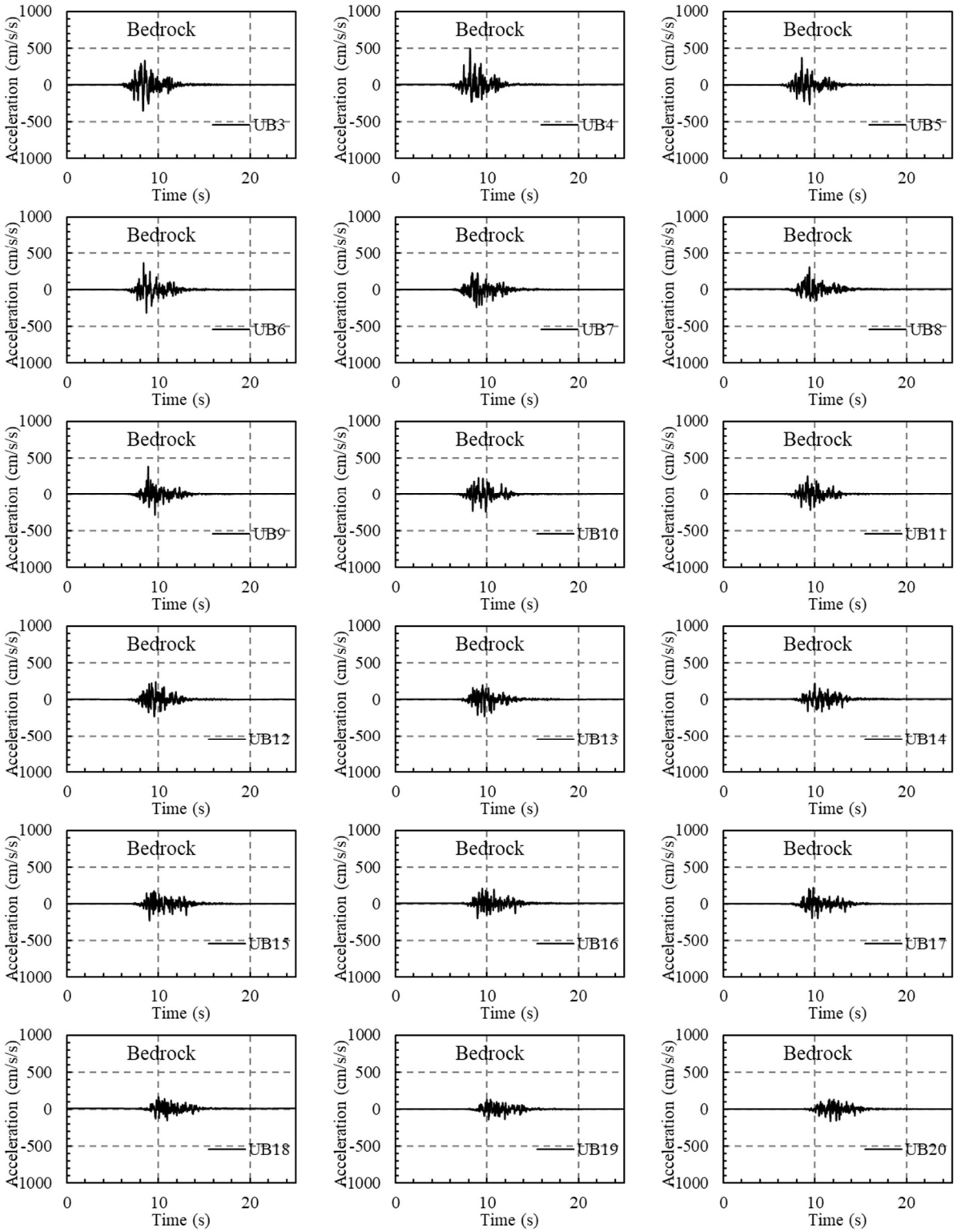

Figure 3-5. Acceleration time histories at seismic bedrock by SGFM at all sites.

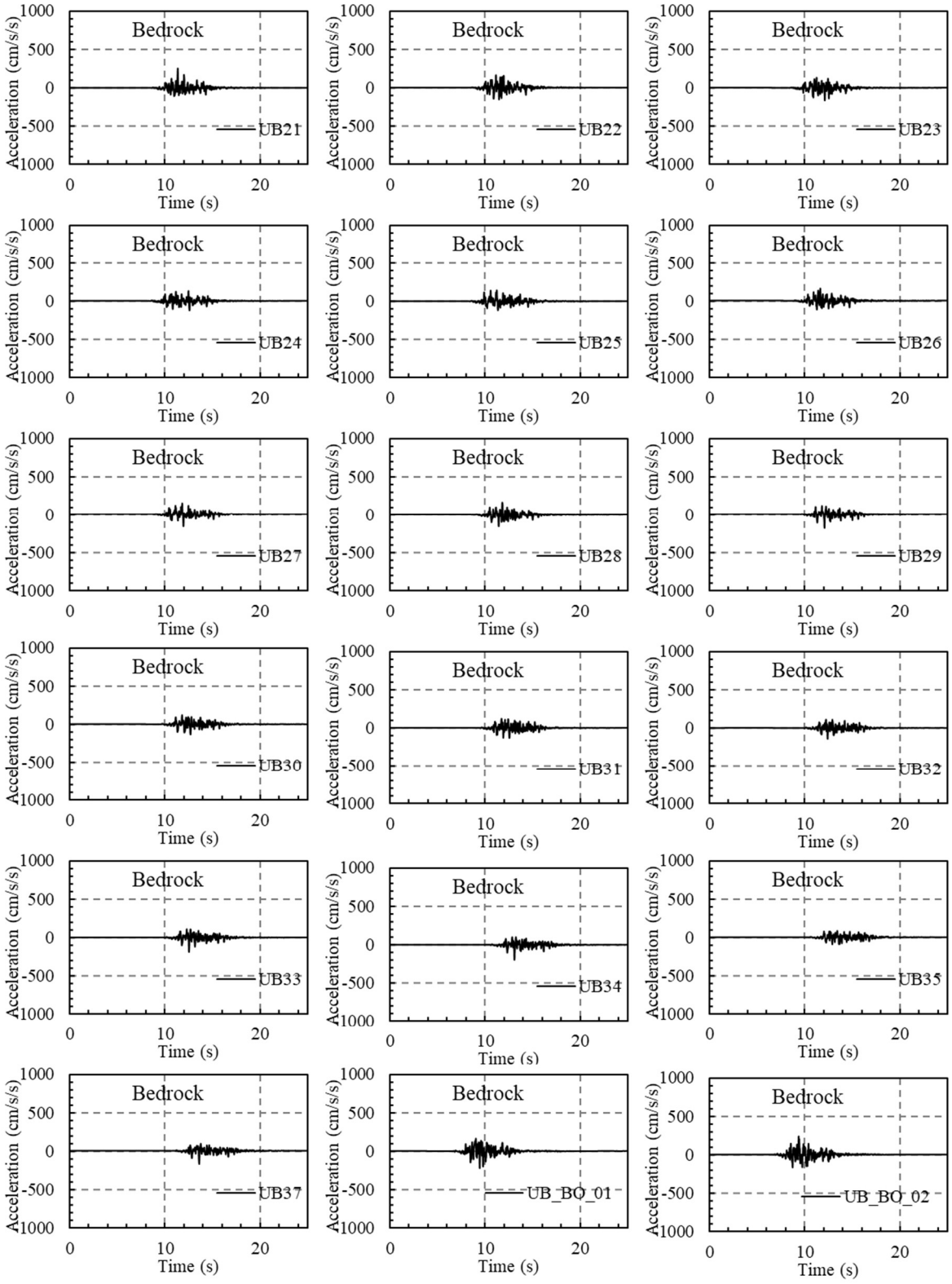

Figure 3-6**.** Acceleration time histories at seismic bedrock by SGFM at all sites.

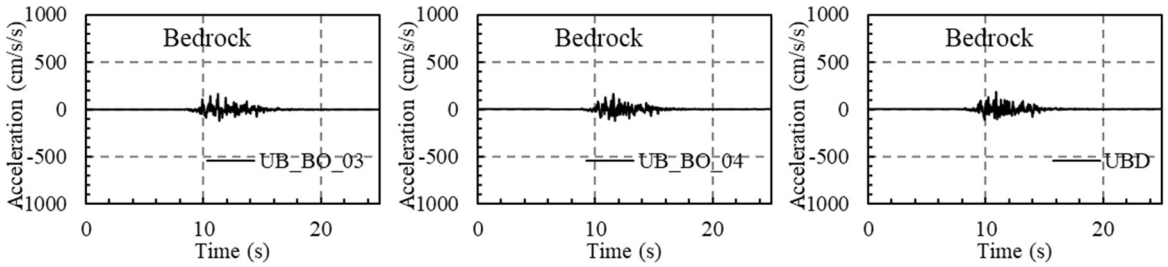

Figure 3-7. Acceleration time histories at seismic bedrock by SGFM at all sites.

3. 5. Ground response analysis

3. 5. 1. Equivalent linear ground response analysis

In order to evaluate the nonlinear seismic ground response, the equivalent linear response analysis of DYNEQ (Yoshida et al., 2002) is applied in this study. DYNEQ is an open-source program that considers the strain-dependent soil properties (shear modulus and damping factor) of horizontally layered media during strong shaking. DYNEQ can also consider the frequency-dependent dynamic soil properties to suppress the underestimation of short-period surface ground motions that were sometimes found in applying the SHAKE (Schnabel et al., 1972). The shear-wave velocity models estimated in our previous study (Tumurbaatar et al., 2019) are used in the simulation. I assume all the soil layers in the UB area as sand and gravel and apply the soil properties introduced in Ref. (Koyamada et al., 2003; Yoshida, 2015).

Figure 3-4 to 3-7 shows the estimated surface ground motions and acceleration response spectra at all sites. The peak ground acceleration (PGA) at a site closer to the earthquake fault is approximately 700 cm/s2. The PGAs at central and eastern UB sites are about 500 cm/s2, respectively. A significant peak is found at 0.6 s in the response spectrum at a closer site. Multiple peaks are found at 0.25 s and 0.7 s in central and eastern sites.

To accurately assess the vulnerability for building-by-building, strong motion at each building site needs to be estimated. However, it is challenging to estimate ground motions at arbitrary sites because of the limitation of the available sites where the shear-wave velocity model is obtained. Therefore, the spatial interpolation technique is applied to estimate the distribution of response accelerations. The inverse distance weighted interpolation (IDW) is used in this study.

3. 5. 2. Dynamic soil properties (sand and gravel)

It is essential to estimate the seismic behavior of the surface soil layer to calculate input earthquake motion to the building because the surface layer amplifies earthquake motion. Equivalent linear site response analysis DYNEQ (Yoshida et al., 2002) is applied to obtain the surface ground motion time histories. Shear modulus (G) and damping (h) are necessary as the mechanical properties in the equivalent linear method. Figure 3-8 shows the dynamic properties of soil used to calculate in the DYNEQ. Strain-stiffness of ground (G/G0) and strain-damping (h-γ) for soil type sand, gravel, and bedrock were applied in this method (Imazu and Fukutake, 1986).

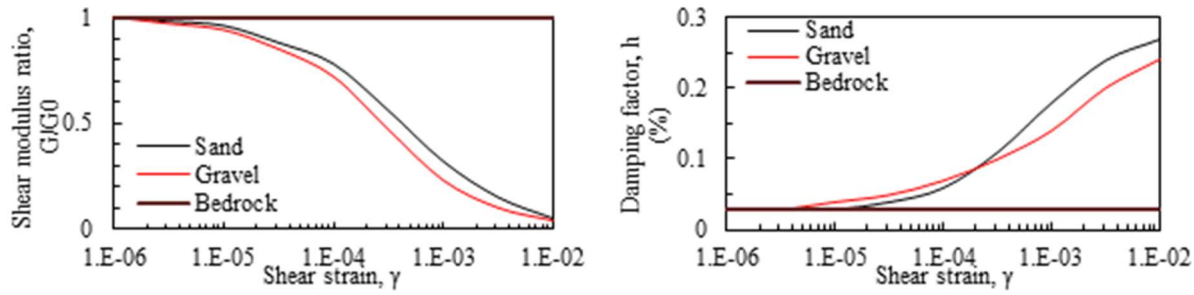

Figure 3-8. Dynamic soil properties of DYNEQ

3. 5. 3. Results

Figure 3-9 to Figure 3-11 also shows acceleration time histories at a surface of sites obtained by the SGFM and the equivalent linear site response analysis. The estimated peak ground acceleration (PGA) on the ground surface at the site A reached 500 cm/s/s since the site is located in the western part of UB near the seismic fault.

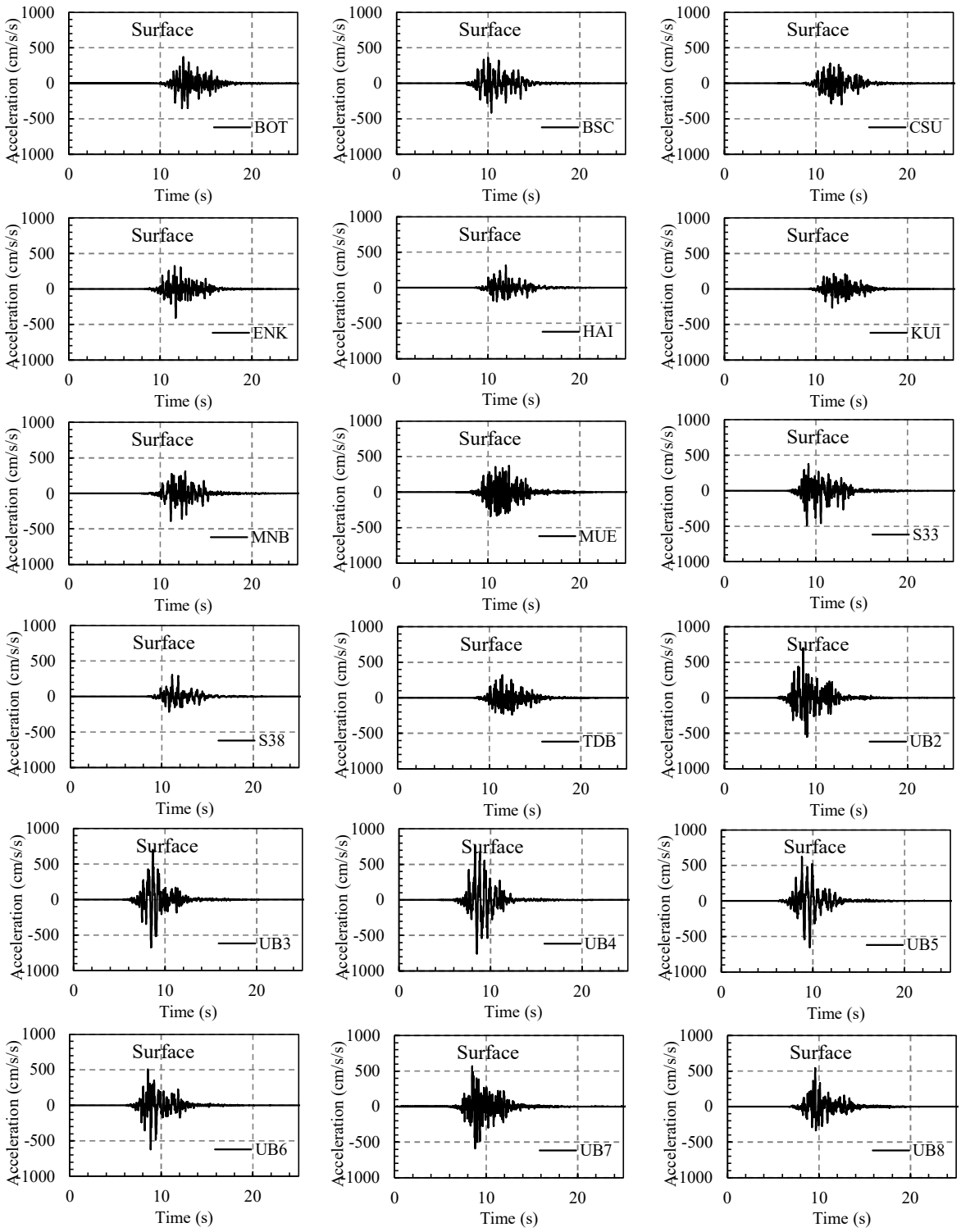

Figure 3-9**.** Acceleration time histories ground surface, estimated by SGFM and equivalent linear seismic response analysis of DYNEQ at all sites.

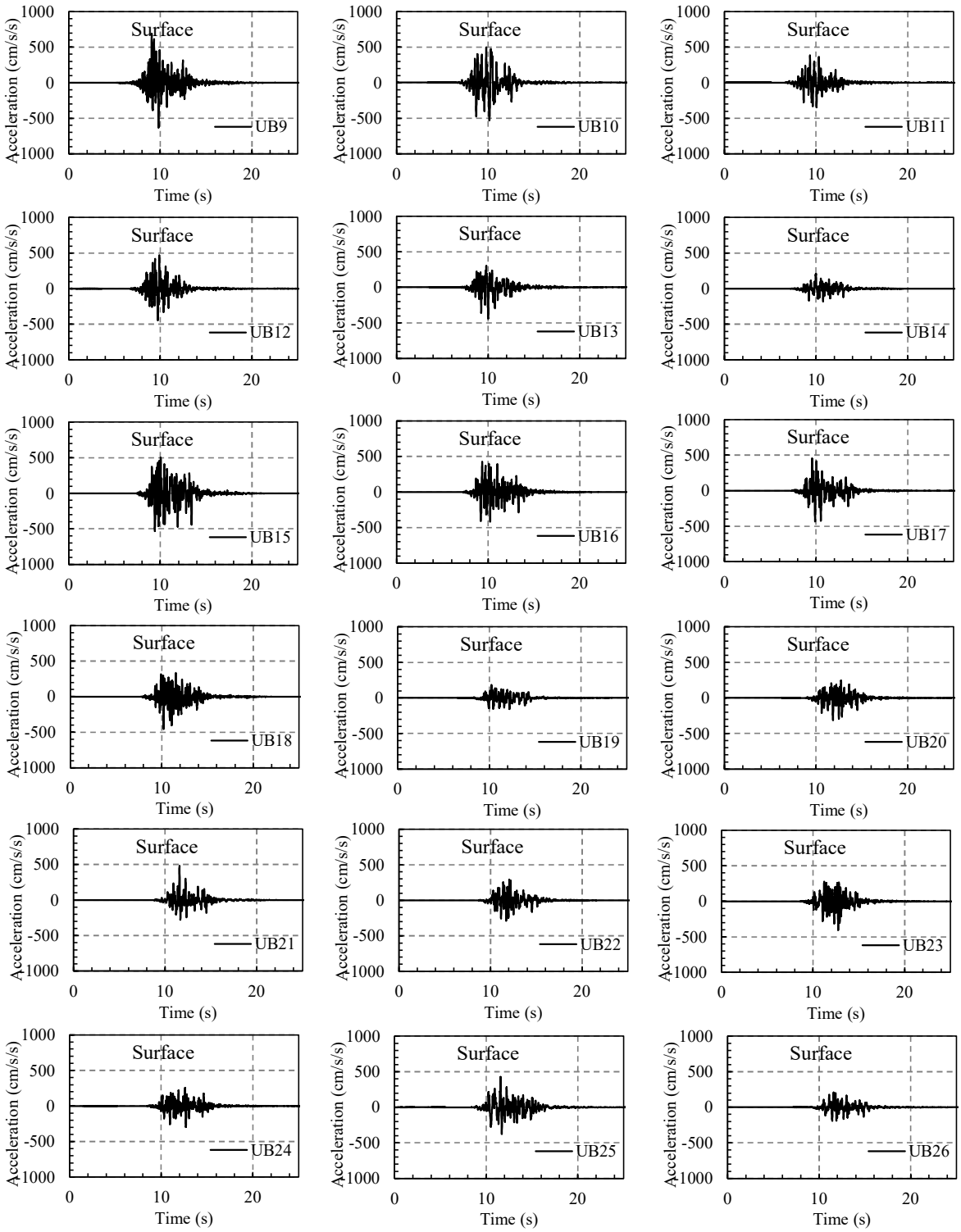

Figure 3-10**.** Acceleration time histories ground surface, estimated by SGFM and equivalent linear seismic response analysis of DYNEQ at all sites.

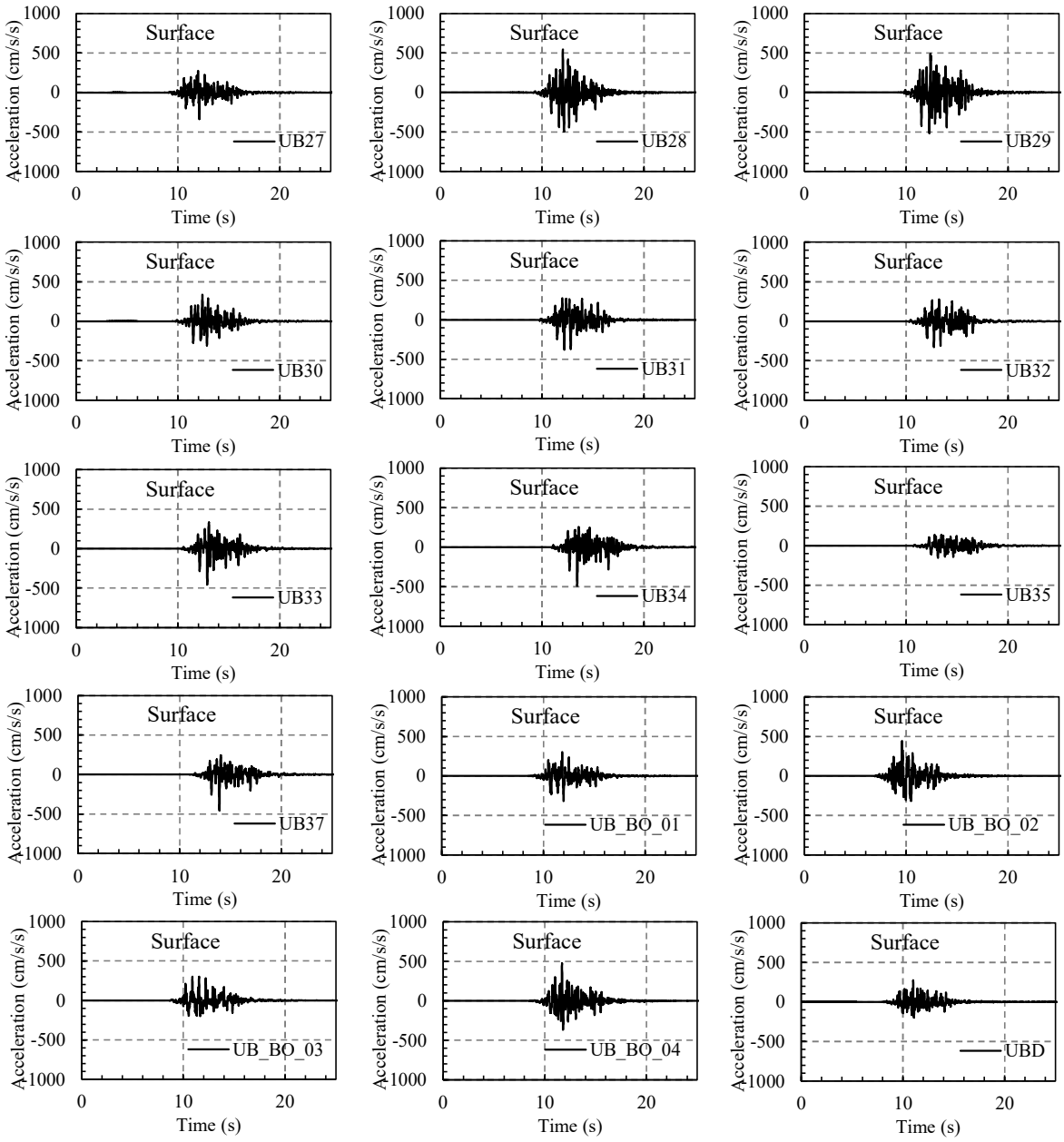

Figure 3-11. Acceleration time histories ground surface, estimated by SGFM and equivalent linear seismic response analysis of DYNEQ at all sites.

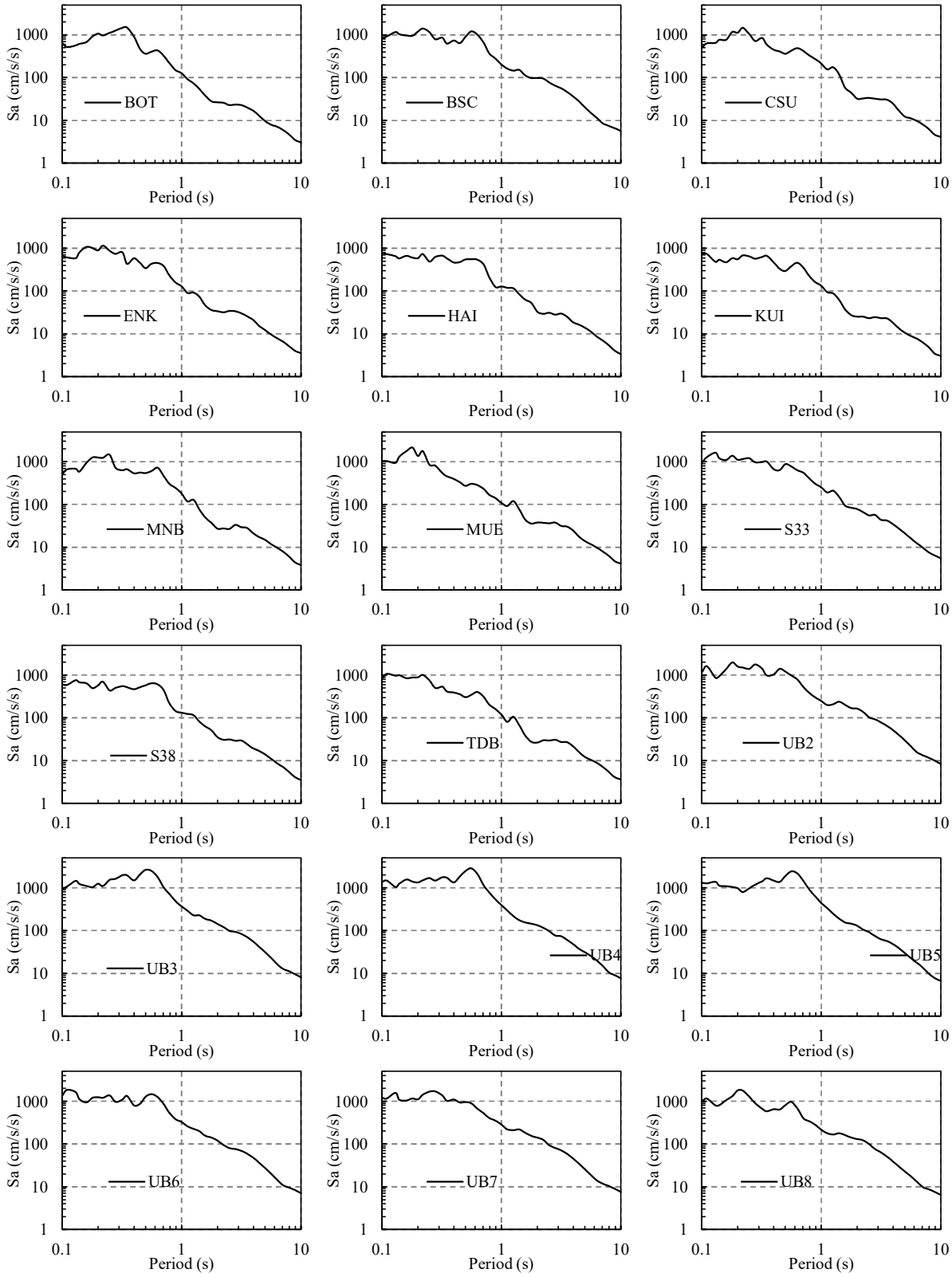

Figure 3-12. Response spectra estimated by SGFM and equivalent linear seismic response analysis of DYNEQ at all sites.

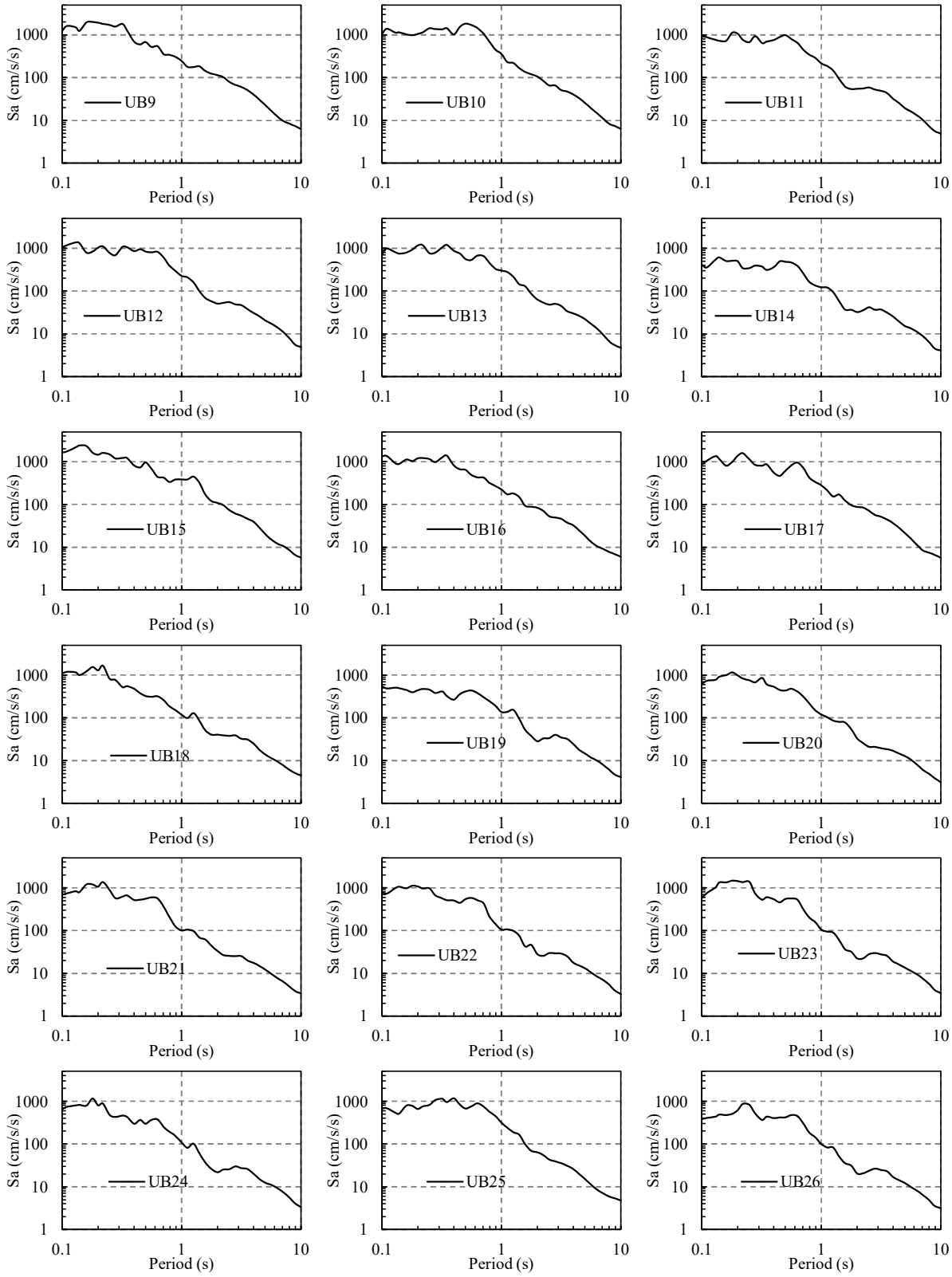

Figure 3-13. Response spectra estimated by SGFM and equivalent linear seismic response analysis of DYNEQ at all sites.

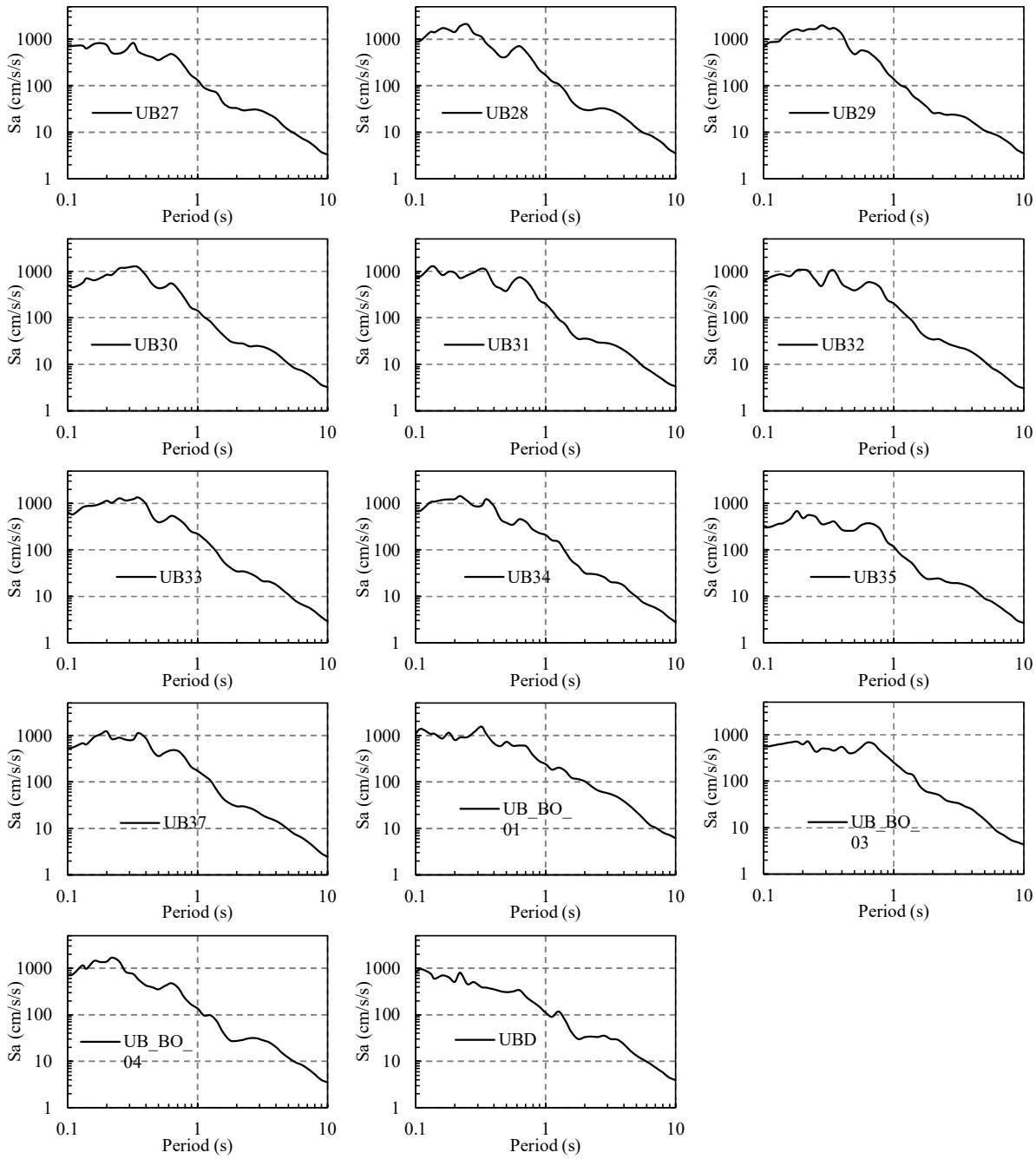

Figure 3-14. Response spectra estimated by SGFM and equivalent linear seismic response analysis of DYNEQ at all sites.

3. 5. 4. Response spectra

Figure 3-12 to Figure 3-14 also show the spectral acceleration ratios at all the sites. The predominant period at closer site is 0.6 s, whereas the predominant period at site central and eastern is 0.2 to 0.3 s. The spectral acceleration at the peak periods is larger than 1000 cm/s/s.

3. 6. Distribution of seismic intensities in UB

3. 6. 1. Spatial interpolation

Inverse distance weighting (IDW) is a type of deterministic method for multivariate interpolation with a known scattered set of points. The assigned values to unknown points are calculated with a weighted average of the values available at the known points.

The name given to this type of method was motivated by the weighted average applied, since it resorts to the inverse of the distance to each known point ("amount of proximity") when assigning weights.

The expected result is a discrete assignment of the unknown function$u$ in a study region:

$$u(x): x \to \mathbb{R},\ x \in D \subset \mathbb{R}^n,$$

where *D* is the study region.

The set of known data points can be described as a list of tuples:

$$[(x_1, u_1), (x_2, u_2), \dots, (x_N, u_N)].$$

The function is to be "smooth" (continuous and once differentiable), to be exact ($u(x_i) = u_i$) and to meet the user's intuitive expectations about the phenomenon under investigation. Furthermore, the function should be suitable for a computer application at a reasonable cost (nowadays, a basic implementation will probably make use of parallel resources).

A general form of finding an interpolated value u at a given point x based on samples $u_i = u(x_i)$ for $i = 1,2, \dots, N$ using IDW is an interpolating function (III-9):

$$u(x) = \begin{cases} \dfrac{\sum_{i=1}^{N} w_i(x) u_i}{\sum_{i=1}^{N} w_i(x)}, & if\ d(x, x_i) \neq 0\ \ for\ all\ i, \\ u_i, & if\ d(x, x_i) = 0\ \ for\ some\ i, \end{cases} \tag{3-9}$$

where,

$$w_i(x) = \frac{1}{d(x, x_i)^p} \tag{3-10}$$

Equation 3-10 is a simple IDW weighting function, as defined by Shepard, x denotes an interpolated (arbitrary) point, x_i is an interpolating (known) point, d a given distance (metric operator) from the known point x_i to the unknown point x, N is the total number of known points used in interpolation and p is a positive real number, called the power parameter.

3. 6. 2. Results

Here are the spectral acceleration results of UB based IDW method. According to the result, there is higher acceleration distributed near the fault area also eastern sides of UB related to soft deposit along the Tuul river. Figure 3-15 shows the distribution of the response accelerations in UB for the typical periods (0.35 s, 0.40 s, 0.50 s, 0.56 s, 1.09 s and 2.24 s). Larger accelerations are estimated in the western area because of the closer distance to the earthquake fault. On the other hand, large accelerations at 0.35 s and 0.40 s are also estimated in the eastern area, although the area is farther than the central area to the fault. According to our site effect assessment (Tumurbaatar et al., 2019), strong amplifications in short periods were expected in the eastern area, probably due to the soft deposits along the river.

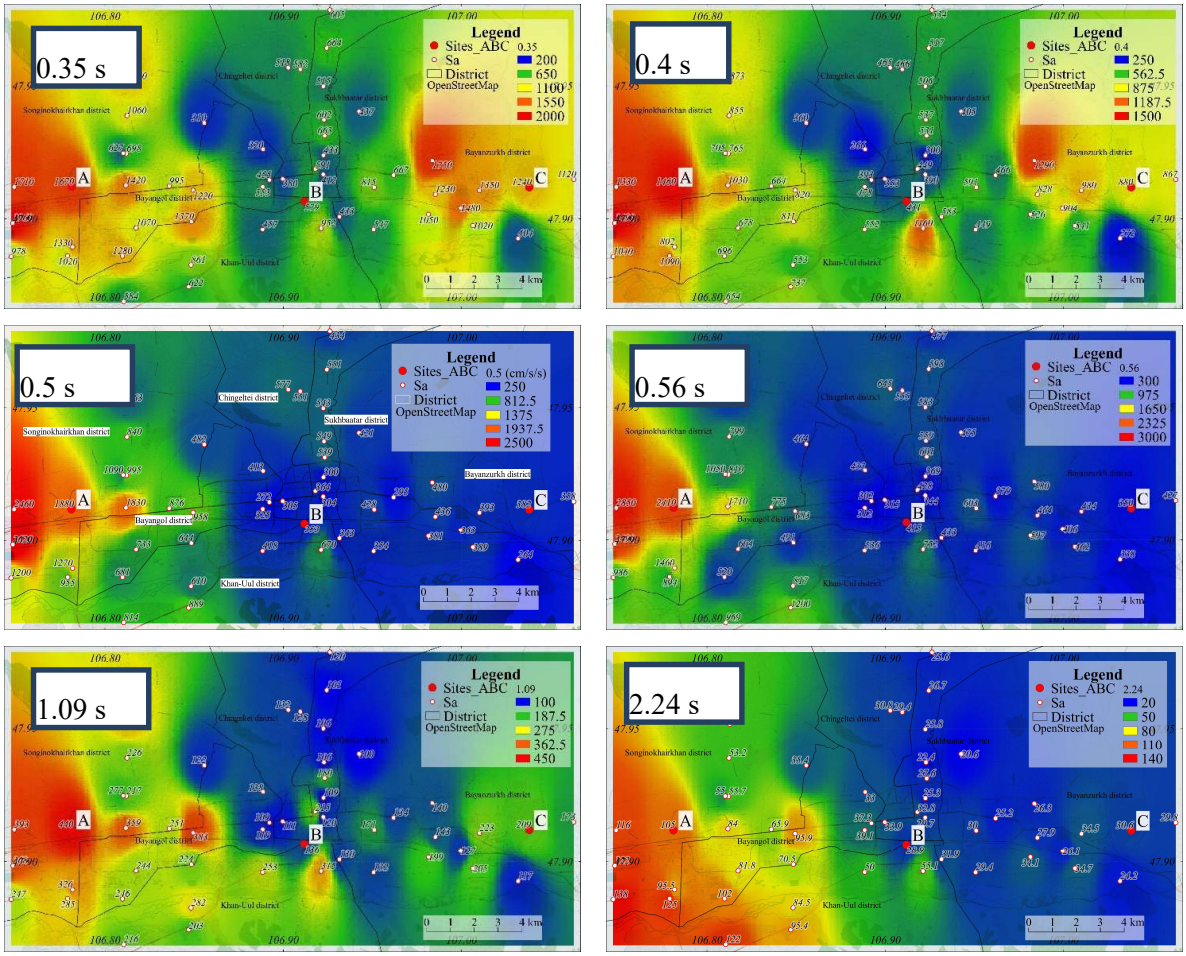

Figure 3-15**.** Distributions of spectral accelerations in UB at 0.35 s, 0.40 s, 0.5 s, 0.56 s, 1.09 s and 2.24 s were estimated from the Mw7 Emeelt earthquake.

3. 7. Conclusion

In this chapter, strong ground motion simulation is performed for the scenario earthquake induced by the Emeelt fault. Seismic ground motions at the seismic bedrock are computed by the stochastic Green's function (SGF) method and the characterized fault model. Seismic ground motions at the ground surface are calculated by the estimated shear-wave velocity models in the Chapter 2 and equivalent linear seismic response analysis method of DYNEQ. The dynamic soil properties for sand and gravel developed in Japan are applied to evaluate nonlinear response of strong shaking. The distributions of spectral accelerations for typical periods are estimated from the strong ground motion simulation and spatial interpolation technique. The result of the simulation shows that the peak ground acceleration is expected at approximately 500 cm/s/s in the western part of UB located near the fault.

The inverse distance weighted interpolation (IDW) is used for distribution of spectral acceleration in predominant periods. The spectral accelerations at 0.35 s, 0.4 s and 0.5 s periods are up to 2500 cm/s/s near the fault area. On the other hand, large accelerations at 0.35 s and 0.40 s are also estimated in the eastern area, although the area is farther than the central area to the fault

CHAPTER 4. DEVELOPMENT OF BUILDING INVENTORY IN ULAANBAATAR

4. 1. Introduction

Building inventory development is one of the important parts of disaster risk assessment such as hurricane, flood, and earthquake. Regional and national level evaluation requires low-resolution distribution of buildings on the district or regional scale. A high-resolution database is essential for detailed seismic assessment, but it is time-consuming and costly (Polese, M, 2019).

For a general building stock, the following parameters affect the damage and loss characteristics: structural system; material and lateral-load-resisting system; height: number of floors; and construction year: for the identification of seismic design level. Also, land use information is very important for disaster risk analysis in urban areas. There is no single reliable source, which can be used for developing a unique database for building and infrastructures located in an urban area.

In this chapter, I will describe the existing building inventory and which factors are required to estimate building damage assessment especially in UB.

4. 2. Existing building inventory data

The Geographical Information System (GIS) -based building inventory database in UB was firstly established by the Korea International Cooperation Agency (KOICA) in 2010. The database has been updated by the UB city office and was used in the seismic risk assessment by JICA (City & Japan International Cooperation Agency, 2013). The inventory data includes more than 32,000 buildings with location information, a number of stories, main structural type, building area, and construction year, as shown in Table 4-1.

Figure 4-2 (a) and (b) show the distribution of the construction year and building heights of the existing building inventory in UB, respectively. Figure 4-2 (a) also illustrates the areas of the urban sprawl in UB (UN Habitat, 2016). Figure 4-2 (b) also illustrates urban land use such as residential, office, and industrial areas (*Ulaanbaatar 2020 Master Plan and Development Approaches for 2030*, 2014). Ger is a traditional Mongolian dwelling that consists of a round felt tent covered with durable, waterproof, and white canvas. Since many ger houses exist outside the land use areas, we added the ger areas in Figure 4-2 (b) by manually delineating the boundaries from the current building distribution. Although ger-type houses have been built mainly in the ger areas around mountainous areas, ger houses have not been registered in the inventory data. Therefore, ger houses are not considered in this study. Low-rise (1-3 story) buildings typically dominate in the ger areas, and mid-rise and high-rise buildings are highly concentrated in the central office and residential areas. Figure 4-4 (a) and (b) represent the close-ups of the central part of UB shown by the rectangular in Figure 4-2 (a) and (b), respectively. Building information was assigned for an individual building in the GIS inventory data.

Table 4-1. List of building information of the existing inventory data.

1	Object ID	2	District	3	Khoroo (Sub-district)
4	Zipcode	5	Location	6	Curriculum (Building use)
7	Capacity	8	Number of stories	9	Construction year
10	Main structural type	11	Area of shape	12	Total floor area

Table 4-2 shows the number of buildings in the inventory data according to structural types and building heights. Totally 32,500 buildings are included in the inventory data. Approximately 85 % of the buildings are low-rise buildings. The number of high-rise buildings higher than 16 stories is about 300. The structural types are masonry, timber, reinforced concrete (RC) frame, RC frame with a masonry wall, RC frame with a shear wall, precast, and steel structures. However, the structural types for more than 50 % of the buildings are not registered (unknown). Besides, the masonry and timber buildings seem erroneous. For example, many masonries and timber buildings are higher than four stories despite most of those building types being low-rise. In the first recording of the inventory, the misclassifications would be generated. If some part of the roof and/or exterior walls in nonstructural elements of the building were wood or brick, the main bearing structures were incorrectly listed as wooden or brick.

Table 4-3 shows the number of buildings with construction years. Similar to the structural types, construction years for more than 60 % of the buildings are unknown. Most of the unknown buildings can be classified as buildings constructed before 2010 because the building officials have rarely registered the older buildings. In contrast, most of the newly constructed buildings after 2010 have been almost fully registered in the inventory.

The heating system of each building is essential information for estimating construction costs in UB described later. However, such information is not included in the inventory. The existing building inventory data issues for estimating construction cost can be summarized as follows. First, structural types of unknown, masonry, and timber buildings need to be estimated. Second, the construction years for unknown buildings need to be estimated, and last, the heating system of each building needs to be estimated.

Table 4-2**.** The number of buildings with structural type and number of stories in existing inventory data.

Main structural type	1-3 story	4-7 story	8-15 story	16-up story	Total	Percent
Unknown	17,673	195	15	0	17,883	54.94
Masonry	1,363	497	24	3	1,887	5.79
Timber	6,571	688	161	24	7,444	22.86
Reinforced concrete (RC)	814	788	1117	205	2,924	8.97
RC with masonry wall	165	121	3	0	289	0.88
RC with shear wall	40	30	51	37	158	0.48
Precast	561	581	494	37	1,673	5.13
Steel	267	17	8	0	292	0.89
Total	27,454	2,917	1,873	306	32,550	100

(**a**)

(**b**)

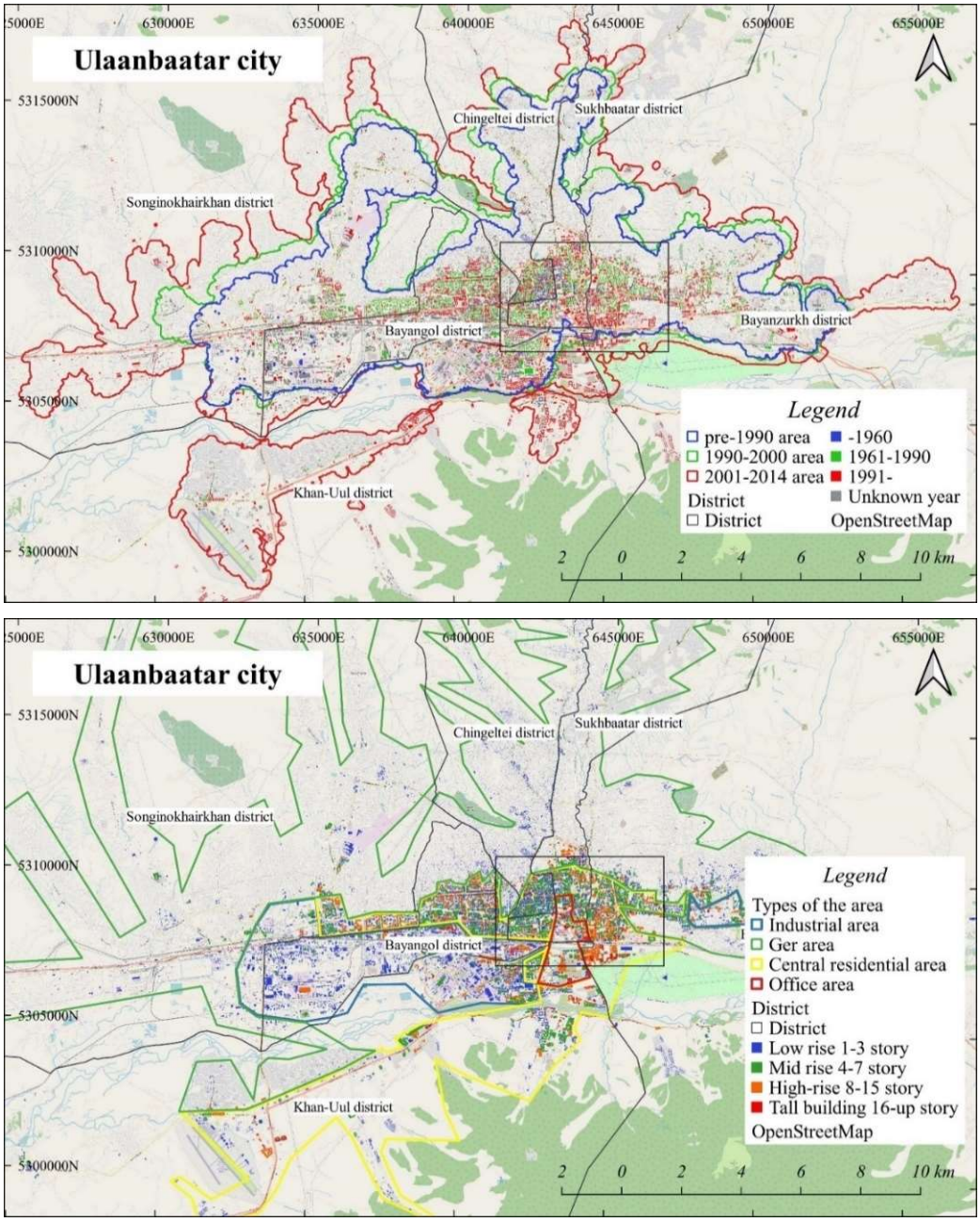

Figure 4-1**.** (**a**) Construction year distribution in Ulaanbaatar city with urban expansion (UN Habitat, 2016); (**b**) Distribution of building heights with urban land use.

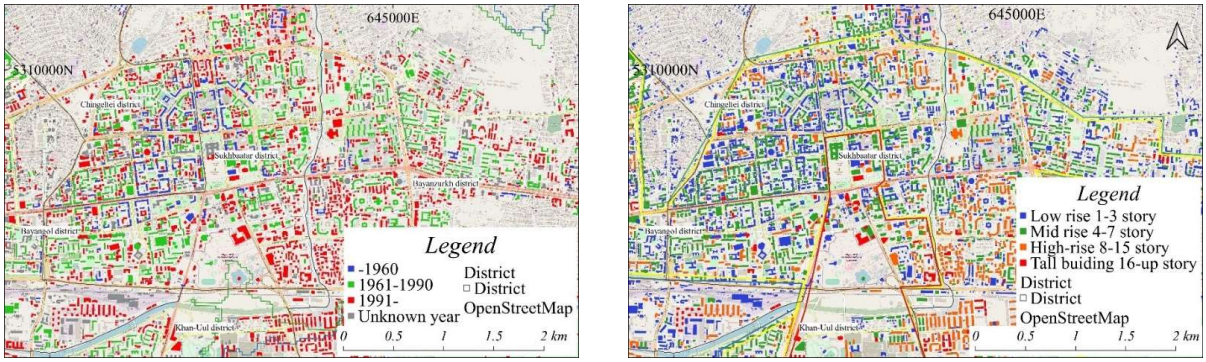

(**a**) (**b**)

Figure 4-2**.** (**a**) Construction year distribution in Ulaanbaatar; (**b**) Distribution of building heights.

Table 4-3**.** The number of buildings with construction year and a number of stories in existing inventory data.

Construction year	1-3 story	4-7 story	8-15 story	16-up story	Total	Percent
Unknown	20,121	404	34	12	20,640	63.4
-1960	350	56	0	0	406	1.25
1961-1990	1,322	536	234	1	2,099	6.45
1991-	5,579	1,922	1,605	293	9,405	28.9
Total	27,386	2,918	1,873	306	32,550	100

4. 3. Development of inventory data

4. 3. 1. Heating type

Since it is difficult to find information about the heating system coverage map, the coefficient $K_{\_heating}$ is estimated from the existing GIS data by defining the heating system connected area of UB. In general, residential apartments are connected to the central heating system in the central regions of UB, shows in Figure 4-3. Most households located around mountain areas such as ger areas are not connected to the central city system. Simple heating stoves and individual heating types are typically used for small houses and industrial buildings, respectively. Table 4-4 shows the criteria for the estimation of a heating type for each building. The heating type is determined by the building location, structural type, and building area. Small and low-rise buildings in ger area are classified to the simple heating stove. Two-story buildings whose building use and structural type are both unknown, and two-story small masonry or timber buildings are also assigned to the simple heating stove. Buildings in ger area whose building use or structural type is already given in the inventory are classified to the individual heating type. Outside ger area, 1-2 story small precast or steel buildings are also classified to the individual heating type. Other buildings outside ger areas are classified to the central heating system. The smaller coefficient is given to the buildings with a simple heating stove, and a higher coefficient is given to the buildings with the central heating system, as shown in Eq. (4-1).

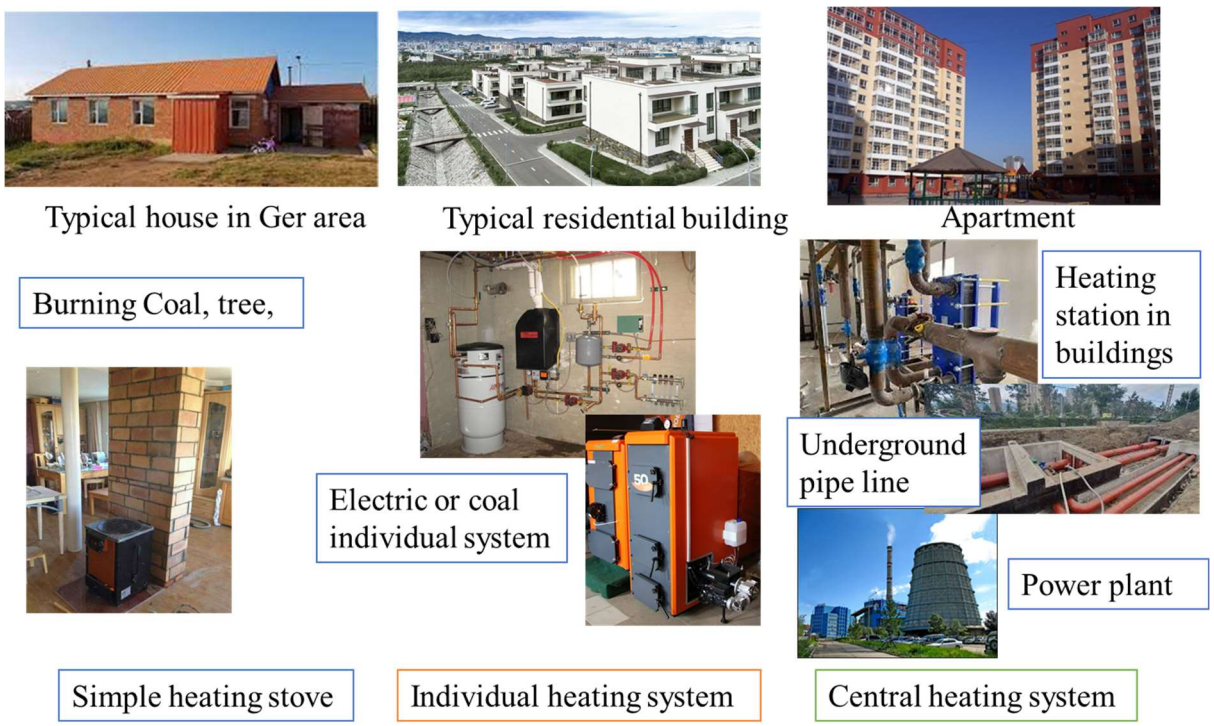

Figure 4-3. Photos of heating system type of Ulaanbaatar city.

Table 4-4. Table of defining the heating type of building.

Location	Number of stories	Area, A (m^2)	Building use	Structural type	Assigned heating system type
In ger area	1	A<80	-	-	Simple heating stove
	2	All	Unknown	Unknown	
		A<200	Not public[1]	Masonry or timber	
		Others			Individual heating type
	≧3	-	-	-	
Outside ger area	1-2	A<200	Not public*	Precast or steel	
	Others				Central heating system

[1] Not public buildings correspond to residential, commercial, or industrial buildings.
Hyphen "-" indicates no criteria for the building information.

4. 3. 2. Structural type

Building structural type is important information to estimate construction cost and assign vulnerability functions for seismic loss estimation. The location, number of stories, building area, and shape of the building classify the structural types of the unknown buildings. Table IV-5 shows the criteria for the estimation of structural types for the unclassified buildings. The unknown buildings are classified as masonry, timber, precast, steel, and RC with masonry wall structures. The building area and the width and length of buildings are considered in the classification because the shape of the building would be a key parameter to assign the structural type. The width and length are approximated from the area and perimeter of a building polygon. The threshold values in the criteria are determined from the characteristics of the known buildings in the existing inventory.

The small and low-rise buildings are classified into masonry or timber structures. On the contrary, larger and higher buildings are classified as precast, steel, or RC with masonry wall structures. If the buildings are located in the industrial area, the buildings are classified as precast or steel frames. As described before, some misclassifications are found in the classified buildings. According to the Mongolian seismic code, the load-bearing structure of a building with more than five floors cannot be made of bricks, but there is an error in these data as there are tall brick buildings. Therefore, tall masonry buildings are re-classified to RC with masonry or RC with shear wall depending on the number of floors. The high-rise timber and RC buildings are re-classified to RC with masonry walls or RC with a shear wall, and large timber buildings in industrial areas are steel structures. The threshold values in the criteria are empirically from the characteristics of the registered buildings in the inventory.

Table 4-5. Criteria for defining the structural type of building.

Original structural type	Number of stories	Location	Area, A (m^2)	Width, W (m)	Length, L (m)	Assigned structural type
Unknown	1	In ger area	-	W<6	L<8	Timber
		In industrial area	-	14≦W<30	-	Precast
		In industrial area	A≧2000	-	-	Steel
		In industrial area	-	W≧30	-	Steel
		Outside industrial area and ger area	-	W≧10	-	RC with masonry wall
		Others				Masonry
Unknown	2	In ger area	A<80	W<8	-	Timber
		In industrial area	-	14≦W<30	-	Precast
		In industrial area	A≧2000	-	-	Steel
		In industrial area	-	W≧30	-	Steel
		Outside industrial and ger area	-	W≧12	-	RC with masonry wall
		Others				Masonry
Unknown	3	In ger area	-	W<6	L<8	Timber
		In ger area	-	W>14	-	Masonry
		In industrial area	-	W≧14	L>24	Precast
		Outside industrial and ger area	-	W>12	-	RC with masonry wall
		Others				Masonry
Unknown	4-5	In industrial area	-	10≦W<16	L≧72	Masonry
		In industrial area	-	W≧16	-	Precast
		Outside industrial	-	W≦16	-	Masonry
		Others				RC with masonry wall
Unknown	≧6	-	-	-	-	RC
Timber	1-2	In industrial area	-	W≧12	-	Precast
	1-2	Outside industrial area and ger area	-	W≧12	-	Masonry
	1-2	-	-	-	-	Timber
	3-4	-	-	-	-	Masonry
	≧5	-	-	-	-	RC
Masonry	1-5	-	-	-	-	Masonry
	6-8	-	-	-	-	RC with masonry wall
	≧9	-	-	-	-	RC with shear wall
RC	1-7	-	-	-	-	RC
	≧8	-	-	-	-	RC with shear wall

Hyphen "-" in the cell indicates no criteria for the building information.

4. 3. 3. Construction year

Since it is difficult to accurately estimate construction year only from the existing inventory data for an individual building, the urban sprawl map shown in Figure 4-2 (a) is used in the estimation. Table 6 shows the criteria for the estimation of the construction year. As previously described, most of the unknown buildings are supposed to be constructed before 2010. The parameters used in the criteria are location, number of stories, building area, and structural type. Most timber and precast buildings were constructed before and during the period of the influence of the Soviet Union. If the structural type of the target building is timber or precast, the construction year is classified as an older building constructed before 1990. Large steel or masonry buildings are also classified as an older buildings before 1990. If the number of stories is higher than 12, the construction is classified as a newer building constructed after 2001. Other buildings are classified as structures built from 1991 to 2000.

Table 4-6. Criteria for defining construction year.

Location (in UN-Habitat urban sprawl map)	Number of stories	Area, A (m^2)	Structural type	Assigned construction year
Pre - 1990	All	All	Timber or precast	Before 1990
	≧12	All	All	2001-2010
	1-11	Others		1991-2000
In 1990-2000 area	All	All	Timber or precast	Before 1990
	All	A≧1000	Steel or masonry	Before 1990
	≧12	All	All	2001-2010
	Others			1991-2000
Outside 1990-2000 area	All	All	Timber or precast	Before 1990
	Others			2001-2010

4. 3. 4. Validation

The estimated structural types are validated by comparing them with the field photographs. Figure 4-4 compares the structural types estimated by the proposed method and the pictures of typical buildings in the StreetView of Google Maps (Google map, n.d.). The upper three buildings in Figure

4-4 were classified as unknown in the existing inventory data and are classified to masonry, precast, and RC with a masonry wall, respectively. Whereas the original structural type of the building shown at the bottom of Figure 4-4 was timber, the type is obviously erroneous by comparing it to the field photo. The building is re-classified to RC by the proposed criteria.

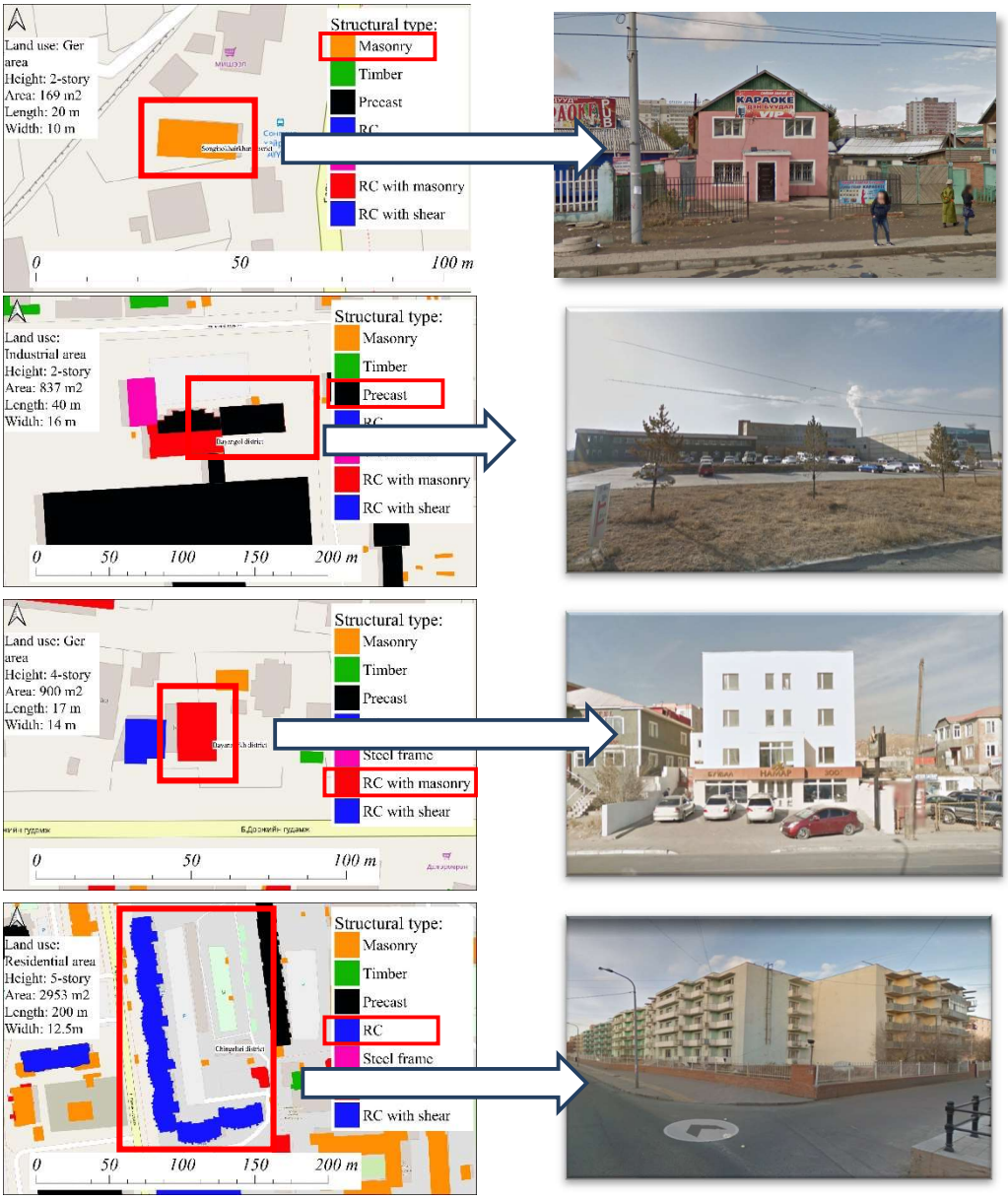

(**a**) (**b**)

Figure 4-4**.** Comparisons of estimated structural types and ground photos (**a**) Estimated inventory data; (**b**) Ground photos in Google Street View (Google map, n.d.).

4. 4. Cost estimation

The building costs of the buildings in UB are estimated using the Mongolian construction code (Ministry of Construction and Urban Development in Mongolia, 2016). Ministry of construction and urban development in Mongolia published the latest code in 2016 suitable for this research data. This rule shall apply to the implementation of Article 33.1.10 of the "Law on Construction" and to regulate relations related to the use of the standard unit capacity assessment approved by the Order No. 203 of the Minister of Construction and Urban Development in 2016. Preliminary design estimates of unit capacity of buildings and structures at the pre-design stage to determine the budgeted cost of buildings and engineering networks, to develop investment programs, to make economic calculations, research and analysis, to compare cost estimates, to study socio-economic. It is used to estimate and research programs, to plan investments in advance, and to guide designers in making optimal decisions. It will also be used to provide investors, customers and contractors with the same conditions and information to determine the cost of construction. Standard unit capacity estimates can be used as a basis for estimating asset valuations, as well as reference estimates for cost estimates, financial statements, and tax purposes. Standard unit capacity assessments shall not be used for financing. In calculating the unit capacity of the building, the estimated cost of the building was calculated based on the selected construction, probability, and working drawings, and the average budgeted cost per unit area was calculated based on the total construction area along the working drawing axis.

The calculation, which defines the benchmark unit capacity, does not include the cost of land acquisition for the construction of the facility, the cost of relocating the utilities and the cost of the plant's construction technology equipment, as well as the cost of the land and sales. Standard unit valuation estimates do not include the cost of external utilities and the construction of auxiliary buildings, substations, boreholes and boilers, so they will be assessed separately.

The total cost depends on the individual building area and other coefficients of local conditions, such as building heating system, location, structural type, and inflation rate, as shown in

Eq. (4-1).

$$cost_{(MNT)} = cost_{(MNT/m2)} * area_{(m2)} * K_{nature\ (GIS)} * K_{distance\ (GIS)} * K_{heating} * K_{economy} * K_{reduction} \quad (4\text{-}1)$$

$cost_{(MNT/m2)}$ – Building unit cost per floor area for building type in MNT (Mongolian Tugriks as of 2016, 1.0 USD = approximately 1550 MNT).

$area_{(m2)}$ - Building floor area in square meter

$K_{\_nature\ (GIS)}$ - Coefficient for natural influence by the soil and weather., I: 1, II: 1.05, III: 1.10, IV: 1.18, V: 1.25 (Ministry of Construction and Urban Development in Mongolia, 2016), 1.0 in UB area.

$K_{\_distance\ (GIS)}$ – Coefficient for transportation fee (Ministry of Construction and Urban Development in Mongolia, 2016), 1.0 in UB area.

$K_{\_heating}$ - Coefficient for heating system in each building. Buildings in the central district are connected to central heating system 1.0, individual heating type 0.95, Simple heating stove 0.75.

$K_{\_economy}$ – Coefficient for economic condition at each year, 1.0 as of 2016.

$K_{\_reduction}$ – Coefficient for reducing area considered with outer wall space, normally 1.0.

Since the target area of this research is the central districts of UB city, all the buildings are located within 50 km from UB, the coefficients $K_{\_distance}$, $K_{\_natural}$, $K_{\_economy}$, $K_{\_reduction}$ are given at 1.0, respectively. Since Mongolia is located in a cold region, the heating system of a building is one of the critical parameters in evaluating construction costs. The building unit cost per floor area is determined according to the structural type introduced later. It means that the structural type and heating system need to be determined for each building in order to estimate the construction cost. Besides, the construction year also need to be estimated to assign the design level of vulnerability functions.

Despite the lack of the building information in the existing inventory data, the building distribution

in UB suggests that typical building types can be characterized by other building information such as the location, building use, building area, number of stories. This study estimates structural types and construction years for the unknown buildings by criteria developed from the building characteristics in the existing building inventory. The details of each estimation are introduced in the following sections.

The construction costs for all the buildings in UB are estimated from Eq. (4-1). Table 4-7 shows the construction cost per unit in USD for each building use and structural type. A higher cost is required for house and office buildings with RC frame structures. On the other hand, lower cost is required for storehouses or cellars with masonry or steel structures. By using the cost per unit, structural type, building use, and floor area, the total amount of construction cost is estimated for each building.

Table 4-7. Construction cost per unit for typical building uses and structural types.

Building use	**Construction cost per unit (USD/m^2)**				
	Structural types of building [1]				
	A	**B**	**C**	**D**	**S**
Public building					
Office building	816.5	692.5	571.3	561.4	
School	597.4	866.0	521.7	643.5	
Kindergarten	765.0	700.9	702.7	757.0	
Dormitory	632.9	699.4	649.8	633.3	
Clinic	675.4	802.8	754.9	664.5	
Apartment					
House	1001.0	1001.	866.0	832.6	
Public apartment	723.0	667.7	595.0	595.0	
Industrial and maintenance	619.7	576.2	501.0	501.0	503.2
Storehouse or cellar	439.0	439.0	351.2	329.3	329.3

[1] A=RC, RC with masonry, RC with shear wall; B=Precast; C=Masonry; D=Timber; S=Steel.

4. 5. Result of cost estimation

Figure 4-5 shows the estimated construction cost distribution of UB. Figure 4-6 shows the histogram of the number of buildings according to the construction costs. Around 13,000 building cost is lower than 25 thousand USD, which correspond to small buildings located in ger area. Approximately 4,000 buildings are from 300 thousand to 1 million USD, and most of them are located in the central residential area. The buildings whose construction cost is higher than 500 million USD correspond to the high-rise buildings located in the city's central office area.

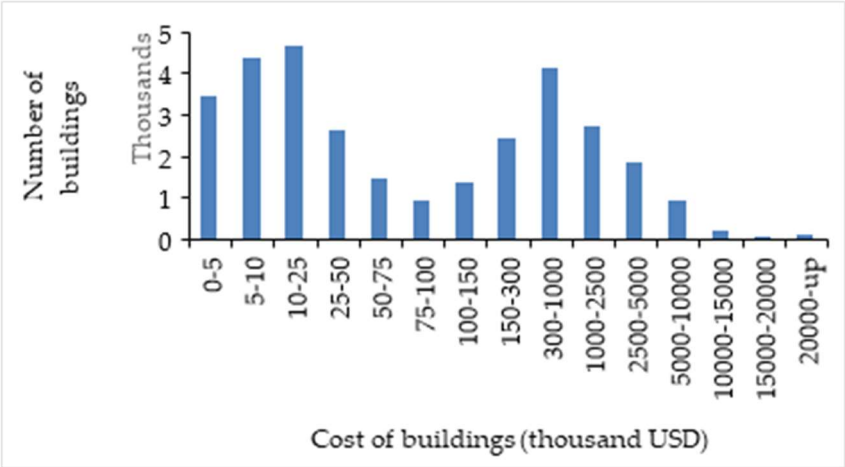

Figure 4-5**.** The number of buildings according to construction cost in thousand USD.

Whereas the estimation is based on the currency as of 2016, I can estimate the current prices considering the change of the currency at a year of interest.

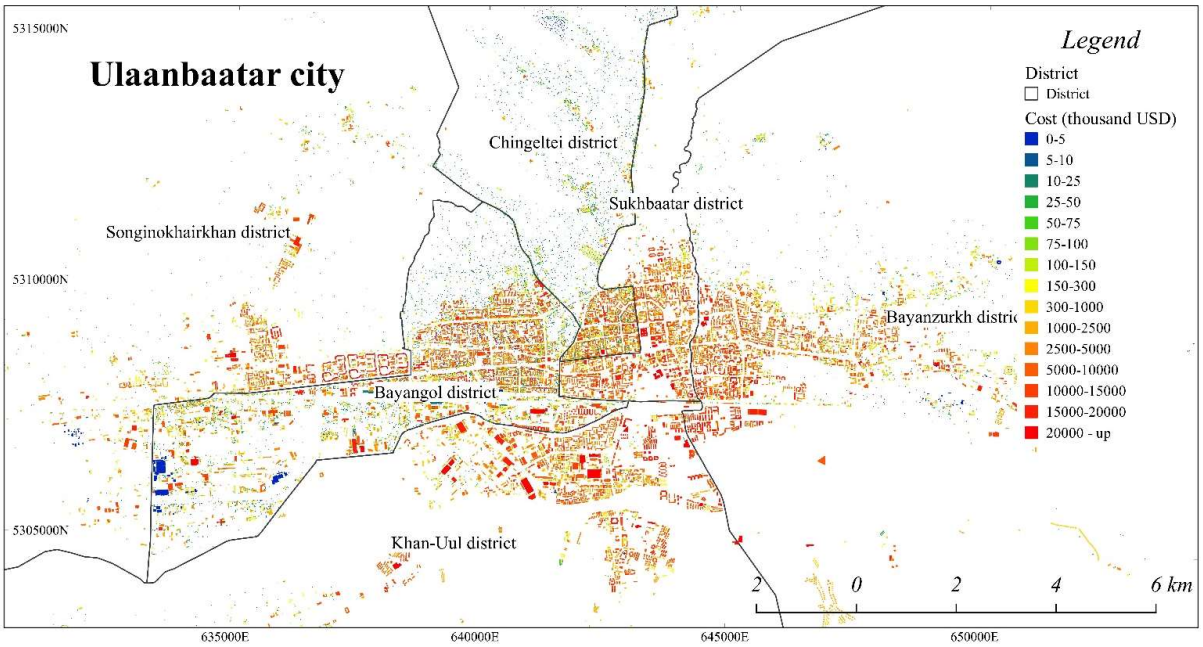

Figure 4-6. Distribution of construction costs (thousand USD) in UB.

4. 6. Validation

The statistic department of the Ulaanbaatar city office has published the total amount of property in several districts from 2006 (The Ulaanbaatar Statistic & http://ubstat.mn/StatTable=381, n.d.). The city authorities have developed the statistical data with each year based on the procurement report every year. Since the number of buildings constructed after 2010 in the inventory data would be more reliable than those of older buildings, our estimation is compared with the statistics since 2010. Figure 4-7 compares the total amount of costs in six districts (SHD: Songinokhairkhan district, HUD: Khan-Uul district, BZD-Bayanzurkh district, BGD: Bayangol district, SBD: Sukhbaatar district, and CHD: Chingeltei district) with the statistics for each year after 2010.

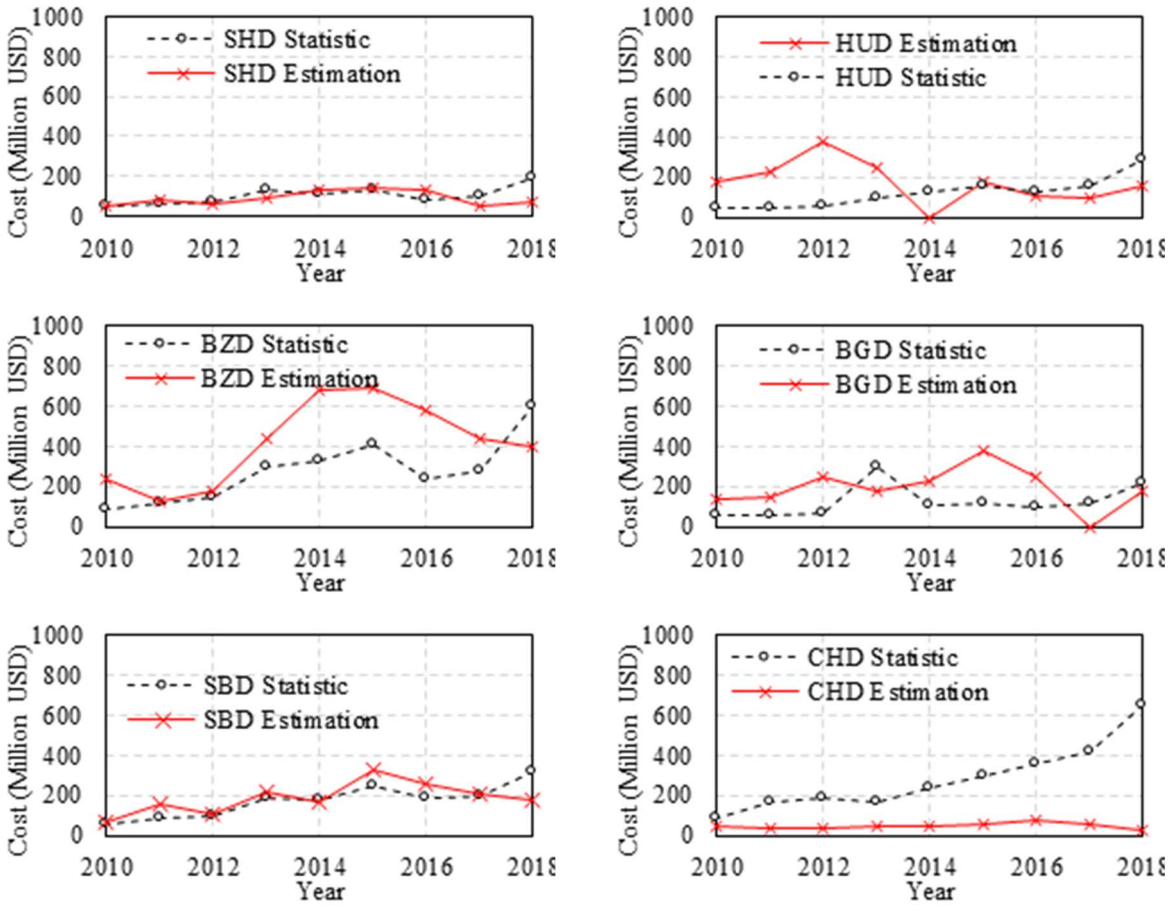

Figure 4-7. Comparison of cost estimation and statistical data of central district of Ulaanbaatar year by year. SHD: Songinokhairkhan district, HUD: Khan-Uul district, BZD-Bayanzurkh district, BGD: Bayangol district, SBD: Sukhbaatar district, CHD: Chingeltei district.

Our estimations in SHD, SBD, and BGD show good agreement with the statistical data. However, the estimations in BZD and CHD are remarkably smaller than the statistics. One of the underestimations might be that BZD and CHD include many ger areas where a number of unregistered buildings have been constructed. Since our estimation did not consider ger houses, our estimation would be significantly smaller than the statistics.

4. 7. Conclusions

In this chapter, the building inventory data is updated from the existing data by estimating heating type, structural class, and construction year for the unregistered buildings to estimate the buildings' construction cost. Since Mongolia is located in the cold region, the heating type is a critical item that controls the construction cost. The building information is estimated from the location, building use, building height, and building shape such as area, length, and width of the registered buildings. I compare the structural types estimated by the proposed method and the pictures of typical buildings in the StreetView. Whereas it is difficult to know the actual structural type from the field photo, the results show that the estimated structural types seem reasonable to the conditions of the actual buildings.

The construction cost for each building is evaluated based on the Mongolian construction code. I confirmed that the estimated construction costs aggregated for the districts show good agreement with the official statistics for the building properties.

CHAPTER 5. LOSS ESTIMATION IN ULAANBAATAR CITY

5. 1. Introduction

The building class and the vulnerability functions proposed in the Global Assessment Report on Disaster Risk Reduction 2013 (GAR-13) were used in this study. The building heights are categorized into three classes (Low-rise, Mid-rise, and High-rise) in the building classes of the GAR-13. The typical periods were also given to the building classes in GAR-13. Of course, the typical periods would not be accurate for individual buildings because actual building heights vary within the building category. Although the accuracies of the typical periods need to be discussed considering actual seismic behaviors of buildings in each country/region, it is beyond the scope of this study. Future studies need to discuss the applicability of the building categories and the vulnerability functions, including the typical periods to the target area. In this chapter, for that reason, we have tried microtremor measurement at several buildings in UB.

5. 2. Building dynamic characteristic

5. 2. 1. Measurement of buildings in UB

In the observations, I use the portable handheld microtremor sensor of GEODAQS-2S3D developed by ANET Inc., Japan. The sensor can measure the ambient motions in velocity with the lower limit of the frequency of 0.5 Hz (period of 2.0 s). The sampling of 100 Hz is applied during the observation, indicating the frequency coverage from 50 Hz to 0.5 Hz. I have measured the microtremor at the ground and top floor of the building and recorded it for three to ten minutes.

Figure 5-1 shows the map of the microtremor measurement of UB during the visit to Mongolia 2019.

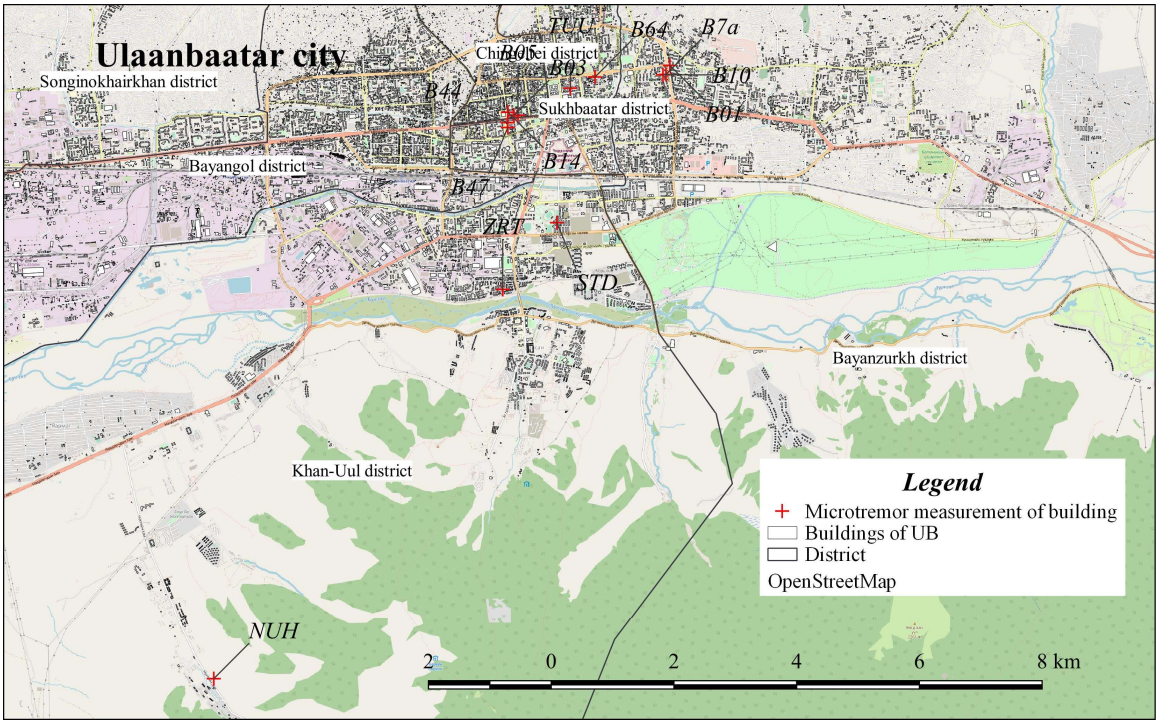

Figure 5-1. Distribution of microtremor measurement for buildings in UB.

The most common type of apartment has been chosen to have microtremor measurement, Table 5-1 shows information of buildings. I have selected typical old masonry apartments in the central district of UB. Which was built Chinese construction influence and constructed early years (1960-1970) of

Ulaanbaatar city. These buildings are constructed of thick masonry walls with timber or concrete slab. Next buildings are precast buildings constructed under the soviet construction code, basically 4 stories, 5 stories, 9 stories, and 12 stories in 1970-1990. One of the ordinary apartment buildings in UB uses precast panels to connect welded reinforcing bars. The following buildings are new RC buildings constructed after 2000 years. Building less than 7 stories is constructed RC frame with masonry or light block outer walls. More than 7 story buildings are constructed RC frames with diaphragm walls and masonry or light block walls. The last building is a steel high-rise hotel building, constructed in 2013.

Table 5-1. Microtremor measurement of buildings in UB

Name of sites	**Name of the building**	**Structural type**	**Number of Story**	**Construction Year**	**Predominant period (s)**	
					X	Y
B64	Apartment 64	Masonry	5	1980	0.244	0.213
B47	Apartment 47	Masonry	3	1960-1970	0.169	0.193
B44	Apartment 44	Masonry	4	1960-1970	0.281	0.223
B05	Apartment 05	Masonry	4	1973	0.27	0.25
B03	Apartment 03	Masonry	4	1973	0.259	0.293
B14	Apartment 14	Masonry	3	1960	0.203	0.19
B10	Apartment 10	Precast	4	1970	0.235	0.209
B01	Apartment 1	Precast	9	1985	0.347	0.353
B7a	Apartment 7A	Precast	12	1988	0.525	0.539
STT	Apartment STT	Reinforced concrete frame	9	2009	0.445	0.476
ZRT	Apartment 34	Reinforced concrete frame	5	2008	0.213	0.225
NUH	NUHT House	Reinforced concrete frame	3	2018	0.126	0.128
TUU	Tuushin hotel	Steel frame	25	2013	2.05, 1.02, 0.53	1.86, 1.02, 0.45

Based on the measurement, I calculate the top and bottom floor X and Y Fourier spectrum shown in Figure 5-2 to Figure 5-11. The Parzen window with a bandwidth of 0.3 Hz is applied for the Fourier spectrum. Three 20.48 s duration parts with less traffic and artificial noises are extracted from the

records, mean values of the three spectral ratios are calculated.

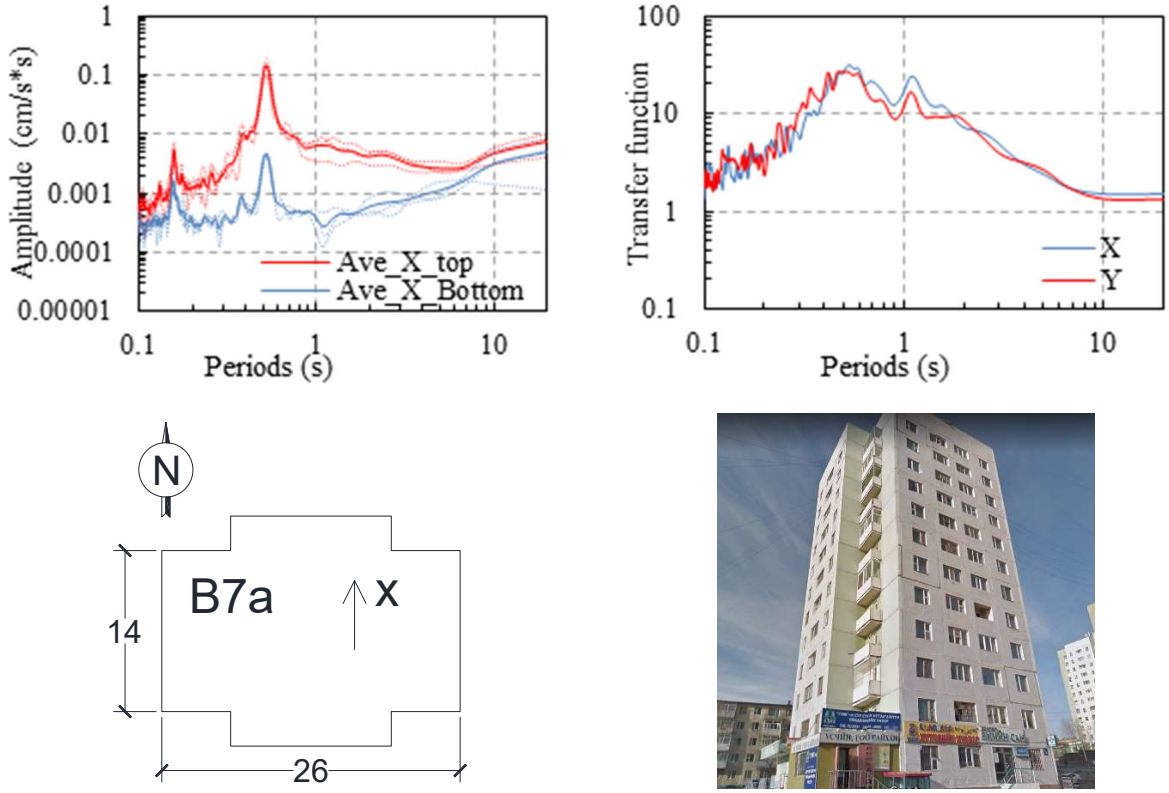

Figure 5-2. Microtremor measurement of buildings in UB

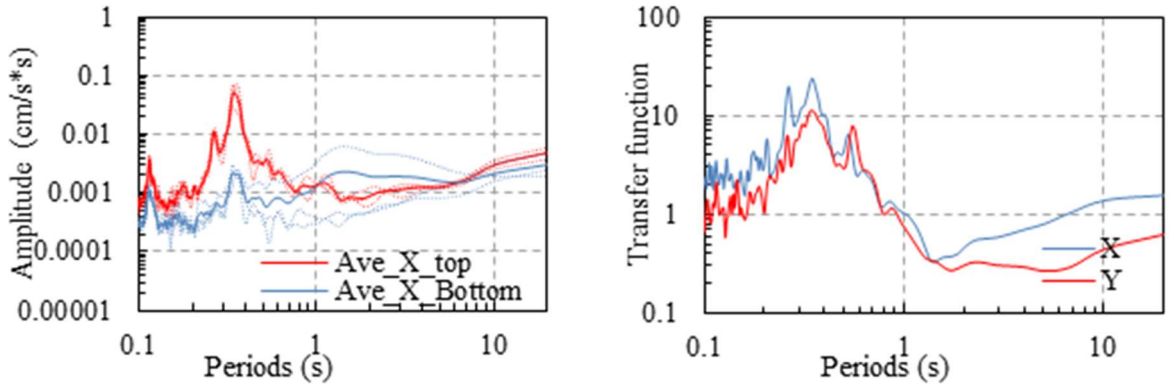

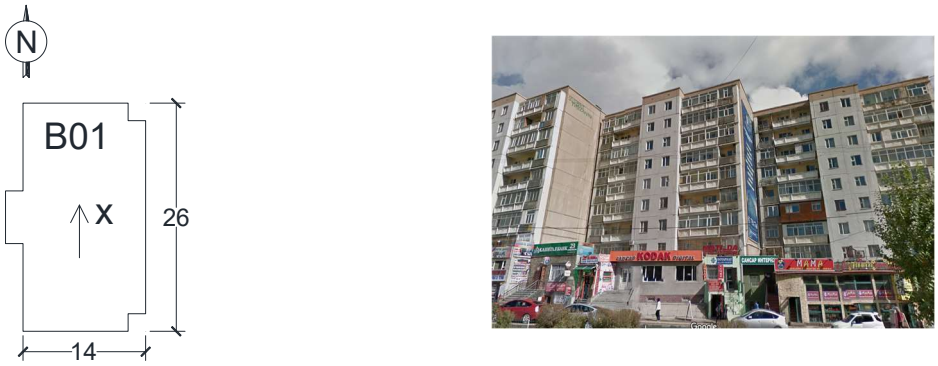

Figure 5-3. Microtremor measurement of buildings in UB

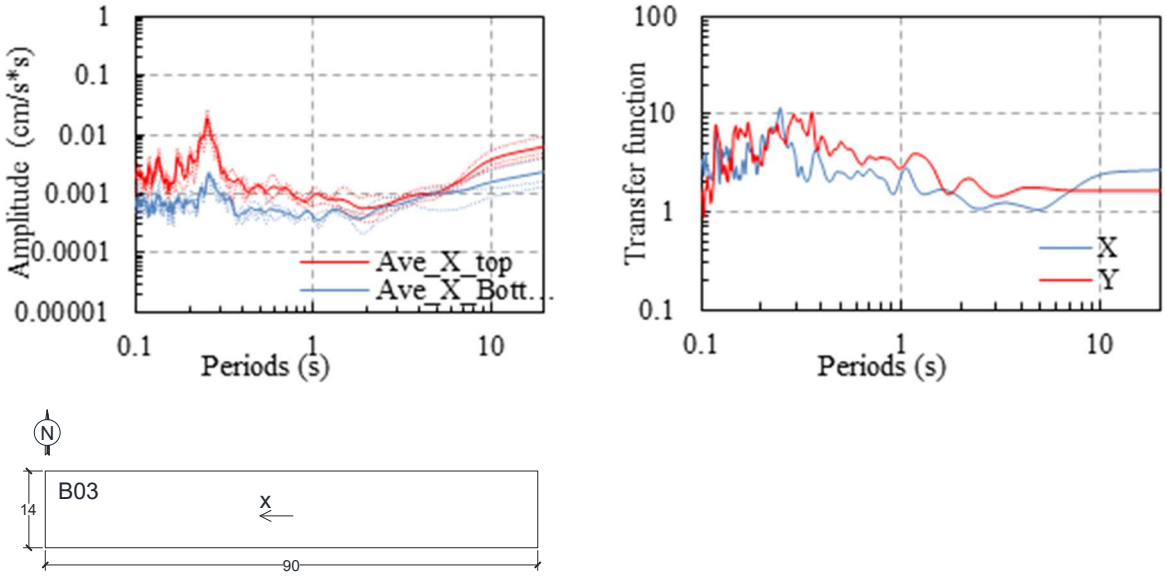

Figure 5-4. Microtremor measurement of buildings in UB

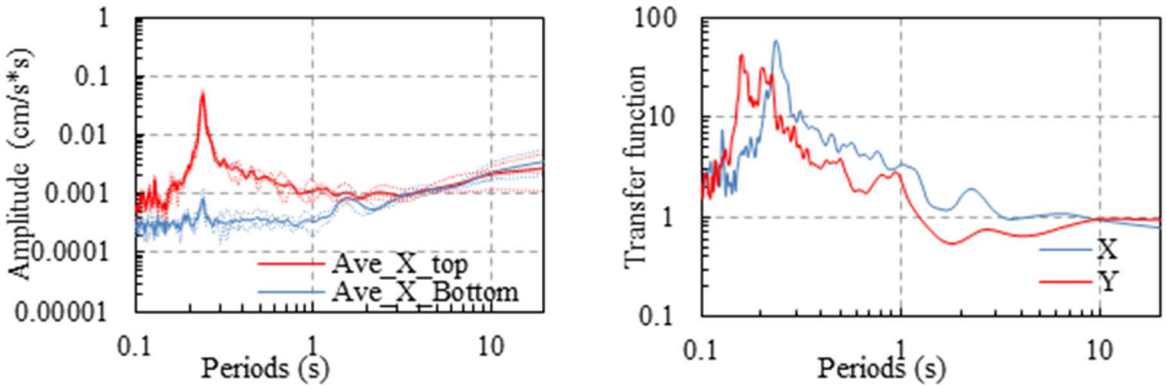

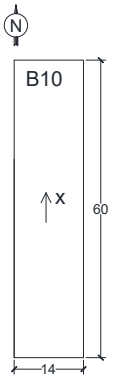

Figure 5-5. Microtremor measurement of buildings in UB

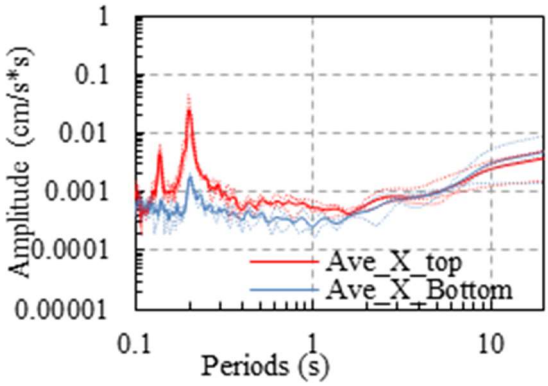

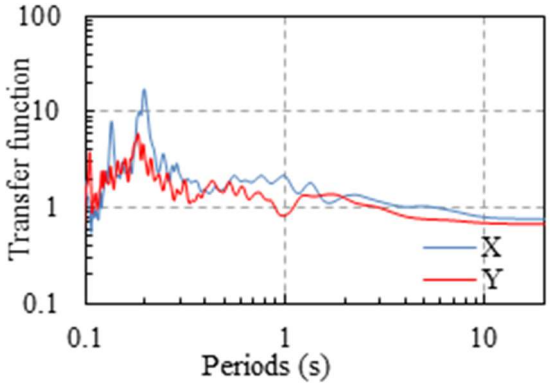

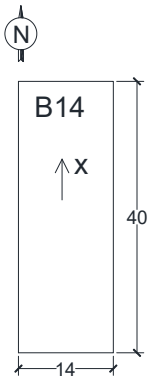

Figure 5-6. Microtremor measurement of buildings in UB

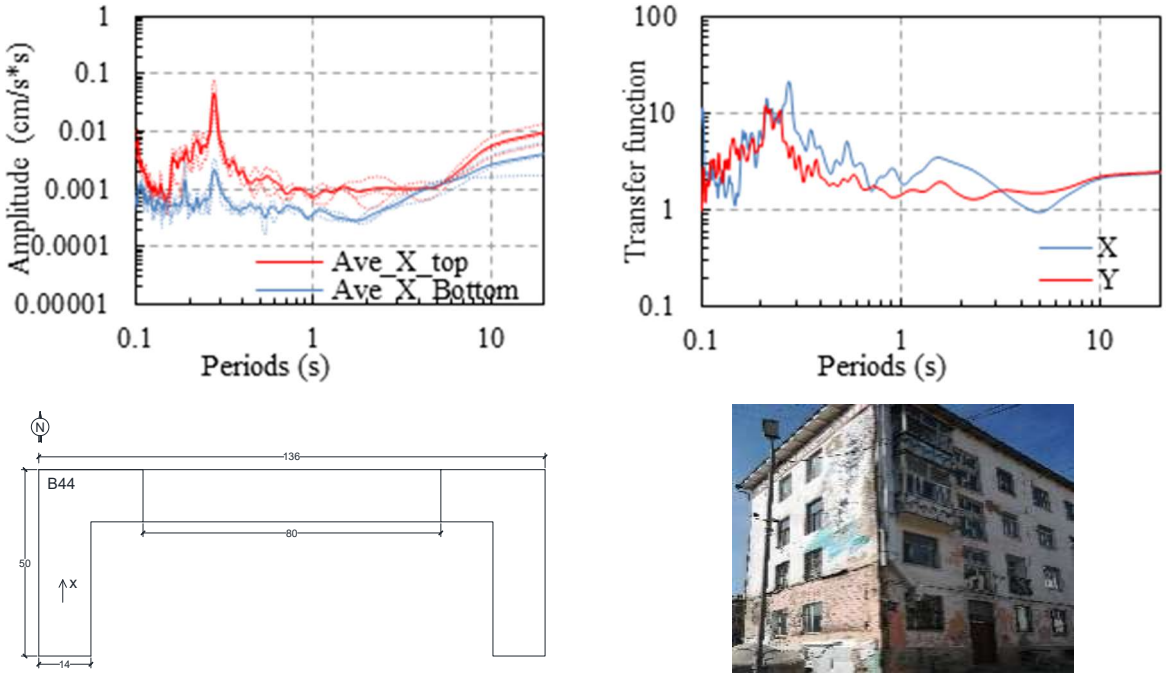

Figure 5-7. Microtremor measurement of buildings in UB

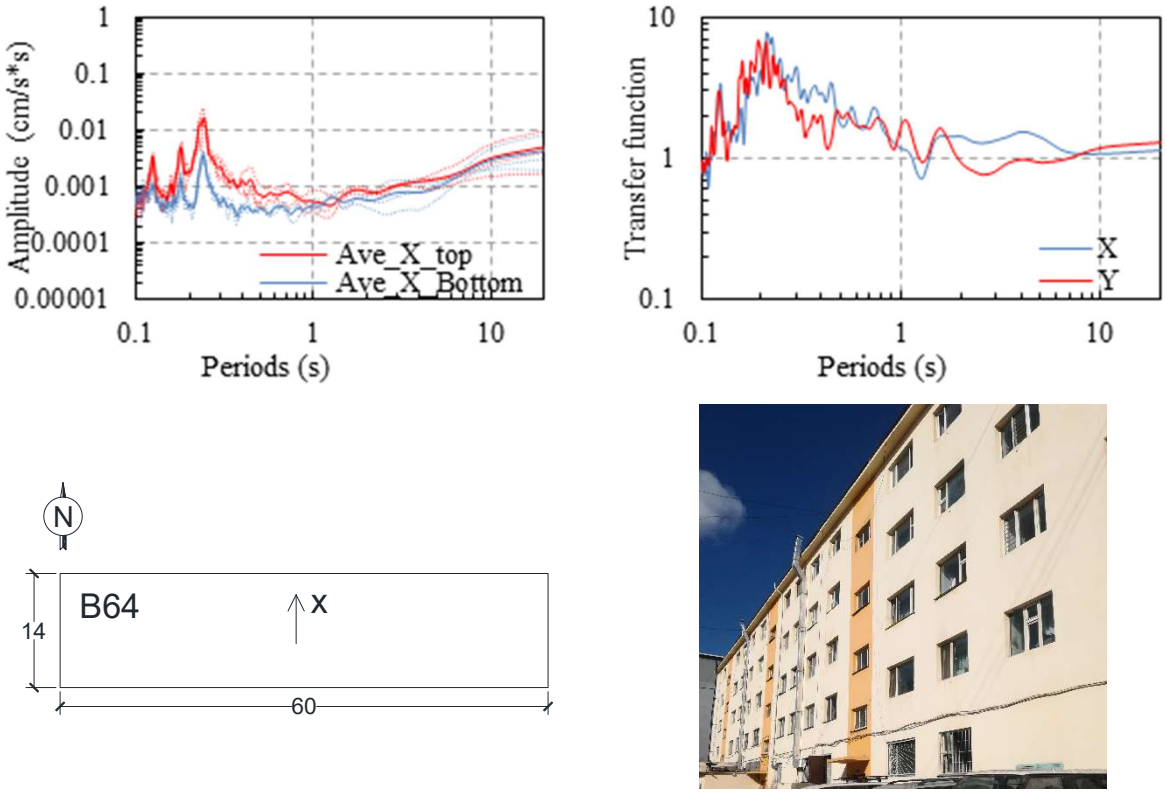

Figure 5-8. Microtremor measurement of buildings in UB

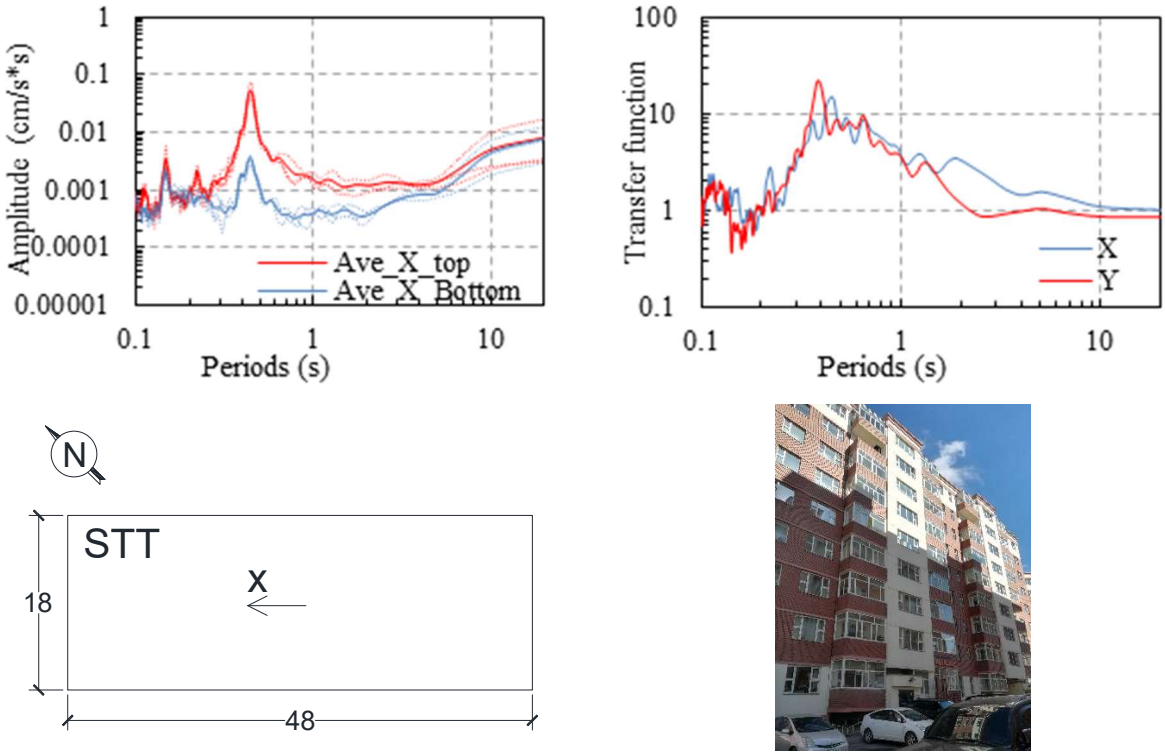

Figure 5-9. Microtremor measurement of buildings in UB

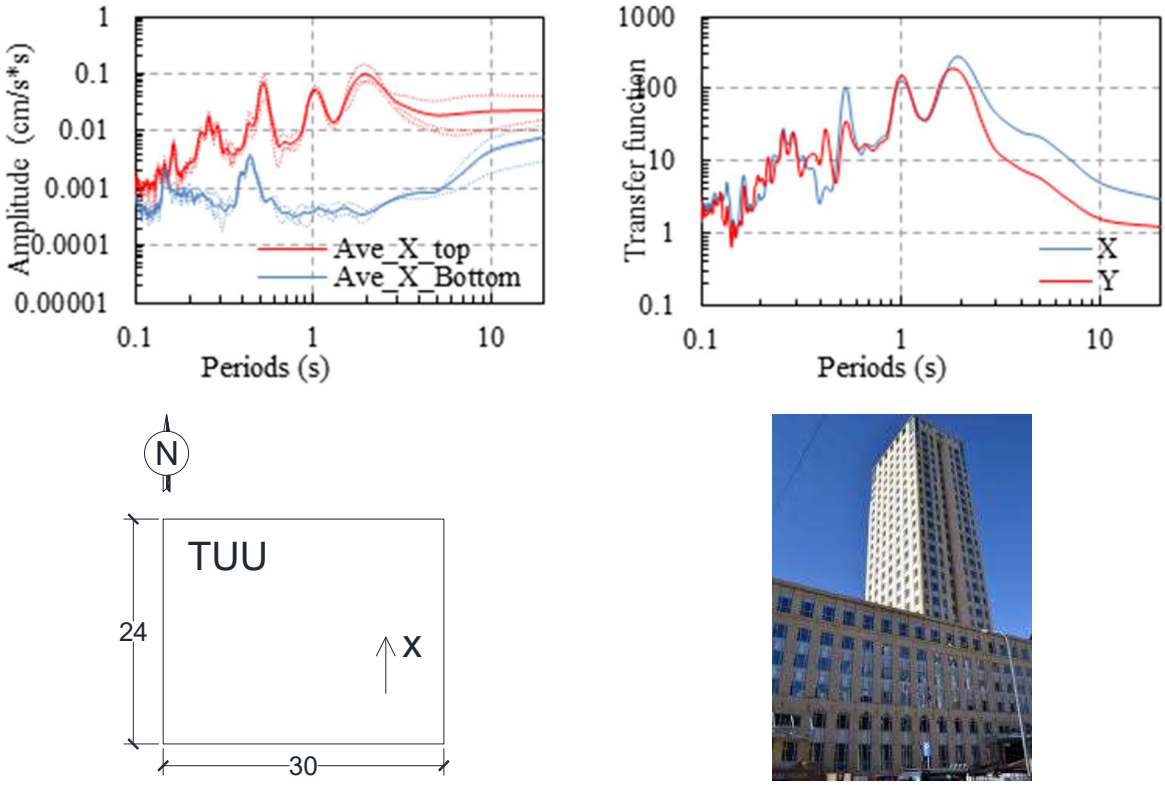

Figure 5-10. Microtremor measurement of buildings in UB

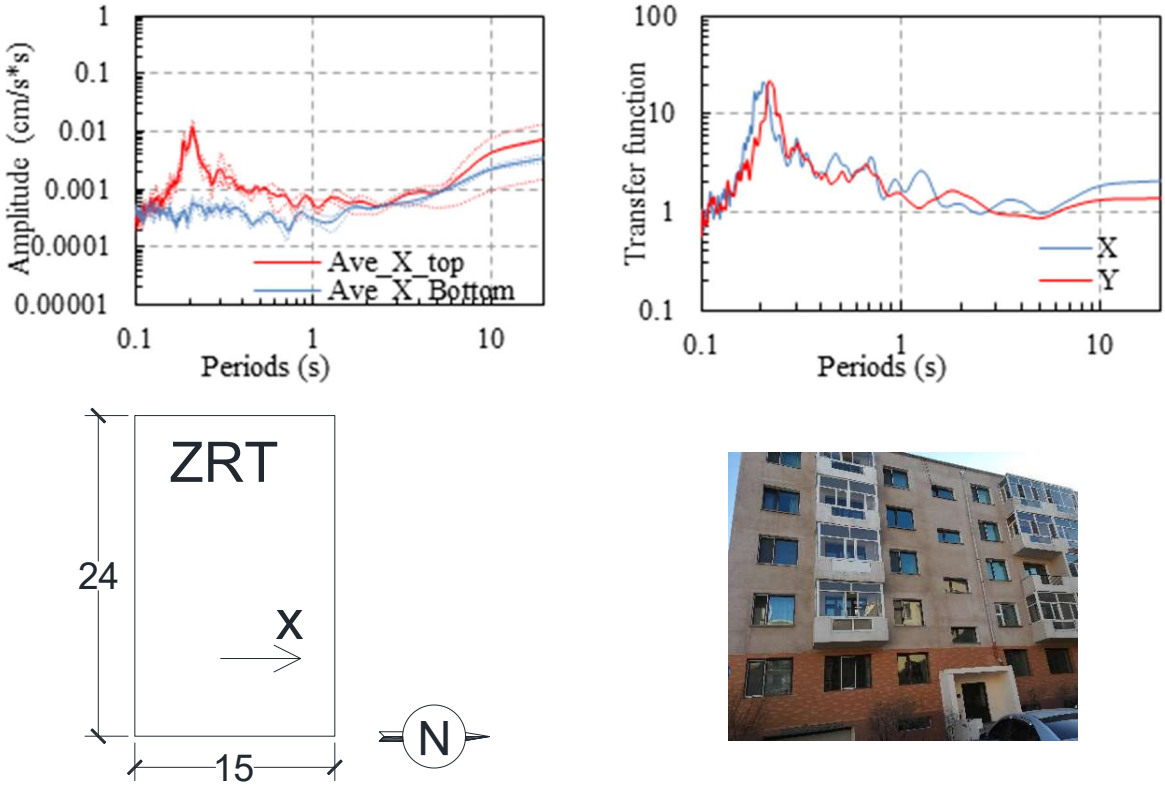

Figure 5-11. Microtremor measurement of buildings in UB

Figure 5-2 to Figure 5-11 shows example microtremor measurement of selected buildings. These figures show a building plan with the direction of axis, photo, MHVR, and Fourier spectrum.

5. 2. 2. Relationship between building heights and predominant periods

Figure 5-12 shows the relationship of predominant period and building height of masonry, precast, RC and steel structure in selected buildings. Due to the cold climate, most of the buildings has very thick masonry outer wall, a short height of story is common in UB buildings. Dynamic characteristics are different from other country buildings.

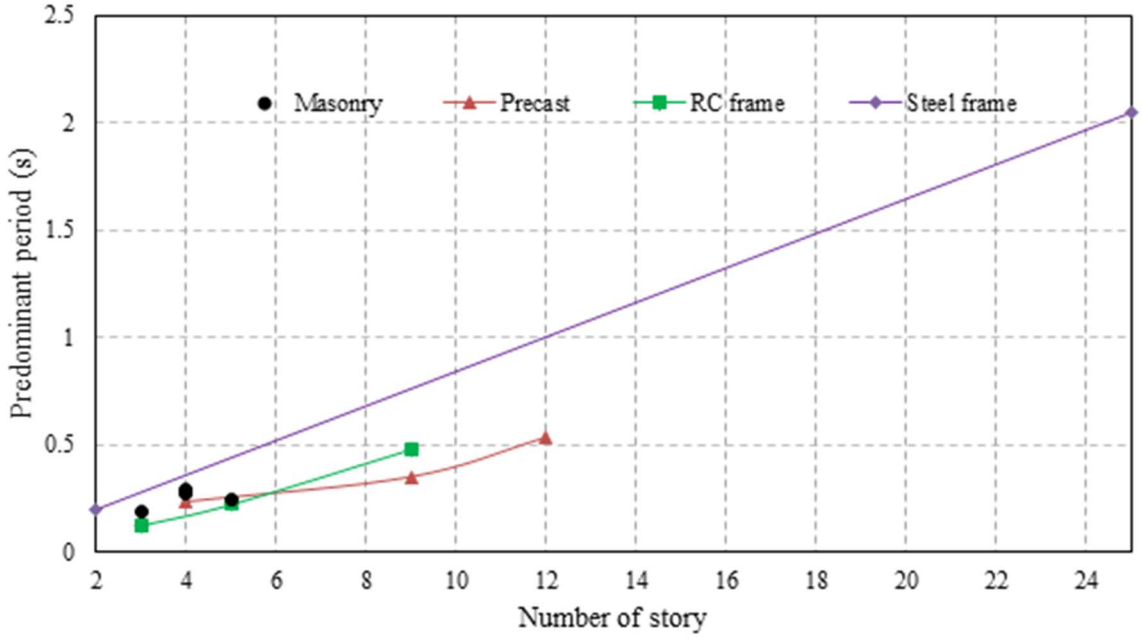

Figure 5-12. Relation of predominant period and building height in each structural type.

5. 3. Vulnerability assignment

In this study, the global vulnerability functions developed in the GAR-13 (Engineering & ITEC S.A.S. – INGENIAR LTDA. – EAI S.A., 2013; Yamin et al., 2014, 2017) are used to estimate building losses by a scenario earthquake. The seismic vulnerability functions of the GAR-13 represent the relationship between spectral acceleration for the typical period of a building class and expected repair cost in percentage (Mean damage ratio: MDR). The vulnerability functions were developed for 47 building classes considering structural types and building heights, and four design levels (High, Medium, Low and Poor) in the GAR-13.

Seismic activities were considered in 1970 in the Mongolian construction code. And, after 1990, Mongolian construction practices have introduced modern construction technologies. Especially, 2010, high-rise building technology is widely used in practice. That's why we are considered three different categories before 1970, 1970-1990, and 1990-2010.

We have considered seismic code with a vulnerability curve of GAR-13. In this method, there are four levels of quality of building vulnerability.

High (H): fully complies with earthquake resistance requirements of international seismic design building codes in terms of load capacity.

Medium (M): moderately complies with earthquake resistance requirements.

Low (L): does not generally comply with minimum earthquake resistance specifications.

Poor (P): does not comply with any basic earthquake resistance requirement.

These can be considered seismic code requirements.

I assign each building in the updated inventory data to the classes of GAR-13 based on the criteria shown in Table 5-2. The building classes are classified considering the structural type and the number of stories. The design levels are classified considering the building location, building use, and construction year. Since many non-engineered masonry houses exist in ger areas, poor design level is given to the buildings in the ger areas. The higher design level is assigned to public buildings such as

government buildings, city offices, schools, and hospitals. The building area and construction year are considered in classifying the design levels of masonry, timber, and RC with masonry wall buildings. A higher design level is also given to the larger or newer buildings in the classes. Figure 8 illustrates the distribution of the assigned building classes.

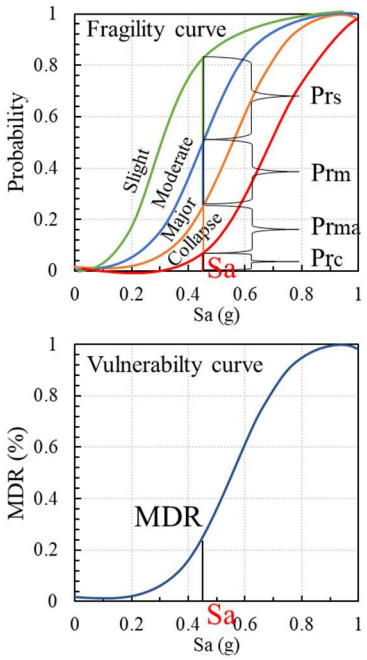

MDR(%)=Prs*Rs+Prm*Rm+Prma*Rma+Prc*Rc

Pr- damage state probability
R- repair cost in percentage each damage state

For probabilistic disaster risk assessment, vulnerability function is the relation of the intensity of the hazard and relative direct physical impact.

Each vulnerability function is characterized by a value known as the mean damage ratio (MDR) and its corresponding variance for each level of hazard intensity.

Figure 5-13. Relationship between fragility and vulnerability curve in GAR-13.

Figure 5-15 shows the vulnerability functions of the GAR-13 used in this study. The horizontal axis indicates a spectral acceleration in *g* at the typical period for each building class shown in Table 5-2. According to the vulnerability functions, a considerable repair cost is expected in unreinforced masonry buildings such as URML and URMM. Those vulnerability functions are used in the following seismic loss estimation.

Table 5-2**.** Building classes of GAR-13 and criteria of building information in the inventory data.

Building class in GAR-13			Criteria of building information in inventory data					
Class ID	Typical period (s)	Design level	Structural type	Story	Location	Use	Building area, A (m2)	Construction year, Y
URML	0.35	Poor	Masonry	1-3	In ger area	-	-	Y<1970
		Low			Others	Not public	-	Y<1970
		Medium			Others	Public	-	Y<1970
RM1L	0.35	Poor	Masonry	1-3	In ger area	-	-	Y>1971
		Low			Others	-	A<75	1971<Y<1990
		Medium			Others	Public	A>75	1971<Y<1990
		High			Others	-	-	Y>1991
URMM	0.56	Poor	Masonry	4-7	In ger area	-	-	Y<1970
		Low			Others	Not public	-	Y<1970
		Medium			Others	Public	-	Y<1970
RM1M	0.50	Poor	Masonry	4-7	In ger area	Not public	-	Y>1971
		Low			In ger area	Public	-	Y>1971
		Medium			Others	Not public	-	Y>1971
		High			Others	Public	-	Y>1971
RM2H	1.09	Low	Masonry	8≦	In ger area	-	-	
		High			Others	Public	-	Y<1990
W1	0.35	Poor	Timber	1-3	In ger area	Not public	-	-
		Low			In ger area	Public	-	-
		Medium			Others	-	A<2000	-
		High			Others	-	A>2000	-
C1L	0.40	Low	RC, RC with shear wall	1-3	In ger area	-	-	-
		Medium			In industrial area	-	-	-
		High			Others	-	-	-
C1M	0.75	Low	RC, RC with shear wall	4-7	In ger area	-	-	-
		Medium			In industrial area	-	-	-
		High			Others	-	-	-
C3L	0.35	Poor	RC with masonry wall	1-3	In ger area	-	-	Y<1970
		Low			In ger area	-	-	Y>1971
		Medium			Others	-	-	Y<1990

		High			Others	-	-	Y>1991
C3M	0.56	Poor	RC with masonry wall	4-7	In ger area			Y<1970
		Low			In ger area			Y>1971
		Medium			Others			Y<1990
		High			Others			Y>1991
C3H	1.09	Medium	RC with masonry wall	8≦	In ger area	-	-	Y<1990
		High			-	-	-	Y>1991
C4H	1.09	Low	RC with shear wall	8≦	In ger area	-	-	-
		Medium			In industrial area	-	-	-
		High			Others	-	-	-
PC2L	0.35	Low	Precast	1-3	In ger area	-	-	-
		Medium			In industrial area	-	-	-
		High			Others	-	-	-
PC1M	0.56	Low	Precast	4-7	In ger area	-	-	-
		Medium			In industrial area	-	-	-
		High			Others	-	-	-
PC1H	1.09	Low	Precast	8≦	In ger area	-	-	-
		Medium			In industrial area	-	-	-
		High			Others	-	-	-
S1L	0.50	Low	Steel	All	In ger area	-	-	-
		Medium			In industrial area	-	-	-
		High			Others	-	-	-

URM: Unreinforced masonry bearing wall, RM1: Reinforced masonry bearing wall with wood or metal deck diagrams, RM2: Reinforced masonry bearing wall with precast concrete diagrams, W1: Wood light frame, C1: Concrete moment frame, C3: Concrete frame with unreinforced masonry infill walls, C4: Reinforced concrete frames and concrete shear walls, PC2: Precast concrete frames with concrete shear walls, PC1: Precast concrete tilt-up walls

Public: Public buildings such as government buildings, office buildings, schools, and hospital

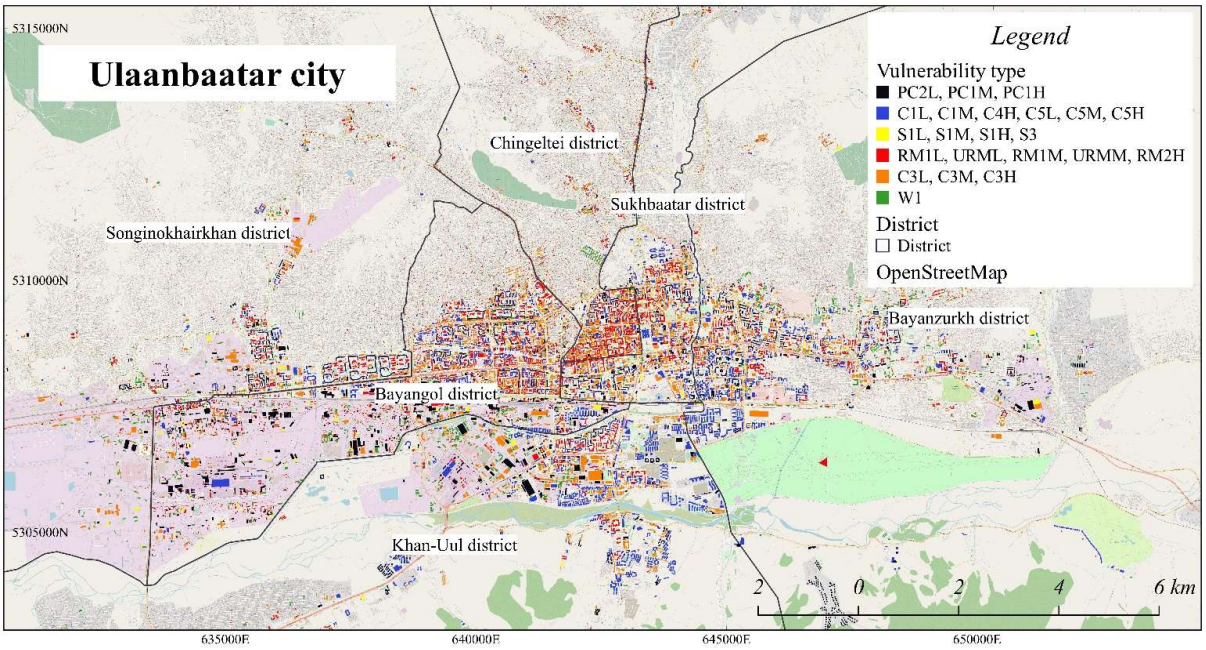

Figure 5-14. Distribution of building classes in UB.

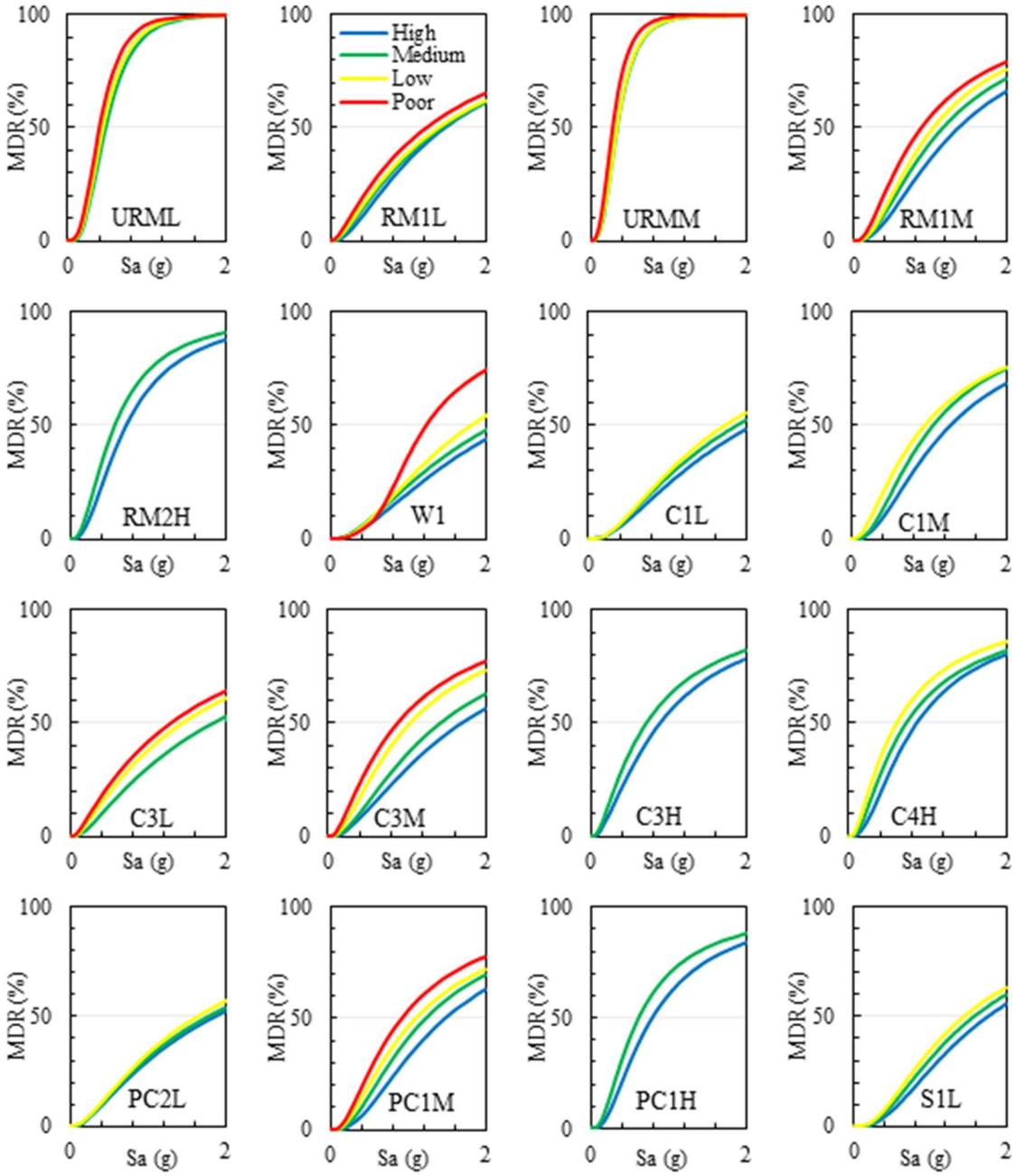

Figure 5-15. Vulnerability functions of GAR-13 were used in this study.

5. 4. Seismic loss estimation

The economic loss of the buildings by the scenario earthquake is estimated by the simulated response spectral accelerations, the vulnerability functions, and the construction costs estimated in chapter 3 and 4. Figure 5-15 shows the distribution of the estimated MDRs in the percentage of each building. Higher MDRs than 50 % are estimated in the western and eastern part of the UB area, whereas the MDRs in most of the buildings in the central area is lower than 20 %.

The repair costs of the buildings are estimated from the construction costs by multiplying the MDRs shown in Figure 5-16. Figure 5-17 shows the distribution of the expected repair costs of the buildings in thousand USD for the scenario. The repair costs for most of the buildings are lower than 20 thousand USD. Those buildings correspond to the small low-rise masonry buildings. Higher repair costs are expected in more significant buildings, especially in the southern part of the UB area, because high-rise residential apartment buildings have concentrated in recent years.

In the updated building inventory data, the total construction cost for the buildings in UB is approximately 28.7 billion USD. The result of the loss estimation shows that the total amount of repair costs for damaged buildings is approximately 3.4 billion USD in the scenario. According to the economic situation by The World Bank (*The World Bank, GDP (Current US$) - Mongolia*, n.d.), the average of the recent 5-years growth domestic product (GDP) in Mongolia is approximately 13 billion USD. It indicates that the total direct losses of the buildings in the scenario correspond to approximately 26 % of the Mongolian GDP. Jaiswal and Wald (Jaiswal & Wald, 2013) estimated the direct shaking-related economic losses in the recent worldwide M7 class earthquakes as 3.0 billion USD for the Haiti earthquake on Jan. 12, 2010 (M7.0), 2.0 billion USD for the Canterbury, New Zealand earthquake on Sep. 3, 2010 (M7.0), and 2.0 billion USD for the Eastern Turkey earthquake on Oct. 23, 2011 (M7.1), respectively.

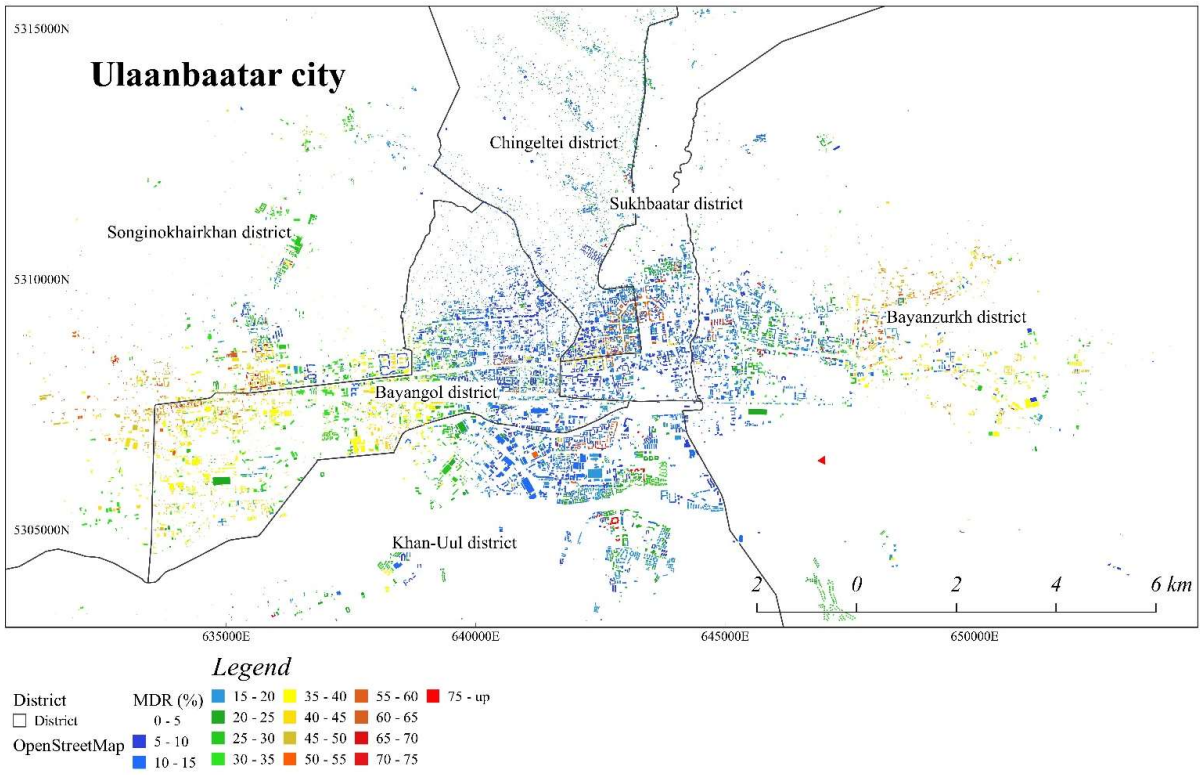

Figure 5-16. Distribution of MDR (mean damage ratio) estimated by vulnerability assessment in UB.

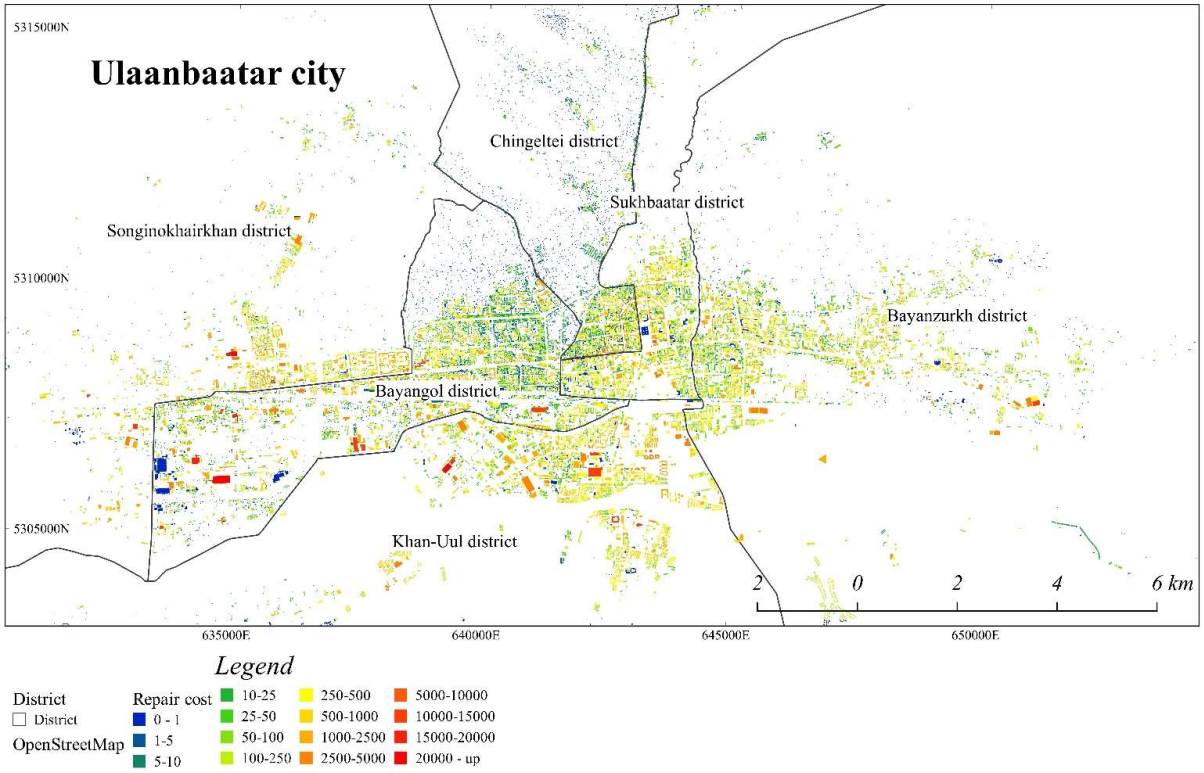

Figure 5-17. Distribution of building losses (repair costs in thousand USD) in UB.

Whereas our estimation's seismic and urban conditions are different from those in the previous earthquakes, our estimated economic loss is consistent with those in the earthquakes. If indirect losses such as business interruption are counted in the loss estimation, much more significant losses would be expected. In order to reduce the building damage and losses, seismic retrofitting and structural rehabilitation, especially non-engineered buildings such as unreinforced masonry, would be substantial.

5. 5. Conclusions

In this chapter, the financial building loss due to the scenario earthquake is estimated based on the strong motion simulation, the updated building inventory data, and global vulnerability functions developed in GAR-13. Also, predominant periods of typical buildings in UB are compared with GAR-13 results. Future studies should discuss the applicability of vulnerability curves. The building vulnerability classes are assigned by the structural type, building height, and location.

The result of the loss estimation shows the total amount of the loss is approximately 3.4 billion USD. In contrast, Mongolia's recent growth domestic product (GDP) is 13 billion USD, indicating the loss reaches approximately 26 % of the Mongolian GDP. The estimated loss almost corresponds to the direct shaking-related economic losses in the recent worldwide M7 class earthquakes.

CHAPTER 6. CONCLUSIONS

In this thesis, I introduced research about Earthquake Loss Estimation Based on Building Inventory Data and Strong Motion Prediction in Ulaanbaatar city, Mongolia. I estimated building losses due to a scenario earthquake. Although the building inventory data is available in UB, information on the structural type and construction year were not registered in some buildings. I estimated the structural type and construction year by applying the criteria based on the building characteristics in the existing inventory data. I confirmed that the estimated structural types show good agreement with the actual buildings. The construction costs of the UB buildings are calculated based on the updated building inventory data and the Mongolian construction code. The vulnerability functions of GAR-13 were also assigned to the buildings considering structural type, building height, and construction year.

Strong motion simulation for the scenario earthquake by the Emeelt fault was performed using the stochastic Green's function method and the equivalent linear ground response analysis. This research estimates the shear-wave velocity profiles in Ulaanbaatar (UB) city from the inversion analysis of the observed microtremor H/V spectral ratios (MHVRs) based on the diffuse field assumption. The joint inversions of the MHVRs and the surface wave dispersion curves obtained in the previous study are applied to the three sites in UB. The single inversion of the MHVRs estimates the Vs profiles for the rest of the sites. A comparison between the inverted shallow VS profiles and the geological borehole information has shown that reliable results within the methods' capabilities and resolution could be achieved. The seismic microzoning is performed based on the site amplifications obtained from the inverted Vs profiles. The UB areas are divided into five zones considering the site characterizations.

The largest site amplifications are expected around the Tuul river area, which consists deepest sedimentary deposit. Especially the Zone-V is the highest site amplified area, which means a significant risk for a newly constructed building district.

The peak ground accelerations for the scenario were estimated at more than 500 cm/s2 in UB, especially larger accelerations were expected in the western area located closer to the fault. By using the construction cost inventory, the vulnerability functions, and the simulated response accelerations, the expected repair costs of the damaged buildings were estimated. The direct loss of the buildings reached a total of 3.4 billion USD in the target area, which almost corresponds to approximately 26 % of the recent GDP in Mongolia. The developed inventory database and the procedure for the seismic loss estimation would be useful for considering counter-measures against future earthquake disasters for the national government and local municipalities.

The strengths of our approach can be summarized as that monetary loss of damaged buildings can be estimated not only for scenario earthquakes but also for an actual earthquake by using our developed building inventory. Generally, it would be complicated to estimate the total amount of loss immediately after an earthquake. Our developed approach can produce a damage distribution map and amount of building loss immediately after an earthquake if ground motion data is available. In addition to the wider-practical aspect and value of the performed study, the applicability of the obtained data can be used the earthquake insurance market for building stock in UB, Mongolia.

On the other hand, the limitations of our approach can be summarized as the applicability of the vulnerability functions, the accuracy of the seismic ground motion prediction, and the quality of building inventory data. Although we used the global vulnerability functions proposed in the GAR-13, the applicability needs to be discussed by considering the actual seismic capacity and dynamic

characteristics of UB buildings. Since detailed shear-wave velocity structure models in UB is not available yet, we applied one-dimensional ground response analysis in the seismic ground motion prediction. If a more detailed Vs-model would be available by future dense geophysical explorations, 3D ground motion simulation techniques such as the finite difference method can be applied to estimate not only body waves but also basin-induced surface waves. Finally, the building inventory data of UB still has uncertainties in heating types, structural types, and construction years because it was challenging to determine them from the currently available data accurately. Updating the inventory data would be one of the critical issues for reliable earthquake loss assessment in UB.

References

Arai, H. (2005). S-Wave Velocity Profiling by Joint Inversion of Microtremor Dispersion Curve and Horizontal-to-Vertical (H/V) Spectrum. *Bulletin of the Seismological Society of America*, *95*(5), 1766–1778. https://doi.org/10.1785/0120040243

Arai, H., & Tokimatsu, K. (2004). S-Wave Velocity Profiling by Inversion of Microtremor H/V Spectrum. *Bulletin of the Seismological Society of America*, *94*, 53–63. https://doi.org/10.1785/0120030028

Boore, D. M. (1983). *Stochastic simulation of high-frequency ground motions based on seismological models of the radiated spectra*. *73*(6), 1865–1894. https://doi.org/10.1785/BSSA07306A1865

Building Seismic Safety Council (BSSC). (2009). *NEHRP recommended seismic provisions for new buildings and other structures, Part 1 (Provisions) and Part 2 (Commentary to ASCE/SEI 7)*. Federal Emergency Management Agency, Washington, D.C.

Chimed, O. (2011). *Site effects characterization in the basin of Ulaanbaatar*. University of Strasbourg.

City, E. M. D. of the C. C., & Japan International Cooperation Agency, (JICA). (2013). *Mongolia The Project for Strengthening the Capacity of Seismic Disaster Risk Management in Ulaanbaatar City Final Report*. Asian Disaster Reduction Center, Urban Disaster Research Institute Tokyo Electric Power Services Co., Ltd. https://openjicareport.jica.go.jp/661/661/661_115_12129102.html

Danielson, J. J., & Gesch, D. B. (n.d.). *Global Multi-resolution Terrain Elevation Data 2010*

(GMTED2010). 34.

Dolce, M., Kappos, A., Masi, A., Penelis, G., & Vona, M. (2006). Vulnerability assessment and earthquake damage scenarios of the building stock of Potenza (Southern Italy) using Italian and Greek methodologies. *Engineering Structures*, *28*(3), 357–371. https://doi.org/10.1016/j.engstruct.2005.08.009

Engineering, C. I. C. for N. M. in & ITEC S.A.S. – INGENIAR LTDA. – EAI S.A. (2013). *Probabilistic Modelling of Natural Risks at the Global Level: Global Risk Model* (p. 719). Ingeniar Ltda. http://www.preventionweb.net/gar

Ferreira, T. M., Vicente, R., Mendes da Silva, J. A. R., Varum, H., & Costa, A. (2013). Seismic vulnerability assessment of historical urban centres: Case study of the old city centre in Seixal, Portugal. *Bulletin of Earthquake Engineering*, *11*(5), 1753–1773. https://doi.org/10.1007/s10518-013-9447-2

Fujishima, D., Miura, H., Kanno, T., Shigefuji, M., Abiru, T., Nakamura, H., & Aoi, S. (2018). Estimation accuracy of shear wave velocity profiles inverted from earthquake and microtremor H/V spectral ratios. *Proceedings of 15th Japan Earthquake Engineering Symposium*, 2141–2149.

García-Jerez, A., Piña-Flores, J., Sánchez-Sesma, F. J., Luzón, F., & Perton, M. (2016). A computer code for forward calculation and inversion of the H/V spectral ratio under the diffuse field assumption. *Computers & Geosciences*, *97*, 67–78.

https://doi.org/10.1016/j.cageo.2016.06.016

Google map, https://www. google. com/maps. (n.d.). *(assessed on Sep. 1, 2021)*. https://www.google.com/maps. Retrieved September 1, 2021, from https://www.google.com/maps

Haskell, N. A. (1960). Crustal reflection of plane SH waves. *Journal of Geophysical Research (1896-1977)*, *65*(12), 4147–4150. https://doi.org/10.1029/JZ065i012p04147

Irikura, K. (1986). Prediction of Strong Acceleration motions using Empirical Green's function. *Proceedings of Seventh Japan Earthquake Engineering Symposium*, 151–155. http://www.kojiro-irikura.jp/pdf/7th_J_Earthquake_Eng_Sympo.pdf

Irikura, K., & Miyake, H. (2011). Recipe for Predicting Strong Ground Motion from Crustal Earthquake Scenarios. *Pure and Applied Geophysics*, *168*(1–2), 85–104. https://doi.org/10.1007/s00024-010-0150-9

Jaiswal, K., & Wald, D. J. (2013). Estimating economic losses from earthquakes using an empirical approach. *Earthquake Spectra*, *29*(1), 309–324. USGS Publications Warehouse. https://doi.org/10.1193/1.4000104

Kamae, K., Irikura, K., & Pitarka, A. (n.d.). *A Technique for Simulating Strong GroundMotion Using Hybrid Green's Function*. 12.

Kawase, H., Mori, Y., & Nagashima, F. (2018). Difference of horizontal-to-vertical spectral ratios of observed earthquakes and microtremors and its application to S-wave velocity inversion

based on the diffuse field concept. *Earth, Planets and Space*, *70*(1), 1. https://doi.org/10.1186/s40623-017-0766-4

Kircher, C. A., Reitherman, R. K., Whitman, R. V., & Arnold, C. (1997). Estimation of Earthquake Losses to Buildings. *Earthquake Spectra*, *13*(4), 703–720. https://doi.org/10.1193/1.1585976

Kirkpatrick, S., Gelatt, C. D., & Vecchi, M. P. (1983). Optimization by Simulated Annealing. *Science*, *220*(4598), 671–680. https://doi.org/10.1126/science.220.4598.671

KITSUNEZAKI, C. (1990). Estimation of P- and S-wave velocities in deep soil deposits for evaluating ground vibrations in earthquake. *Journal of Japan Society for Natural Disaster Science*, *9*, 1–17. https://ci.nii.ac.jp/naid/10030726468/en/

Koyamada, K., Miyamoto, Y., & Miura, K. (2003). Nonlinear property for surface strata from natural soil samples. *Proceedings of the 38th Japan National Conference on Geotechnical Engineering*, 2077-2078 (in japanese).

Lachetl, C., & Bard, P.-Y. (1994). Numerical and Theoretical Investigations on the Possibilities and Limitations of Nakamura's Technique. *Journal of Physics of the Earth*, *42*(5), 377–397. https://doi.org/10.4294/jpe1952.42.377

Lermo, J., & Chivez-Garcia, F. J. (n.d.). *Are Microtremors Useful in Site Response Evaluation?* 15.

Matsuoka, M., Mito, S., Midorikawa, S., Miura, H., Quiroz, L. G., Maruyama, Y., & Estrada, M. (2014). Development of Building Inventory Data and Earthquake Damage Estimation in Lima, Peru for Future Earthquakes. *Journal of Disaster Research*, *9*(6), 1032–1041.

https://doi.org/10.20965/jdr.2014.p1032

Ministry of Construction and Urban Development in Mongolia. (2016). *Building and infrastructure unit cost*.

Munkhsaikhan, A. (2016). *Seismic activity near Ulaanbaatar: Implication for seismic hazard assessment* [University of Strasbourg]. https://tel.archives-ouvertes.fr/tel-01425480

Murao O., & Yamazaki F. (2002). Building fragility curves for the 1995 Hyogoken-Nanbu earthquake based on CPIJ & AIJ's survey results with detailed inventory. *Journal of Structural and Construction Engineering (Transactions of AIJ)*, *67*(555), 185–192. https://doi.org/10.3130/aijs.67.185_1

Orkhon hydrogeology Co. Ltd. (2014). *Engineering geological map of Ulaanbaatar*. Ministry of Construction of Mongolia.

Oyun-Erdene, Odonbaatar, C., & D, G. (2014). Predicting strong ground motion of Emeelt fault. *Science Academy News*, *2*(210), 48–56. https://doi.org/10.5564/pmas.v54i2.654 (in Mongolian)

Piña-Flores, J., Perton, M., García-Jerez, A., Carmona, E., Luzón, F., Molina-Villegas, J. C., & Sánchez-Sesma, F. J. (2017). The inversion of spectral ratio H/V in a layered system using the diffuse field assumption (DFA). *Geophysical Journal International*, *208*(1), 577–588. https://doi.org/10.1093/gji/ggw416

Porter, K. (2015). Beginner's Guide to Fragility, Vulnerability, and Risk. In M. Beer, I. A.

Kougioumtzoglou, E. Patelli, & S.-K. Au (Eds.), *Encyclopedia of Earthquake Engineering* (pp. 235–260). Springer Berlin Heidelberg. https://doi.org/10.1007/978-3-642-35344-4_256

Sánchez-Sesma, F. J. (2017). Modeling and inversion of the microtremor H/V spectral ratio: Physical basis behind the diffuse field approach. *Earth, Planets and Space*, *69*(1), 92. https://doi.org/10.1186/s40623-017-0667-6

Sanchez-Sesma, F. J., Weaver, R. L., Kawase, H., Matsushima, S., Luzon, F., & Campillo, M. (2011). Energy Partitions among Elastic Waves for Dynamic Surface Loads in a Semi-Infinite Solid. *Bulletin of the Seismological Society of America*, *101*(4), 1704–1709. https://doi.org/10.1785/0120100196

Schnabel, P. B., Lysmer, J., & Seed, B. (1972). *A computer program for earthquake response analysis of horizontally layered sites*.

The Ulaanbaatar Statistic, "Capital city property", & http://ubstat.mn/StatTable=381, (assessed on Sep. 1, 2021). (n.d.). Retrieved September 1, 2021, from http://ubstat.mn/StatTable=381

The World Bank, GDP (current US$)—Mongolia. (n.d.). https://data.worldbank.org/indicator/NY.GDP.MKTP.CD?locations=MN, (assessed on Sep. 1, 2021)). Retrieved September 1, 2021, from https://data.worldbank.org/indicator/NY.GDP.MKTP.CD?locations=MN

Tsamba, T., Masato, M., Susumu, O., Dashjamts, D., Ninjgarav, E., & Battulga, B. (2017). Real-Time Strong Motion Network With Structural Health Monitoring Function In Ulaanbaatar,

Mongolia. *16th World Conference on Earthquake Engineering, 16WCEE 2017*.

Tumurbaatar, Z., Miura, H., & Tsamba, T. (2019). Site Effect Assessment in Ulaanbaatar, Mongolia through Inversion Analysis of Microtremor H/V Spectral Ratios. *Geosciences*, *9*(5), 228. https://doi.org/10.3390/geosciences9050228

Ulaanbaatar 2020 master plan and development approaches for 2030. (2014). https://policy.asiapacificenergy.org/sites/default/files/Ulaanbataar%202020%20Master%20Plan%20and%20Development%20Approaches%20for%202030%20%28EN%29.pdf

UN Habitat. (2016). *Atlas of Urban Expansion: The 2016 Edition, Volume 1: Areas and Densities* [Map]. ISBN 978-0-9981758-0-5. https://www.lincolninst.edu/sites/default/files/pubfiles/atlas-of-urban-expansion-2016-volume-1-full.pdf

V. I., D., Kluchevskii, A. I., Serebnikov, S. P., Demiyanovich, B. M., Batsaikhan, T., & Bayaraa, G. (2009). Seismicity and seismic hazard zoning of Mongolian region. *Earth's Crust Institute*.

Yamin, L. E., Hurtado, A. I., Barbat, A. H., & Cardona, O. D. (2014). Seismic and wind vulnerability assessment for the GAR-13 global risk assessment. *International Journal of Disaster Risk Reduction*, *10*, 452–460. https://doi.org/10.1016/j.ijdrr.2014.05.007

Yamin, L. E., Hurtado, A., Rincon, R., Dorado, J. F., & Reyes, J. C. (2017). Probabilistic seismic vulnerability assessment of buildings in terms of economic losses. *Engineering Structures*, *138*, 308–323. https://doi.org/10.1016/j.engstruct.2017.02.013

Yepes-Estrada, C., Silva, V., Valcárcel, J., Acevedo, A. B., Tarque, N., Hube, M. A., Coronel, G., & María, H. S. (2017). Modeling the Residential Building Inventory in South America for Seismic Risk Assessment. *Earthquake Spectra*, *33*(1), 299–322. https://doi.org/10.1193/101915eqs155dp

Yoshida, N. (2015). *Seismic Ground Response Analysis* (Vol. 36). Springer. https://doi.org/10.1007/978-94-017-9460-2

Yoshida, N., Kobayashi, S., Suetomi, I., & Miura, K. (2002). Equivalent linear method considering frequency dependent characteristics of stiffness and damping. *Soil Dynamics and Earthquake Engineering*, *22*(3), 205–222. https://doi.org/10.1016/S0267-7261(02)00011-8

独立行政法人 & Japan International Cooperation Agency (JICA). (2016). *Mongolia Information gathering / confirmation survey related to disaster prevention field* (Final Report). Oriental Consultants Global Co., Ltd. Urban Disaster Prevention Research Institute Mongolia. https://openjicareport.jica.go.jp/pdf/12266573.pdf

List of publications

Peer-reviewed journal papers

Tumurbaatar, Z., Miura, H., and Tsamba, T. (2021). Development of Building Inventory Data in Ulaanbaatar, Mongolia for Seismic Loss Estimation. *ISPRS Int. J. Geo-Inf.* 2022, 11(1), 26. https://doi.org/10.3390/ijgi11010026. **2021.12**

Tumurbaatar, Z., Miura, H., and Tsamba, T. (2019). Site Effect Assessment in Ulaanbaatar, Mongolia through Inversion Analysis of Microtremor H/V Spectral Ratios. *Geosciences*, 9(5), 228. https://doi.org/10.3390/geosciences9050228. **2019.5**

Conference papers

Tumurbaatar, Z., Miura, H., "Earthquake Loss Estimation for Buildings in Ulaanbaatar, Mongolia, Based on Construction Cost Inventory Data" 17th World Conference of Earthquake Engineering, Sendai, Japan. **2021.9**

Tumurbaatar, Z., Miura, H., "Estimation of Shear-Wave Velocity Structure Using Microtremor Measurements", ISEC-10, Illinois Institute of Technology, Chicago, USA. Doi: 10.14455/ISEC.res.2019.71, **2019.5**

Tumurbaatar, Z., Miura, H., and Tsamba, T. "Inversion of Microtremor H/V Spectral Ratios for Estimating Shear-Wave Velocity Structures in Ulaanbaatar" *Proceedings MJEED conference*, 1st Integrated Conference on Joint Research Program in Mongolia (ICJPM) of MJEED project. **2019.3**

Tumurbaatar, Z., Miura, H., "Strong Ground Motion Simulation and Seismic Response Analysis for Ulaanbaatar City", 12th Annual meeting of "*Geotechnical issues on Buildings and Structures*, Ulaanbaatar, Mongolia. **2018.3**